CONTROLLED ROCKING HEAVY TIMBER WALLS

DESIGN OF CONTROLLED ROCKING HEAVY TIMBER WALLS FOR LOW-TO-MODERATE SEISMIC HAZARD REGIONS

By MICHAEL A. KOVACS, B.ENG.

A Thesis Submitted to the School of Graduate Studies in Partial Fulfilment of the Requirements for the Degree Master of Applied Sciences

McMaster University MASTER OF APPLIED SCIENCES (2016) Hamilton, Ontario (Civil Engineering)

TITLE: Design of Controlled Rocking Heavy Timber Walls for Low-to-Moderate Seismic Hazard Regions

AUTHOR: Michael A. Kovacs, B.Eng. (McMaster University)

SUPERVISOR: Professor Lydell Andree Wiebe

NUMBER OF PAGES: xv, 148

Lay Abstract

The controlled rocking heavy timber wall (CRHTW) is a high-performance structural solution that was developed to resist high seismic loads without sustaining structural damage. The wall responds in bending and shear to small lateral loads, and it rocks on its foundation in response to large seismic loads. In previous studies, rocking has been controlled by both energy dissipation elements and post-tensioning; the latter returns the wall to its original position after a seismic event. This controlled rocking behaviour mitigates structural damage and costly repairs.

This thesis explores the value of an adapted CRHTW in which the design and construction costs and complexity are reduced for low-to-moderate seismic hazard regions by using post-tensioning but no supplemental energy dissipation. A design and analysis process is outlined; numerical analysis confirms the expected performance of the adapted CRHTW; and the system is shown to have a low probability of collapse.

Abstract

The controlled rocking heavy timber wall (CRHTW) is a high-performance structural solution that was first developed in New Zealand, mainly considering Laminated Veneer Lumber (LVL), to resist high seismic loads without sustaining structural damage. The wall responds in bending and shear to small lateral loads, and it rocks on its foundation in response to large seismic loads. In previous studies, rocking has been controlled by both energy dissipation elements and post-tensioning, and the latter returns the wall to its original position after a seismic event. The controlled rocking response avoids the need for structural repair after an earthquake, allowing for more rapid return to occupancy than in conventional structures.

Whereas controlled rocking walls with supplemental energy dissipation have been studied before using LVL, this thesis proposes an adapted CRHTW in which the design and construction cost and complexity are reduced for low-to-moderate seismic hazard regions by removing supplemental energy dissipation and using cross-laminated timber (CLT) because of its positive economic and environmental potential in the North American market. Moreover, whereas previous research has focussed on direct displacement-based design procedures for CRHTWs, with limited consideration of force-based design parameters, this thesis focusses on force-based design procedures that are more common in practice. A design and analysis process is outlined for the adapted CRHTW, based on a similar methodology for controlled rocking steel braced frames. The design process includes a new proposal to minimize the design forces while still controlling peak drifts, and it also includes a new proposal for predicting the influence of the higher modes by referring to previous research on the capacity design of controlled rocking steel braced frames. Also, a numerical model is outlined, including both a baseline version and a lower-bound model based on comparison to experimental data. The numerical model is used for non-linear time-history analysis of a prototype design, confirming the expected performance of the adapted CRHTW, and the model is also used for incremental dynamic analyses of three-, six-, and nine-storey prototypes, which show a low probability of collapse.

Acknowledgements

The completion of this thesis owes a great deal to many in the Department of Civil Engineering. I sincerely appreciate the guidance and learning experience provided by my supervisor, Dr. Lydell Wiebe, whose strong understanding of the technical topics of this thesis was invaluable to the final product. Dr. Wiebe's genuine interest in building and maintaining an academic and social network among his students was essential to my positive graduate experience. I would also like to thank my peers, and many other staff and Faculty who have contributed to an extraordinarily positive graduate student community, socially and academically. A special, thanks to Taylor Steele for his patience and interest in teaching was essential to my understanding of controlled rocking and numerical modeling. Also, thanks to Adrian Crowder for being an amazing co-director on the extra-curricular seismic design team for two years; and to Niel Van Engelen for being such a strong role model since my first year as an undergrad. Paul Steneker, Dan Stevens, and Changxuan Zhang have had equally positive impacts on my graduate experience, and I am happy to call this a group of great friends as much a group of colleagues.

I also owe this thesis to the patience and support of my parents, and also to my wonderful partner Alex, for her patience, encouragement, and even enthusiasm throughout my studies.

Finally, I would like to acknowledge the financial support of the Department of Civil Engineering, an Ontario Graduate Scholarship, and the NSERC Discovery Grant, which have afforded me many opportunities for personal development and networking, in addition to the opportunity to complete this research project.

Table of Contents

Table of Figures

List of Tables

List of Abbreviations and Symbols

c	Neutral axis depth
CBA	Cantilever Beam Analogy
C_{CLT}	Compression force in CLT
CLT	Cross Laminated Timber
C_pC_g	Wind pressure-gust coefficients
C_R	Non-linear displacement estimation factor
c_{yield}	Location of first yield in CLT rocking toe, from neutral axis
d_{PT1}	Distance from rocking toe to furthest PT element
d_{PT2}	Distance from rocking toe to nearest PT element
E_{CLT}	Composite modulus of elasticity, considering longitudinal and transverse layers of CLT
ESF	Equivalent static force (higher mode estimation procedure)
E_t	Timber modulus of elasticity
$f_{c,//}$	Parallel-to-grain strength of timber
F_i	Equivalent static force, storey i
F_{sw}	Wall self weight
GM	Ground motion
H_i	Inter-storey height
h_w	Total wall height
$h_{mid,i}$	Mid-height of storey i
IDA	Incremental Dynamic Analysis
I_E	Importance factor
IM	Intensity measure
I_z	Moment of inertia, about central axis perpendicular to rocking plane
k	System stiffness matrix
L_{eff}	Effective Winkler spring length
LRFD	Load Resistance Factor Design
LVL	Laminated Veneer Lumber
l_w	Wall length (in-plane of rocking, from left to right rocking toe)
m	System mass matrix
MBA	Monolithic Bean Analogy
M_{CLT}	Base connection moment contribution from CLT
M_{con}	Base connection moment response
M_{cap}	Bending moment capacity of CLT panel
MDOF	Multi Degree of Freedom
M_{PT}	Total base connection moment contribution from PT
$M_{PT,X}$	Horizontal base connection moment contribution from PT

$M_{PT,Y}$	Vertical base connection moment contribution from PT
MSA	Multiple Stripes Analysis
M_v	Modifying factors of higher mode effects
NBCC	National Building Code of Canada
NLTHA	Non-linear time history analyses
OTM	Overturning moment
PBEE	Performance-Based Earthquake Engineering
p_e	External wind pressure
PRESSS	Precast Seismic Structural Systems
PT	Post-tensioning
PT_{final}	Final post-tensioning force, at a given rocking drift
R_dR_o	Force reduction factor (Canadian Building Code)
r_{mode}	Modal response, due to *mode*
$S_a(T)$	Spectral acceleration
SDOF	Single Degree of Freedom
S_M	Scaling multiplier, for individual spectra to target spectra
$S_{M2,mean}$	Scaling multiplier, for mean spectra
SRSS	Square Root Sum of Squares
SSF	Spectral Shape Factor
$S_g(T)$	Individual ground motion spectrum, to be scaled
$S_T(T)$	Target design spectrum, for scaling
T_n	Natural period
$T_{PT,init}$	Initial PT force
t_{wall}	Thickness of wall
UFP	U-Shaped Flexural Plates
UHS	Uniform Hazard System
V_{base} (V_b)	Base shear
V_{cap}	Shear capacity of CLT panel
WSA	Winkler Spring Analogy
W_{trib}	Tributary seismic weight
y_{cent}	Centroid of base connection response, from neutral axis
β	Energy dissipation / Variance of fragility curve (Chapter 6)
$\Delta_{CLT,relax}$	Compression deformation in CLT relaxation due to initial PT force
ΔL_i	Total change in PT length due to rocking
$\Delta_{non\text{-}lin}$	Total deflection, including elastic and rocking contributions
Δx_{PT}	Horizontal change in PT length
Δy_{PT}	Vertical change in PT length
$\varepsilon_{CLT,max}$	Max. strain in CLT
θ	Median intensity parameter, fragility curve

θ_{con}	Base connection rotation (rigid body rocking rotation)
$\theta_{non\text{-}lin}$	Total roof drift, including elastic and rocking contributions
ξ	Damping coefficient
ρ	Density of CLT wall
Ω	Base connection moment over strength factor
ω_i	Natural frequency (radians/second)

1 Introduction

1.1 Motivation

Developing sustainable and resilient infrastructure has become an important objective for building owners, architects, and structural engineers (Bocchini et al., 2014). Structural engineers achieve sustainability and resilience through the choice of structural material, and how that material is applied to buildings and other infrastructure (Bocchini et al., 2014). Themes of sustainability and resilience are especially evident with respect to seismic design of buildings in dense urban population centers, where society is coming to realize the vulnerability of its social, political, and economic systems to natural hazards (Bosher, 2008). This realization has led to demands for more sustainable development policies and practices related to structural engineering projects (Bocchini et al., 2014). For structural engineers to address these sustainability and resilience demands, a critical evaluation of traditional structural engineering methods is required (Buchanan et al., 2011).

A critical evaluation of traditional structural engineering methods is supported by the motivations for Performance-Based Earthquake Engineering (PBEE) as a design principle (Krawinkler & Miranda, 2004). PBEE seeks to improve on the failure of traditional methods to quantify structural performance expectations under multiple hazards levels, to better address the needs of a structure's stakeholders (Krawinkler et al., 2004).

Recent earthquakes in New Zealand (2010-2011) have highlighted the need for this critical evaluation of structural engineering practices, and have motivated a shift towards PBEE principles: the Canterbury earthquake sequence structurally affected much of the Central Business District in Christchurch, New Zealand (Canterbury Earthquakes Royal Commission, 2012). Costs for demolition, rebuilding, and repair, in addition to economic down-time, have been estimated at twenty percent of New Zealand's annual GDP; all of these costs despite most buildings still standing after the earthquake events (Canterbury Earthquake Recovery Authority, 2012). Recent reflections on the rebuilding efforts and the public's post-disaster expectations

emphasize the need for a critical evaluation of structural engineering methods (Buchanan et al., 2011; Canterbury Earthquakes Royal Commission, 2012; Pampanin, 2015). Stakeholders in New Zealand want to make informed decisions regarding the costs and related performance of their structures under seismic loads, and engineers require a method to facilitate an informed decision on this matter (Krawinkler et al., 2004).

An evolving appreciation for global seismic risk and resilience has extrapolated the significance of the Canterbury earthquake sequence to a global scale (The World Bank, 2014). This was even suggested more than a decade ago, when Krawinkler and Miranda wrote that an evolving understanding of global seismicity, and a realization that earthquake damages could easily and significantly surpass expectations, would be the motivating factors for PBEE principles (Krawinkler et al., 2004). This evaluation of PBEE motivations is certainly reflected in modern earthquake engineering knowledge, as presented in the following section.

1.1.1 Earthquake Engineering in Regions of Low-to-Moderate Seismicity

Densely populated regions around the world face a range of seismic hazards, from the high risk areas around the Pacific Rim, to the low or moderate risk areas across most of North America and Europe (See Figure 1.1). However, while Christchurch is rebuilding after the Canterbury earthquake sequence of 2011 with resilient and sustainable infrastructure to withstand its next seismic event, recent studies have exposed significant structural engineering vulnerabilities in lower seismic risk regions (AIR Worldwide, 2013; Guéguen et al., 2007). These vulnerabilities include aging infrastructure and outdated performance objectives which only emphasize life safety, magnifying the social and economic risks in densely populated regions with a large quantity of susceptible buildings (AIR Worldwide, 2013; Guéguen et al., 2007; Kuang, 1998).

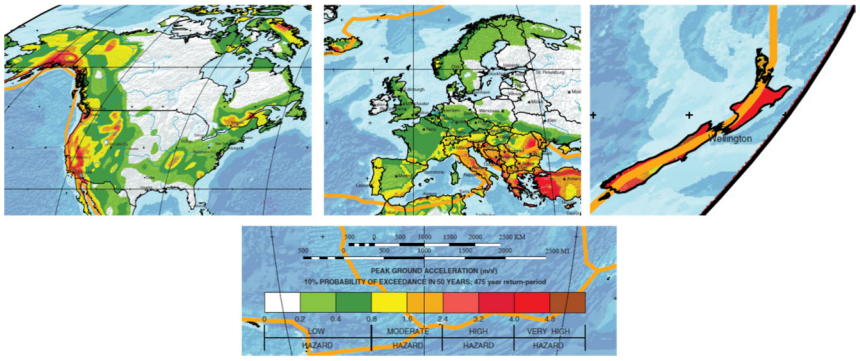

Figure 1.1: Seismic hazard maps of North America (left), Europe, and New Zealand (right) taken from Giardini, Grunthal, Shedlock, & Zhang (1999)

1.1.2 Controlled Rocking as a Resilient Structural Solution

In response to the need for resilient infrastructure, structural engineers can adopt a variety of structural solutions, including both isolation and other damage resistant design techniques (Pampanin, 2015). One damage resistant design technique is controlled rocking, which is available in structural frame and wall alternatives, shown in Figure 1.2 (Priestley et al., 1999) . The controlled rocking component of the building is constructed using a combination of traditional structural techniques, including pre-manufactured elements, post-tensioning, and a robust foundation. In a seismic event, ground motions induce deformations in post-tensioned connections designed to dissipate seismic energy and return to their original position after an event (self-centering). Controlled rocking has been applied to concrete, steel, and timber (e.g. Christopoulos et al., 2002; Palermo et al., 2005; Priestley et al., 1999). Each of these controlled rocking systems serves as an alternative to traditional concrete, steel, or timber construction systems which rely on yielding connections (i.e. damage) to dissipate seismic energy.

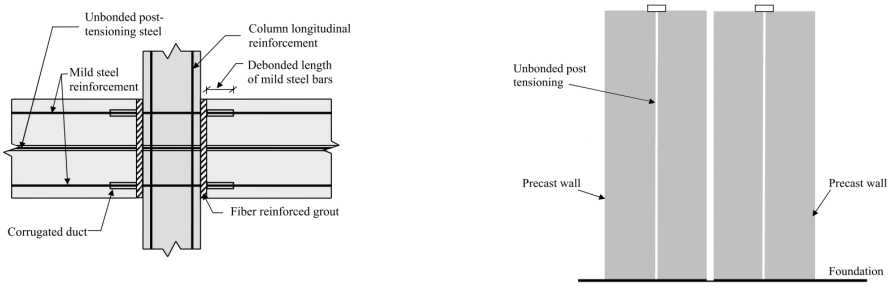

Figure 1.2: Controlled rocking frame and wall alternatives taken from Rahman (2008)

Controlled rocking structures have increased in popularity in New Zealand, which has embraced the technique for resilient structural design (Buchanan et al., 2011). The structures have only a small (or else non-existent) cost premium over traditional structural systems, and especially compared to base isolation which requires expensive foundation design and construction (Buchanan et al., 2011). It is difficult to define either controlled rocking or base isolation as an objectively superior solution. However, the apparent cost advantage of controlled rocking structures is beneficial in low-to-moderate seismic regions where a lack of perceived seismic risk can prevent more expensive resilient structural solutions (Buchanan et al., 2011).

1.1.3 Cross-Laminated Timber as a Sustainable Structural Material

The most recent heavy timber application to the controlled rocking concept is Cross-Laminated Timber (CLT) (Dunbar et al., 2013; Ganey, 2015). CLT is a modern engineered wood product, composed of layers of dimension lumber stacked and glued together in perpendicular layers. It is rather popular in Europe, and is gaining acceptance in North America as a large panel product (Moses & Gagnon, 2010). CLT is a challenger to an alternative heavy timber product, Laminated Veneer Lumber (LVL), which has been used for most previous studies on controlled rocking timber (Buchanan et al., 2011).

CLT's challenge to LVL has merit on several significant points of contention: CLT's manufacturing process is less energy intensive, and therefore less expensive (heat and pressure are required for LVL manufacturing, whereas CLT only requires pressure) (Structural Timber Association, 2014). CLT is also panelized, as opposed to LVL which is manufactured as a beam and column in North America (Structural Timber Association, 2014). As an engineered timber element, CLT can also employ a range of timber grades, internally: timber damaged by forest infestations, and lower quality timber can be removed from the waste cycle, and used within CLT panels (Moses et al., 2010).

The use of timber as a structural material in general presents an excellent opportunity to reduce carbon emissions and contain carbon dioxide for the lifecycle of the structure (Schmidt & Griffin, 2013). These environmental performance

features are in stark contrast to steel and concrete structural systems which require significant heat and pressure to manufacture, or release carbon dioxide over their lifespan (Schmidt et al., 2013).

1.2 Objectives & Scope

This research seeks to develop a better understanding of controlled rocking heavy timber walls for a low-to-moderate seismic context, in order to realize the system as a sustainable and resilient structural alternative. In order to develop this understanding, a controlled rocking wall must be designed with relevant timber products, and evaluated considering low-to-moderate seismic hazards. There is a special interest to explore a simplified controlled rocking wall design for low-to-moderate seismic hazards of Canada. To achieve this specific goal, post-tensioning requirements and energy dissipation elements will be critically evaluated, and the controlled rocking wall design and analysis processes will be investigated to find opportunities for simplification.

The performance of a controlled rocking wall will be demonstrated numerically, before physical testing is performed in future studies. This research will focus on understanding the design and development of the controlled rocking numerical model with CLT, subjected to Canada's low-to-moderate seismic hazard demands. The controlled rocking wall design, analysis, and numerical modeling will subsequently help to identify key issues that require experimental investigation. The design and modelling processes will allow for a critical evaluation of the controlled rocking heavy timber wall technology, so as to better understand how controlled rocking heavy timber walls could be developed for low-to-moderate seismic regions.

1.3 Thesis Organization

Chapter 2 presents a review of the concepts leading to controlled rocking heavy timber structures, with more detail on regions of low-to-moderate seismic hazard, controlled rocking as a resilient structural solution, and CLT as a sustainable structural material, as introduced in Section 1.1. First, the need for achieving sustainable and resilient structural design is explored through Performance Based

Earthquake Engineering (PBEE); there is a significant focus on the application of PBEE in low-to-moderate seismic regions. Next, controlled rocking is reviewed as a means for addressing low-to-moderate seismic hazard: CLT is examined as an efficient and sustainable heavy timber alternative for controlled rocking systems, and a technical overview is provided for controlled rocking heavy timber. Finally, a detailed review is provided for two areas of controlled rocking system research, including response control, and higher mode estimation. These areas of controlled rocking research are adapted in this thesis to the controlled rocking heavy timber wall.

A prototype structure is designed with controlled rocking CLT panels for the low-to-moderate seismic hazard of Ottawa, Ontario, Canada in Chapter 3. Chapter 3 also outlines an analysis process, providing the wall response to a pushover; the analysis process is related to the numerical modeling presented in the subsequent chapter. Finally, Chapter 3 outlines two methods for estimating the higher mode demands on the controlled rocking heavy timber wall, for the purpose of capacity design.

Chapter 4 presents the development of a controlled rocking CLT numerical model in OpenSees. The model is applied to an experimental program from Sarti (2015), and the system properties are calibrated to reflect a lower-bound of the experimental data. The baseline model and the lower-bound calibration are subsequently applied to the prototype design from Chapter 3, and the pushover performance is compared with the analysis and design expectations. Throughout Chapters 3 and 4, existing design, analysis, and numerical modeling methods are critically evaluated, given the unique application of CLT to controlled rocking walls in a low-to-moderate seismic context.

Chapter 5 presents ground motion selection and scaling for the structure in Ottawa. Non-linear time history analyses are subsequently conducted with the scaled ground motions on the prototype design from the previous chapters. The analyses allow for an investigation of the model's sensitivity and the system's performance. Key parameters include peak roof displacements, storey drifts and accelerations,

bending moment and shear demands over the wall height, and peak rocking toe stresses.

Chapter 6 expands on the analysis from Chapter 5 by presenting three different controlled rocking heavy timber designs for Montreal, Quebec, including a three-, six-, and nine-storey design. The designs are modelled and investigated by an incremental dynamic analysis process.

Chapter 7 presents the conclusions from the design, analysis, and numerical modeling of a controlled rocking CLT wall for low-to-moderate seismic hazards in Canada, as well as the incremental dynamic analysis procedure. The discussion is connected to the motivations and objectives outlined in Chapter 1. Furthermore, several important considerations are discussed for future research.

2 Literature Review

This section presents background and context for the subsequent research project, with references to previous literature. The motivating factors of sustainable and resilient structural design are first explored through the concept of Performance Based Earthquake Engineering (PBEE), which is then justified in low-to-moderate seismic hazard regions. Controlled rocking is then explored as a structural design alternative to achieve PBEE objectives, and Cross-Laminated Timber (CLT) is studied as an efficient and sustainable heavy timber alternative for controlled rocking structures. Finally, recent controlled rocking structural research is reviewed to understand the possibilities for simplifying the controlled rocking heavy timber wall in low-to-moderate seismic hazard regions.

2.1 Performance Based Earthquake Engineering for Sustainable and Resilient Infrastructure

To consider more holistic objectives for the design of modern structures, Performance Based Earthquake Engineering (PBEE) is offered as an alternative to Load and Resistance Factor Design (LRFD) as the established method of structural design in modern building codes (Krawinkler et al., 2004). With PBEE, degrees of structural performance must be achievable by a structural design solution, and each degree of performance associated with a risk of occurrence (Krawinkler et al., 2004). In comparison, LRFD does not explicitly consider degrees of performance; LRFD, as implemented in North American building codes, is primarily seeking to prevent collapse given a specified degree of hazard (Krawinkler et al., 2004). PBEE addresses varying function and maintenance objectives of individual structures, especially after a seismic event: some structures simply need to be evacuated safely, while others must maintain some level of functionality. These decisions are made in cooperation with all stakeholders of a project, while also considering the cost of each option.

The various degrees of post-disaster objectives in PBEE have motivated several areas of seismic engineering research, including low-damage design (Hare et al.,

2012). This concept is explored further in Section 2.3, where the controlled rocking PBEE design strategy is presented.

The importance of PBEE is illustrated by the aftermath of the 2011 earthquakes in New Zealand (Canterbury Earthquake Recovery Authority, 2012): the economic center of a major city in New Zealand was effectively rendered useless after an earthquake. Although life safety objectives were generally satisfied in the seismic event, the economic damage and recovery efforts exposed the difference between society's expectations of structural performance, and the existing design standard. In the future, stakeholders of the Christchurch Central Business District (CBD) expect to have more input regarding structural performance in a seismic event, hence the application of PBEE principles in the redevelopment plan for Christchurch (Pampanin, 2015).

Christchurch's desire for PBEE principles becomes increasingly relevant in an urbanizing world since population centers are densifying, with larger populations relying on the economic and social systems that exist within those urban centers (Department of Economic and Social Affairs: Population Division, 2014). This urbanization process gives the PBEE concept additional relevance, even in low-to-moderate seismic regions.

2.2 PBEE Principles in Low-to-Moderate Seismic Regions

Significant efforts have been made to adapt unique structural solutions to regions of high seismicity in order to achieve PBEE principles (Pampanin, 2015). However, high seismic hazard regions are not the only locations where buildings are built, nor are they necessarily the regions of highest seismic risk. Risk is proportional to hazard, exposure, and vulnerability, and the latter two terms can be significant where there is only a low-to-moderate degree of seismic hazard, with dense populations and/or important infrastructure for large social and economic systems (The World Bank, 2014). Earthquake engineering researchers have also noted this increased risk through vulnerability studies of low-to-moderate seismic regions around the world. For example, Kuang (1998) expressed concern for updating structural design

regulations to address the potential consequences of a seismic event, which could impact a significant population; and in France (Guéguen et al., 2007) and Spain (Lantada et al., 2009), several low-to-moderate seismic hazard regions were recognized as high risk, with the potential for significant losses to life and economy, even in a minor seismic event, due to a limited understanding regarding structural response to a seismic event.

In a Canadian context, low-to-moderate seismic hazard regions include Ontario and Quebec, which have known seismic hazards along the shared Ottawa and St. Lawrence River valleys. These hazards affect significant corridors between Toronto, Ottawa, and Montreal (Natural Resources Canada, 2013). An insurance and economic cost analysis of this region cites vulnerable building stock and increasing population densities as part of an estimated fifty billion dollar economic loss (in structural, non-structural, and economic down-time) in the event of a potential seismic event (AIR Worldwide, 2013). The rest of Europe, and most of the United States, have similar regions of low-to-moderate seismic hazard, adding to the global significance of this research (see Figure 1.1) (Klusell, 2008).

An appreciation of the risk in low-to-moderate seismic regions is growing among academia and industry. Unfortunately, appreciation is never higher than for a short period of time immediately after a major event (Fischer III et al., 1996). Therefore, to proactively address seismic risks in low-to-moderate seismic hazard regions, structural engineers can refer to high-performance PBEE solutions that address other stakeholder concerns as well: the increased control over a structure's performance is valuable to address seismic hazards, but also to quantify the cost of design options. Other stakeholder concerns that can be addressed with high-performance alternatives may include architectural options and environmental impact concerns, discussed in the following sections. By considering high-performance PBEE solutions that also address important social, environmental, and economic concerns, low-to-moderate seismic risk can be mitigated in regions where seismic hazard awareness is otherwise a barrier to the adoption of complex and expensive solutions.

2.3 Addressing Low-To-Moderate Seismic Hazard with Controlled Rocking Walls

A variety of solutions are available for structural engineers to achieve low-damage design as part of a PBEE design strategy. Base isolation and controlled rocking are two popular structural alternatives for achieving PBEE objectives (Pampanin, 2015). As outlined in Section 1.1.2, controlled rocking walls present an attractive opportunity to minimize costs and avoid complexity: controlled rocking is achieved with relatively standard construction detailing and pre-manufactured structural elements which reduce on-site labour and construction time (Smith & Buchanan, 2008). Furthermore, the pre-manufactured nature of controlled rocking walls offers an general advantage, even over traditional on-site construction practices: constructing structural elements in a controlled environment, for rapid delivery and placement on-site, is a significant cost- and waste-reduction technique (Robertson, 2011). The significance of these features is reinforced by Fischer III et. al. (1996) and Guéguen et al. (2007), whose low-to-moderate seismic vulnerability studies have cited construction and design cost and complexity as considerable barriers to implementing higher-performance solutions in regions where a low perception of seismic risk creates resistance to modifying traditional structural engineering practices.

Controlled rocking walls are explored further in the following subsections, to provide a background on the system and various developments that have shaped this thesis. First, barriers to the implementation of a heavy timber solution are addressed. Next, a basic background is provided on the controlled rocking system, including system mechanics, followed by more in-depth background, reviewing recent developments in the system design and analysis process. Finally, Cross-Laminated Timber (CLT) is considered in the context of controlled rocking heavy timber walls: CLT is identified as a particularly relevant timber product in the low-to-moderate seismic regions of North America, and compared with Laminated Veneer Lumber (LVL), the heavy timber product that has dominated existing research. Since cost and complexity are of concern, additional social, environmental, and economic factors

are identified that may promote the adoption of controlled rocking walls in low-to-moderate seismic hazard regions.

2.3.1 General Barriers to Implementation with Heavy Timber

Controlled rocking walls have been adapted to both concrete and timber formats (Palermo et al., 2005; Priestley et al., 1999). However, the heavy timber format is a sustainable alternative where timber is abundantly available and responsibly harvested, considering extensive life-cycle assessment research (Zabalza Bribián et al., 2011). Barriers to the uptake of the timber alternative have been widely explored, and include the perceived fire risk and building height limitations (Schmidt et al., 2013). These barriers are being addressed, however, as fire research demonstrates that heavy timber is slow to burn and can safely achieve fire resistance standards, and national building codes (like Canada's) subsequently relax their height restrictions on timber structures (Natural Resources Canada, 2015; Osborne & Dagenais, 2015). Furthermore, the heavy timber alternative offers additional structural design advantages on sites with poor soil conditions, since timber is much lighter than steel or concrete alternatives, requiring less costly geotechnical intervention (reThink Wood, 2014).

2.3.2 Background & Development

Controlled rocking heavy timber walls are based on concrete Precast Seismic Structural Systems (PRESSS) developed in California in the 1990's (Priestley et al., 1999). PRESSS consists of both controlled rocking frame (beam-column) and controlled rocking walls, as shown in Figure 1.2.

PRESSS was developed as a low-damage design alternative, considering PBEE objectives discussed in Section 2.1. Both rocking frame and wall systems rely on connection stiffness, provided by ductile connections at the base or between adjacent walls, to limit structural motion during minor seismic events.Furthermore, joints connected by post-tensioning cables help to control seismic motion in more significant seismic events (Newcombe, 2011). When activated by a significant seismic event, post-tensioned joints limit the forces transferred through a structure, and help

the structure return to its original position after a seismic event; ductile yielding connections (referred to as supplemental energy dissipation) dissipate seismic energy.

PRESSS in precast-concrete led to a proposal for comparable systems using pre-stressed, laminated timber products (for example, LVL and CLT), licensed under the brand name "Pres-Lam" (Palermo et al., 2005). In Pres-Lam, beam-column and wall alternatives offer unique architectural options and low-damage seismic performance by means of heavy timber products. In this research, the wall concept without supplemental energy dissipation is the primary focus for development.

Mechanically, the simplest controlled rocking wall system generally behaves as shown in Figure 2.1 (Sarti, 2015). Before uplift, the system flexibility is a combination of the base connection flexibility and the wall bending and shear deformations (Figure 2.1 (b)). Upon uplift, the post-tensioning elements, as part of the base connection response, act to return the wall to its original static position with a returning moment at the base connection, increasing as the wall is pushed laterally (Figure 2.1 (c,d)).

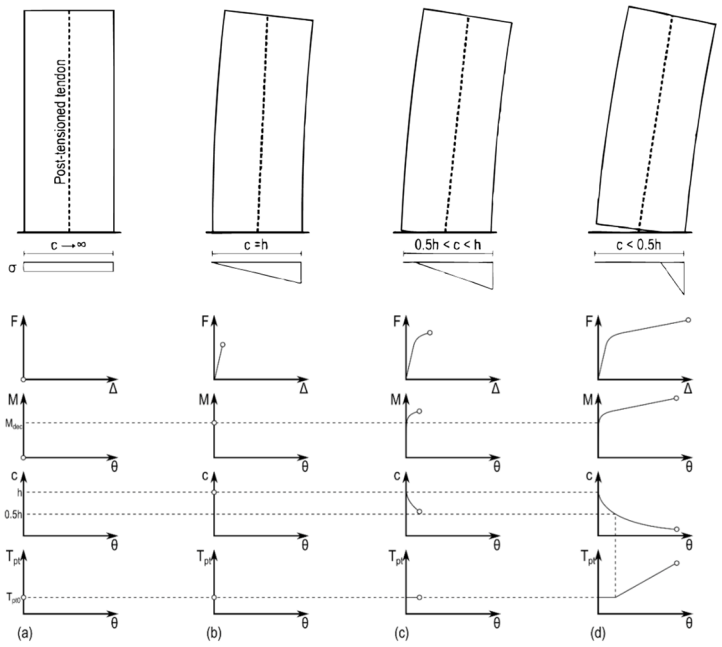

Figure 2.1: Controlled rocking wall, mechanical response taken from Sarti (2015)

The simple controlled rocking wall hysteresis is reflected in the "self-centering" unbonded post-tensioning hysteresis of Figure 2.2 (a), alongside the hysteretic component provided by supplemental energy dissipation in (b). The resulting controlled rocking system hysteresis is also shown, with a β-term indicating a measure of energy dissipation in the system response. Without supplemental energy dissipation, only internal friction of the wood fibers and impact between the rocking wall and foundation can dissipate energy from the rocking system. However, these components are negligible (β is small) for consideration in high seismic hazard design cases (Smith, 2014), which is why supplemental energy dissipation elements are specified to absorb energy in the rocking motion (Buchanan et al., 2008). These elements absorb seismic energy in the structural system to minimize the displacement response; however, post-tensioning forces must be increased to prevent residual structural displacements due to the supplemental energy dissipation elements (Buchanan et al., 2008).

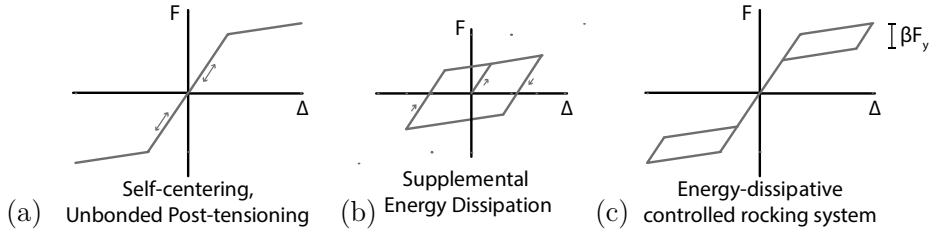

Figure 2.2: (a) Self-centering due to post-tensioning, and (b) contribution of supplemental energy dissipation to the controlled rocking system response shown in (c)

Several supplemental energy dissipation elements were developed for the PRESSS concrete wall system; these elements were adapted and studied on the controlled rocking timber wall. Two examples are U-shaped Flexural Plates (UFP's), and yielding steel elements installed at the wall base. UFP's offer additional overturning moment resistance and dissipate significant amounts of energy through yielding steel elements between coupled walls (Iqbal, Pampanin, et al., 2015; Newcombe et al., 2011). Yielding steel elements at the base also dissipate energy and resist overturning; they include bonded or partially bonded steel bars embedded within the rocking wall, or replaceable "Plug & Play" steel components connected externally (Newcombe et al., 2008; Smith et al., 2007). Another energy dissipating

technique was explored specifically for controlled rocking timber walls, relying on traditional timber fasteners to couple rocking walls (Dunbar et al., 2014; Iqbal, Smith, et al., 2015). The elements identified here are summarized in Table 2.1 and presented in Figure 2.3.

Table 2.1: Supplemental energy dissipation elements for controlled rocking heavy timber walls

Additional Design Element	Benefits	Drawbacks
U-Shaped Flexural Plate (Iqbal, Pampanin, et al., 2015)	Elements contained between walls; Additional overturning moment (OTM) resistance	Some inactivity at low-drift (minor timber damage)
Yielding Steel Bars (embedded internally) (Sarti et al., 2012a)	Elements contained internally	Internal bond slip reduces element effectiveness, and is hard to repair
Yielding Steel Bars (attached externally)	Easy and cheap to replace	Connection stiffness can degrade, reducing element effectiveness; Expands wall footprint
Coupling Plywood Sheets (Iqbal, Smith, et al., 2015)	Easy and cheap to replace with off-the-shelf materials	Less effective than yielding steel bars; Architecturally unappealing

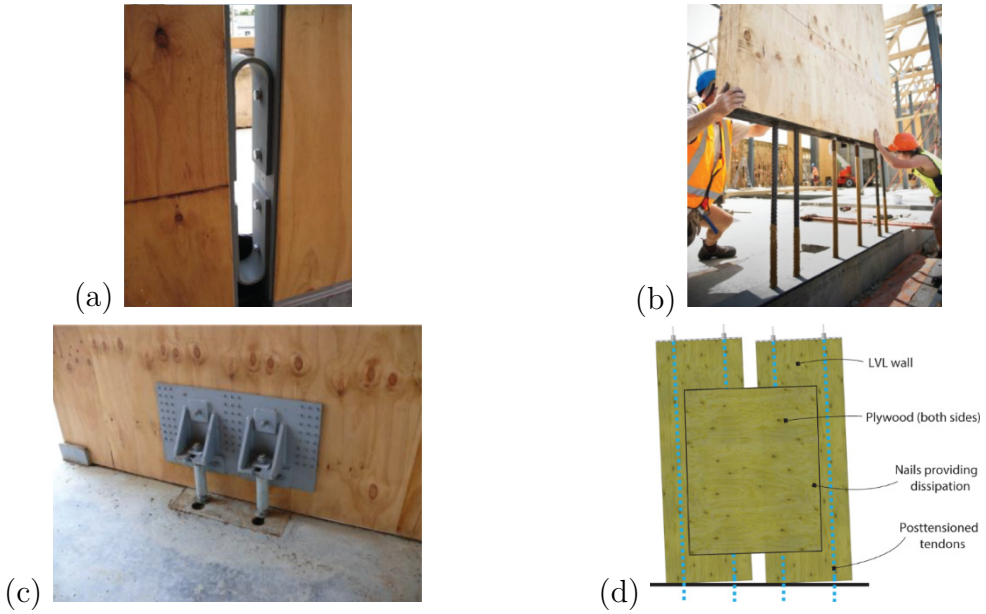

Figure 2.3: (a) UFP yielding elements; (b) Internal and, (c) external yielding elements; (d) Plywood coupled walls (Iqbal, Smith, et al., 2015; Sarti, 2015)

Research results for energy dissipating elements in the controlled rocking timber wall demonstrate their potential to reduce seismic effects, but also to damage the timber wall, either directly or indirectly, due to the increased post-tensioning demands required to ensure self-centering (Dunbar et al., 2014; Palermo et al., 2005). The extent of this damage is a function of the engineered timber product: weaker timber products will experience more extensive damage at the base (Newcombe, 2015). Furthermore, cyclically loaded energy dissipation connections become loose as the fasteners open a gap in the timber, reducing the element's effectiveness at low drifts (Iqbal, Pampanin, et al., 2015). These elements also add complexity to the design process, imposing additional unique forces: Figure 2.4 presents a comparison of the simple and energy-dissipative versions of the controlled rocking wall formats, demonstrating the complexity of two energy-dissipative controlled rocking walls. Note that each element has a different degree of effectiveness depending on the level of drift, further complicating design.

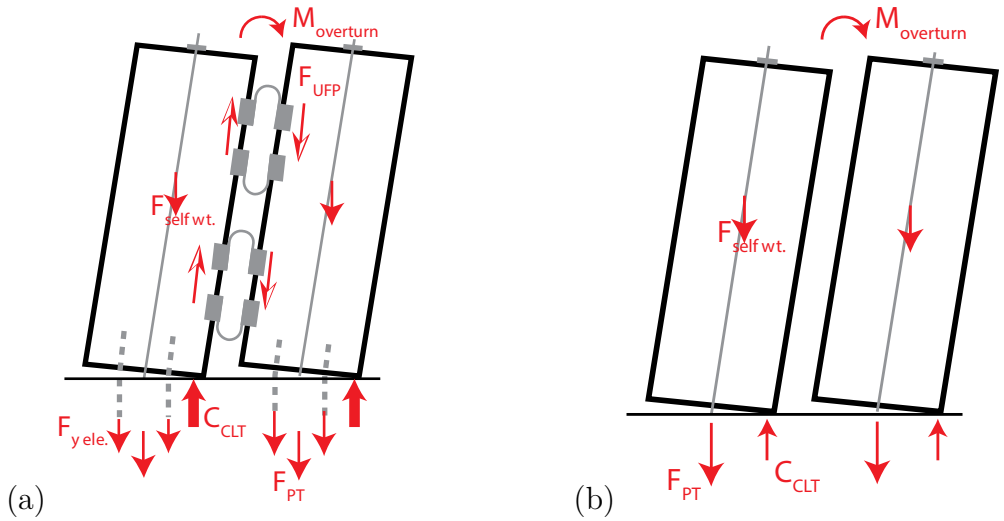

Figure 2.4: Controlled rocking wall comparison: (a) Additional forces and complexity imposed by energy dissipating elements; (b) Simplified controlled rocking wall

2.3.3 Recent Controlled Rocking Heavy Timber Wall Developments

The controlled rocking heavy timber wall has evolved significantly since Palermo et al. (2005) first proposed the controlled rocking heavy timber concept. In addition to numerous studies of energy dissipating elements (identified above), Sarti et al. (2015b) investigated several design details to make the controlled rocking system

compatible with the gravity system; Newcombe (2007, 2011) presented two numerical modeling techniques; Morris et al. (2012) and Yeoh et al. (2012) investigated post-tensioning behaviour in controlled rocking heavy timber, considering immediate and long term effects; and Sarti (2015) evaluated peak force and displacement responses of the controlled rocking heavy timber wall to understand the system response to seismic hazards. These developments coincide with commercial applications of controlled rocking heavy timber that have acted as case studies for the system (Pampanin, 2015). Some developments have helped the controlled rocking heavy timber wall to become more practically achievable; others have explored variations of the system and built a better understanding of its behaviour. These developments are expanded upon, below.

Displacement Compatibility between Rocking Wall Uplift and the Gravity System

One major practical challenge for controlled rocking structures is related to the rocking element's incompatibility with the rest of the structure: the incompatibility between the controlled rocking wall and the floor beams/diaphragms as the wall uplifts is depicted in Figure 2.5 (a). Moroder et al. (2014) studied three different pin connection designs that could reduce vertical and rotational constraints; Sarti et al. (2015b) subsequently studied a solution relying on parallel columns alongside the timber wall, shown in Figure 2.5 (b), which allow the use of coupling energy dissipating elements (UFP's). Therefore, the controlled rocking heavy timber wall's displacement incompatibility with the gravity system has been addressed with a number of design details which have already been used in several commercial applications (Moroder et al., 2014).

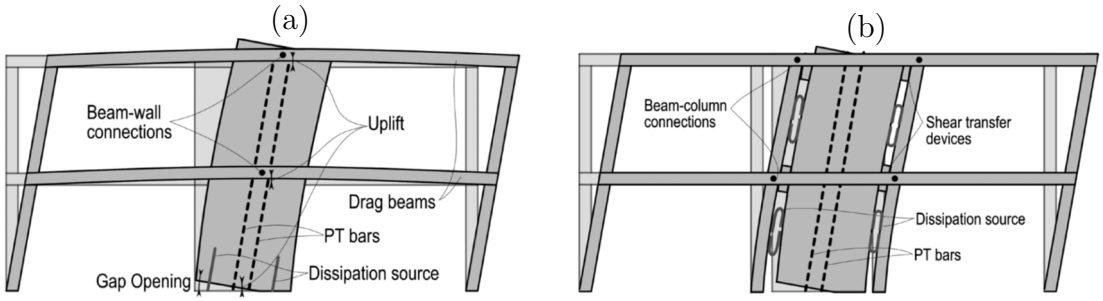

Figure 2.5: (a) Floor diaphragm uplift incompatibility with controlled rocking wall; (b) Controlled rocking with boundary columns, as a solution to uplift incompatibility, from Sarti et al. (2015b)

Numerical Modeling

Numerical modeling is an essential component to the investigation of controlled rocking wall behaviour. First, two general wall models are considered: a rotational spring model, and the multi-spring model (Figure 2.6). The former allows for an understanding of general system responses, including storey displacements and accelerations, interstorey drifts, etc.; but only the multi-spring model captures the system behaviour by modeling the base connection with a finite series of axial springs, with the elastic modulus of the timber and an area proportional to the base cross-section divided by the number of springs. With the multi-spring model, the system-uplift is captured in the response, and the forces in the base connection can be monitored throughout the response (Sarti, 2015).

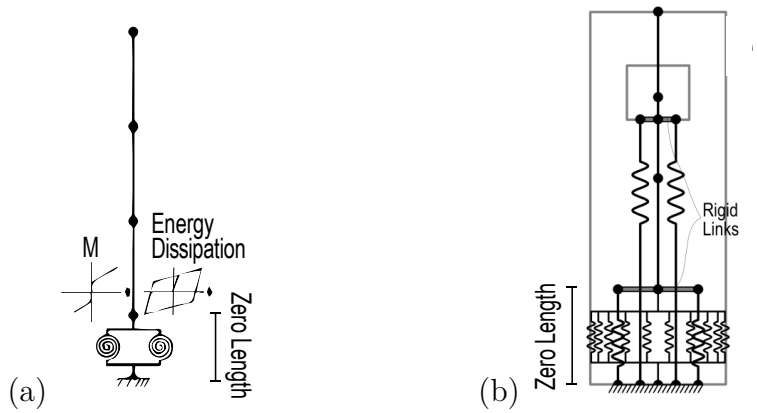

Figure 2.6: (a) Rotational spring and (b) multi-spring model; figures taken from (Sarti, 2015)

The multi-spring model has been in development since 2007, when the monolithic beam analogy (MBA) was applied to the controlled rocking heavy timber wall

(Newcombe, 2007). The MBA defines the multi-spring base stiffness (K_{eff}) as a function of the controlled rocking system's stiffness and mass distribution, i.e. the effective height of an equivalent single degree of freedom system, as shown in Figure 2.7 (a); it also requires additional calibration to experimental data (the λ_{exp}, calibration factor). The MBA is still applied in recent controlled rocking heavy timber wall studies; however, Newcombe (2011) presented the Winkler Spring Analogy (WSA) as an alternative. The WSA uses an empirical relationship that describes the effective length (L_{eff}) of a series of springs at the interface of the rocking wall base and the foundation. L_{eff} is determined by considering the stress fields at the controlled rocking wall base as the wall is pushed laterally, as shown in Figure 2.7 (b). An empirical relationship was developed from a study of finite element models and experimental testing, and originally considered a variety of different material properties and system parameters (Newcombe, 2011). Of the range of variables considered, only the neutral axis depth (c) in the base connection, as a fraction of the wall length (l_w), were found to be significant factors in the base connection stiffness (Newcombe, 2011). The empirical equation is given in Equation 2.1, describing L_{eff} as a function of c and l_w.

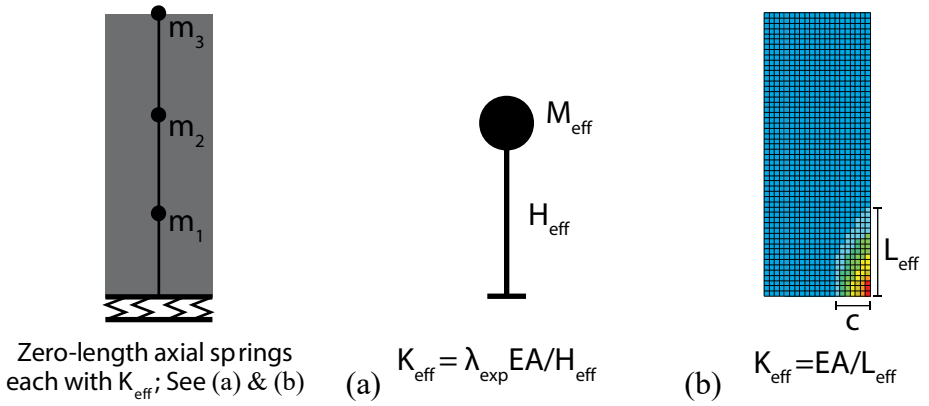

Figure 2.7: Base connection models for the controlled rocking heavy timber wall: effective Winkler spring stiffnesses as a function of (a) MBA, and (b) WSA

$$L_{eff.WinklerSpring} = 120\left(\frac{l_w}{c} - 1\right) \text{ (Newcombe, 2015)} \qquad \textbf{Equation 2.1}$$

The WSA produces a significantly larger estimate of stress in the base connection compared to the MBA: both techniques model the base with springs, but the MBA

uses much larger effective spring lengths, resulting in a reduced axial stiffness (Newcombe, 2015). Because of these differences in the definition of the base connection multi-spring model, the WSA can be especially important for heavy timber products that are softer/weaker than the Laminated Veneer Lumber (LVL) products, and also for tall controlled rocking walls, as Newcombe (2011, 2015) has suggested that the MBA method significantly underestimates the stress in these cases. Furthermore, the MBA also requires further calibration parameters to match the system response, as demonstrated by Sarti (2015); therefore, without experimental data for the given controlled rocking wall design, the MBA model cannot be verified.

Long-Term Behaviour of Post-Tensioned Heavy Timber Panels

Controlled rocking heavy timber post-tensioning behaviour has been studied to understand changes observed over time: changes in post-tensioning lengths, and the causes of those changes, have been monitored in laboratory experiments and in real building cases (Morris et al., 2012; Yeoh et al., 2012). These studies have identified long-term relaxation of the tendons due to high post-tensioning stresses applied to timber, and also due to environmental changes such as temperature and moisture content which cause timber to expand and contract. Notably, these studies have focused on LVL products, and the same conclusions cannot necessarily be applied to all engineered timber products. For example, CLT is cited as a more dimensionally stable material, so additional studies are needed since performance expectations may be different (Moses et al., 2010).

Additional mechanical studies related to post-tensioning behaviour are presented by Sarti (2015), with finite element analyses of the top-of-wall anchorage elements, and referencing the long-term post-tensioning studies identified above. Concentrated stresses are linked with both short-term local timber damage and long-term timber creep. Sarti (2015) suggests that the steel plates on which the post-tensioning elements are anchored must be thick enough to distribute the post-tensioning stresses in the timber, because stress is directly linked to long-term creep (Yeoh et al., 2012).

The plate must also be large enough to avoid short-term local damage of the timber panel (Sarti, 2015).

Codifying the Design Process: Controlled Rocking LVL in New Zealand

Recent studies of controlled rocking LVL systems have focused on understanding their general capabilities and behaviour, subjected to high seismic hazard demands. In particular, Newcombe (2011) and Sarti (2015) presented design and analysis procedures for the system. They found that the system's peak displacements matched their design and analysis results; and they observed higher-mode effects in the system response, which can increase the peak forces in the system and require consideration in design. These studies led to the development of a PBEE framework for the controlled rocking heavy timber wall system, shown in Figure 2.8, and motivated the codification of the design process in New Zealand (Sarti et al., 2015a). However, Sarti and Newcombe's research has focussed on dissipative controlled rocking LVL systems for high seismic hazard regions; although they have suggested that the same principles could apply to other heavy timber products like CLT, the same studies have yet to be performed.

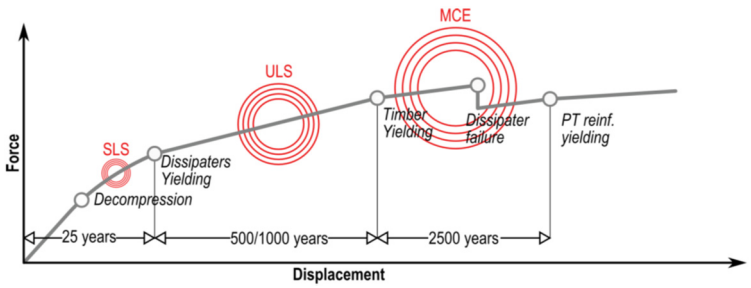

Figure 2.8: PBEE framework for the controlled rocking heavy timber wall, taken from (Sarti et al., 2015a)

2.3.4 Applying Cross-Laminated Timber to Controlled Rocking Heavy Timber Walls

The previous section identified significant developments of controlled rocking heavy timber walls made of LVL. However, some background on CLT is presented next, motivating the study of controlled rocking heavy timber walls made of CLT.

CLT Composition and Material Properties

CLT panels are produced in a relatively simple process: glue and pressure are applied to combine sawn timber in orthogonal layers, typically 15mm-35mm thick (see Figure 2.9). The manufacturing process is efficient, as timber waste is recycled into other timber products and used to fuel the manufacturing facilities (Structural Timber Association, 2014). CLT's orthogonal layers provide bi-directional strength, and help to maintain dimensional stability: alternating timber layers expand and contract at different rates, resisting change in adjacent layers (Moses et al., 2010). LVL is similarly efficient with regards to waste, but it is more expensive to produce because thin layers of wood (veneers) are shaved and glued together under high heat and pressure (Structural Timber Association, 2014).

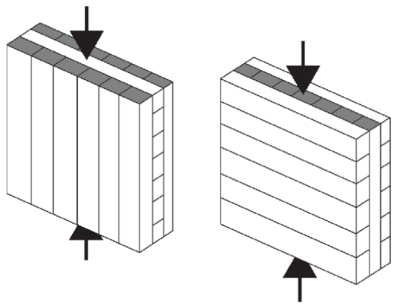

Figure 2.9: Alternating layers within CLT; strong layers (for the direction of loading) are highlighted

CLT is still a relatively new product, and as such, CLT design codes are in development and researchers investigating the in-plane CLT strength and stiffness properties (Andreolli et al., 2012; Gagnon et al., 2014). Currently, engineers can use standard beam mechanics and manufacturer-specified composite material properties to determine in-plane CLT properties for design (Gagnon & Pirvu, 2011). In this process, CLT material properties are taken as an average of the cross section ("effective" properties), and the gross cross section is used for geometric properties (cross-section, moment of inertia, etc.) as per the composite method outlined by Gagnon & Pirvu (2011). In the future, standardization of the CLT manufacturing process, stronger and stiffer timber grades, and an evolving understanding of the cross-layer interaction can improve CLT capacity specifications.

A sample of CLT properties compared with those of LVL is presented in Table 2.2. The effect of the material property differences is discussed further under the

heading *CLT versus LVL in Controlled Rocking Walls*, but some basic behavioural expectations are highlighted in the table. Furthermore, Ganey (2015) presented axial compression properties of CLT (important for the controlled rocking wall base), and simplified the resulting response as elastic perfectly plastic for the purpose of controlled rocking CLT modelling, as shown in Figure 2.10. Ganey's simplification of the actual CLT material hysteresis was justified by CLT compression studies performed by Horvat (2013).

Table 2.2: Comparing CLT to LVL, considering composite CLT properties over a gross cross-section

Property Parameter	Difference from LVL [1]	Value [2] (gross section)	Effect
Comp. Strength, f_c	60-70% Lower	13 MPa	Toe crushing more likely
Elastic Modulus, E	40-50% Lower	7,900 MPa	Increased higher mode demands; Increased elastic drift
Bending Strength, $f_{b,eff}$	50-60% Lower	19 MPa	Bending failure more likely
Shear Modulus, G	20-25% Lower	520 MPa	Increased higher mode demands; Increased elastic drift
Mechano-sorptive properties	Increased dimensional stability	N/A	Decreased PT force variability

[1] Comparing values from two sources (Flaig & Blass, 2013; Sarti, 2015)
[2] From KLH UK [2015], Newcombe [2011]; Sarti [2015] for 9-layer, 315 mm-thick cross section

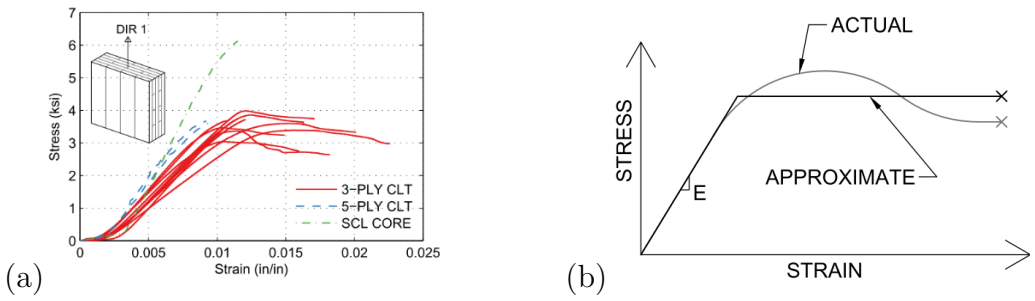

Figure 2.10: (a) CLT compression test results; (b) simplification of CLT material taken from Ganey (2015)

Traditional CLT Construction as A Motivator for Controlled Rocking CLT Development

CLT is currently used in North America and Europe as a wall element, in the same manner as traditional light-frame timber: lines of single-storey CLT panels support floor and roof panels, resisting inter-storey shear forces with ductile fastener connections at the base and between storeys (Moses et al., 2010; Polastri et al., 2015). In this format, CLT has an advantage as a premanufactured element: the panels are built off-site, and walls, doors, and conduits are precut from the panel, reducing expensive and inconsistent on-site work (Moses et al., 2010). Furthermore, CLT panels offer an economy of scale, since the same product is used for floors and walls. However, this shear wall system is architecturally restricting (see Figure 2.11

(a)), so an alternative construction method is desired to allow architectural and structural freedom from shear wall requirements (Dunbar et al., 2013; Sarti et al., 2012b). Furthermore, traditional light-frame and CLT shear walls are not resilient: failure modes include permanent damage via sliding, fastener yielding, and fastener tear-out (Ceccotti et al., 2006; Gavric et al., 2013; Pei et al., 2014).

Controlled rocking walls, shown in Figure 2.11 (b), have been proposed as an alternative to the traditional timber shear wall, as a resilient heavy timber solution for North America (Pei et al., 2014). Industry support is progressing with a Canadian group's recent purchase of the legal rights to Pres-Lam (controlled rocking heavy timber) technology in North America (Knee, 2015). This presents an opportunity for CLT to find a new application in the North American construction industry, and to benefit from the economy of scale offered by the existing CLT industries of North America and Europe.

(a)  (b) 

Figure 2.11: (a) Traditional shear wall format (Green, 2011); (b) controlled rocking timber wall (Nelson Pine, 2015)

CLT versus LVL in Controlled Rocking Walls

Both CLT and LVL have unique properties, as seen in Table 2.2, with different advantages to the controlled rocking wall. LVL is stronger and stiffer than CLT when considering the primary axis (direction of the grain; affects in-plane loading) (KLH UK, 2015; Nordic Structures, 2015). Conversely, CLT's alternating layers offer additional bi-directional strength and stability, as identified previously. This is significant because post-tensioning losses and fluctuations due to environmental conditions, as observed in existing commercial applications of controlled rocking LVL

(Morris et al., 2012), are concerning for engineers. CLT's bi-directional strength and stability could mitigate the loss and fluctuation in post-tensioning forces, reducing maintenance requirements.

LVL's superior strength and stiffness properties allow significant structural forces to develop at the base of the controlled rocking wall without sustaining damage, so it has been the preferred product in previous research and commercial applications (Palermo et al., 2005). In contrast, the few dynamic tests with controlled rocking CLT have demonstrated the susceptibility of the rocking toe to damage, through stages of extreme rocking (+/-9% drift), as shown in the test results from Ganey (2015) in Figure 2.12 (a). This fragility can cause the system's performance to degrade, as shown in the system hysteresis in Figure 2.12 (b). Below 2% roof drift, Ganey (2015) suggests that the performance degradation is due to low-to-moderate damage at the timber base; and beyond 2% drift, fragility is exacerbated by loosened the energy dissipating elements discussed previously, and can require connection repair or replacement of the energy dissipation elements, or rehabilitation of the rocking toe, which can split or plastically compress under the axial load.

(a)

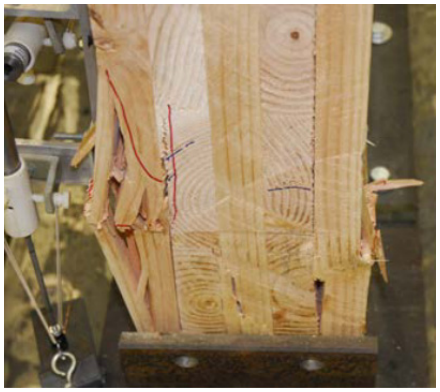

(b)

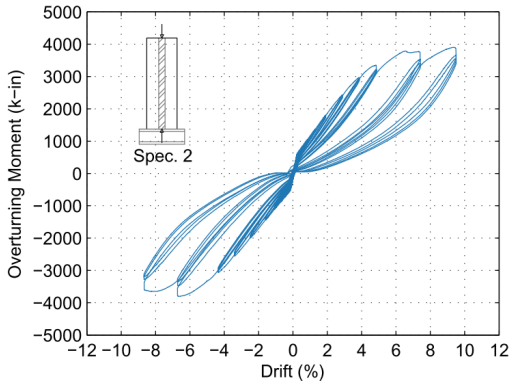

Figure 2.12: (a) Rocking toe damage at 9% drift, and (b) Hysteresis from CLT lab testing, taken from Ganey (2015)

Summary of Motivations for Applying CLT to Controlled Rocking Heavy Timber Walls

Applying CLT to the controlled rocking heavy timber wall presents a sustainable and resilient structural opportunity, in lieu of more expensive LVL products. This is especially true where CLT is already in demand or produced to some extent, as an

economy of scale can benefit stakeholders. These benefits, in addition to those of pre-manufacturing discussed in Section 2.3, address the goals cited in the opening of Section 2.3: the environmental and economic benefits of CLT can promote the adoption of controlled rocking structures in low-to-moderate seismic hazard regions. To develop this system, CLT properties must be applied to the models which were originally developed for LVL, to develop confidence that CLT performance can be predicted and that it is within acceptable ranges of performance.

In this thesis, additional developments and modifications are presented for the controlled rocking CLT wall. Reduced seismic demands in low-to-moderate seismic regions present an opportunity to minimize design complexity and avoid rocking toe damage in controlled rocking CLT walls by removing energy dissipating components and minimizing post-tensioning stresses. The following section explores research in the general field of controlled rocking structures in order to achieve the design objectives cited above, and to develop a better understanding of the controlled rocking wall performance.

2.4 Simplifying Controlled Rocking Wall Design

In the previous discussion, energy dissipation and post-tensioning elements were identified as creating long-term maintenance demands which can damage the base of the controlled rocking heavy timber wall and increase the complexity of design. Mitigating that damage and simplifying the design process can improve the practicality of the controlled rocking wall system in regions of low-to-moderate seismicity. To achieve this, it is proposed that supplemental energy dissipation and post-tensioning stresses be eliminated or minimized in the controlled rocking wall design, but this must be carefully balanced with the resulting controlled rocking wall response. This is discussed in Section 2.4.1.

Furthermore, it was noted in Section 2.3.3 that Newcombe (2011) and Sarti (2015) observed higher-mode effects in the controlled rocking wall response, and that these effects can increase the peak forces in the system, requiring consideration in design. To ensure it is relatively simple for designers to evaluate the controlled

rocking heavy timber wall performance, inclusive of higher-mode effects, three simplified methods are considered that were proposed for controlled rocking steel braced frames. This is discussed in Section 2.4.2.

2.4.1 Controlled Rocking Force Reduction Factors & Energy Dissipation

Zhang (2015) investigated the behaviour of self-centering systems like controlled rocking walls, to consider their response in a force-based design context. Codified force-based design procedures, like the Canadian building code, specify a reduction factor (R, in Figure 2.13 (a)) to reduce the design force for different structural systems (f_y, in Figure 2.13 (a)). Conventional structural systems specify R as a function of the system ductility (NRCC, 2010); however, Zhang (2015) found that controlled rocking walls do not behave according to the same principles. Zhang suggests that the equal energy and equal displacement assumptions that relate the available system ductility with R, are not effective with respect to estimating the self-centering system response. Therefore, Zhang performed a numerical study on self-centering single degree of freedom (SDOF) models, considering a variety of design and modeling parameters, to investigate seismic displacement demands. An empirical relationship was proposed to describe the maximum non-linear displacement of a self-centering system as a function of R, the degree of energy dissipation (β), and initial system period (T_1) (Zhang, 2015). Several of these system parameters are indicated in Figure 2.13, and the empirical relationship and its coefficients are shown in Equation 2.2 and Table 2.3, respectively. Zhang's empirical relation results in a ratio (C_R) of the non-linear to elastic displacement of a self-centring system, given R, β, and T_1.

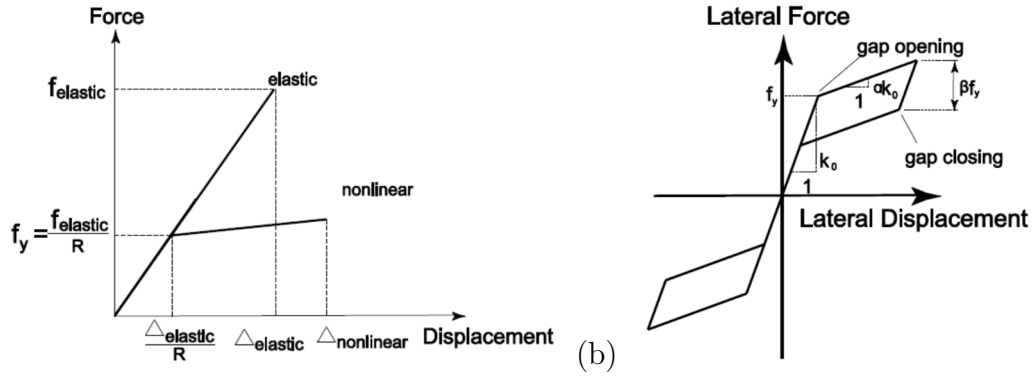

Figure 2.13: (a) Structural response according to force-based design, and (b) flag-shaped hysteresis (self-centering SDOF behaviour), taken from (Zhang, 2015)

$$C_R = \frac{\Delta_{nonlin}}{\Delta_{el}} = (R-1)^{b_1}\frac{b_2 + b_3(1-\beta)^{b_4}}{T_1^{b_5}} + 1 \qquad \text{Equation 2.2}$$

Table 2.3: Regression coefficients

Damping Model	Damping (ζ)	b_1	b_2	b_3	b_4	b_5
Initial Stiffness	5%	0.515	0.184	0.119	1.173	1.478
Initial Stiffness	2%	0.774	0.071	0.088	1.290	1.641
Tangential Stiffness	5%	0.630	0.292	0.477	1.697	1.567

Several key points were identified in Zhang's investigation of the SDOF modeling results. These points are related to the controlled rocking wall design in this thesis:

1. Energy dissipation (β) is not always imperative to limiting the peak drift response; in fact, energy dissipation has a reduced effect on self-centering system response when T_1 is greater than 0.5 seconds (Zhang, 2015).

2. The trends related to self-centering system response are generally the same for either initial or tangent stiffness damping models, although the displacement response with a tangent stiffness damping model is much larger. To be conservative in design, the tangent stiffness damping model should be considered (Zhang, 2015).

3. Ground motions used in Zhang's study are representative of California seismic hazard, and may not be applicable to other regions.

Zhang's research draws generally favourable conclusions for self-centering systems without energy dissipation, like the controlled rocking walls proposed in this thesis. It also supports the force-based design of self-centering systems by quantifying the non-linear response of the system.

2.4.2 Higher-Mode Effects in Controlled Rocking Heavy Timber Walls

A challenge for controlled rocking structural design is the evaluation and design for higher-mode effects (Lydell Wiebe & Christopoulos, 2015b). According to Newcombe (2011) and Sarti (2015), higher-mode effects can increase the bending moment and shear forces above the base of the controlled rocking heavy timber walls; however, Newcombe (2011) and Sarti (2015) both observed reserve bending moment and shear strength capacities of more than 50% in their investigations on controlled rocking LVL walls subjected to high seismic hazards. Nonetheless, forces due to higher-mode effects can govern the design process if they exceed the bending or shear capacity of the timber panel, and their influence is a function of the structural dynamic properties of the system: timber with lower shear and bending stiffness properties, and taller rocking walls, can be more susceptible to higher-mode effects. If the higher-mode effects exceed the heavy timber strength capacity, mitigation techniques have been proposed in controlled rocking steel systems, like multiple rocking sections over the height of the structure (Lydell Wiebe et al., 2015b), and could also be applied to controlled rocking walls (Ganey, 2015; Newcombe, 2011).

Evaluating the influence of higher mode effects is an ongoing challenge: for the controlled rocking heavy timber wall, Newcombe (2011) presented a linear and bi-linear approximation of storey shear forces and bending moments, respectively. However, Sarti (2015) found Newcombe's approximations to underestimate the controlled rocking wall response, and therefore calibrated the approximations according to a different set of controlled rocking numerical model results. The resulting approximations are empirically calibrated linear and bi-linear relationships to envelope the shear force and bending moment response, respectively, in the controlled rocking system (Sarti, 2015).

In this thesis, three alternative approaches to estimating the higher mode response are investigated, referring to research for controlled rocking steel braced frames. These approaches are the dynamic and equivalent static procedures outlined by Steele & Wiebe (2016), and the cantilever beam analogy outlined by Wiebe & Christopoulos (2015). The dynamic and equivalent static procedures estimate the higher mode response using response spectra and equivalent modal forces respectively; and the cantilever beam analogy provides an estimate of the higher mode contributions directly through closed-form equations. These procedures, presented and applied in Chapter 3, estimate the controlled rocking wall response over the height of the structure without empirical calibration, as opposed to enveloping the maximum peak response with empirical linear approximations. By investigating and verifying these procedures for the controlled rocking heavy timber wall, future research can efficiently and effectively investigate a wider range of controlled rocking heavy timber wall designs, including those which may be governed by higher-mode effects. This will help future research relating to multiple controlled rocking sections, as the higher-mode response is more effectively predicted. Furthermore, verification of these procedures will be important for the capacity design of the controlled rocking heavy timber wall, as the complex higher-mode response can be accounted for in commercial software engineering package, or by simplified procedures that are similar to those in current building codes. As per earlier discussion, these simplifications are especially beneficial for the adoption of controlled rocking CLT system in low-to-moderate seismic hazard regions.

3 Structural Design & Analysis

This chapter presents controlled rocking CLT wall design and analysis procedures for a six storey building in Ottawa ("the prototype"). The Canadian Building code (NBCC) and previous controlled rocking heavy timber wall design and analysis procedures are referenced for the design and analysis process; and other controlled rocking system research is used for investigating the higher mode demands on the controlled rocking heavy timber system. Additional comments and modifications to the analysis and design procedure are noted throughout, considering low-to-moderate seismic hazard and different material properties associated with CLT, rather than LVL.

In Section 3.1, the prototype building dimensions and storey weights are outlined. Then, the controlled rocking design and analysis procedures are presented in three phases. First, in Section 3.2, important design decisions are discussed and specified in the initial design phase, resulting in a controlled rocking wall configuration and an initial post-tensioning force to resist the seismic demand imposed on the prototype, especially considering the base connection of the controlled rocking wall. In the second phase (Section 3.3), the base connection mechanics are analyzed, and the system response in the rocking stage is calculated. An approximate pushover curve is constructed for the controlled rocking wall by analyzing the system response at several key points in the rocking stages of response. The final phase is the investigation of higher mode effects in Section 3.4. This phase refers to recent research in capacity design for controlled rocking steel braced frames: a capacity design procedure for the controlled rocking heavy timber wall is presented, and investigated further with the numerical modeling results presented in Chapter 5.

3.1 Prototype Definition

In Canada, the height of timber buildings allowed by the NBCC is increasing to six storeys (Lewington, 2014). The increasing height allowance presents an opportunity for developers of medium and high density regions; therefore, the prototype is defined as a six-storey structure with a footprint of approximately 3,000

square meters in accordance with Ontario building code for mixed use six-storey timber structures (Jeske & Esposito, 2015). Dimensionally, the prototype is 19.8 meters tall (3.3 meters per storey) and fifty-four meters square (2,916 square meters total footprint).

Floor weights for seismic design are based on the loads presented in Table 3.1. To evaluate the suitability of the loads assumed for determining seismic weight, a measure of weight per unit volume (weight density) of the structure is referenced and compared with other studies. The weight density of the prototype is 0.91 kN/m^3, which is larger than similar mid-rise controlled rocking timber building studies: Pei et al. (2012) suggested a weight density of 0.74 kN/m^3, Sarti et al. (2012) suggested 0.15 kN/m^3. However, a Canadian study using CLT shear walls suggested 1.18 kN/m^3 (Robertson, 2011). Therefore, the floor weights for the prototype design are within reason, considering a variety of other heavy timber structural studies; but the variability in seismic weights from these studies underscores the possibility for highly variable structural performance in a heavy timber structure, which uses relatively light structural members compared to steel and concrete structures. This is discussed as an opportunity for consideration in future seismic performance studies, with reference to FEMA P695 (Applied Technology Council, 2009) requirements, in Chapter 7.

Table 3.1: Storey weight contributions and total seismic storey weights

	Roof Pressures		***Floor Pressures***	
	Dead Load [1]	**Snow Load [2]**	**Dead Load [1]**	**Snow Load**
	2.3 kPa	2.4 kPa	3.0 kPa	-
Seismic Storey Weights:	**(Dead + 0.25 (Snow)) x (Tributary Area)**			
	6th Storey (Roof)		**1st – 5th Storey (per storey)**	
Total Building:	8490 kN		8810 kN	

[1] Based on values used in a CLT building Life Cycle Assessment (Robertson, 2011)
[2] Based on National Building Code of Canada snow loads for Ottawa (NRCC, 2010)

3.2 Initial Design Phase

Steps to determine seismic forces on a structure and design a controlled rocking wall are presented in Figure 3.1. This initial design phase results in a controlled

rocking wall configuration and initial post-tensioning (PT) force required to resist the seismic forces on the associated structure. These stages are presented in the subsections of Section 3.2.

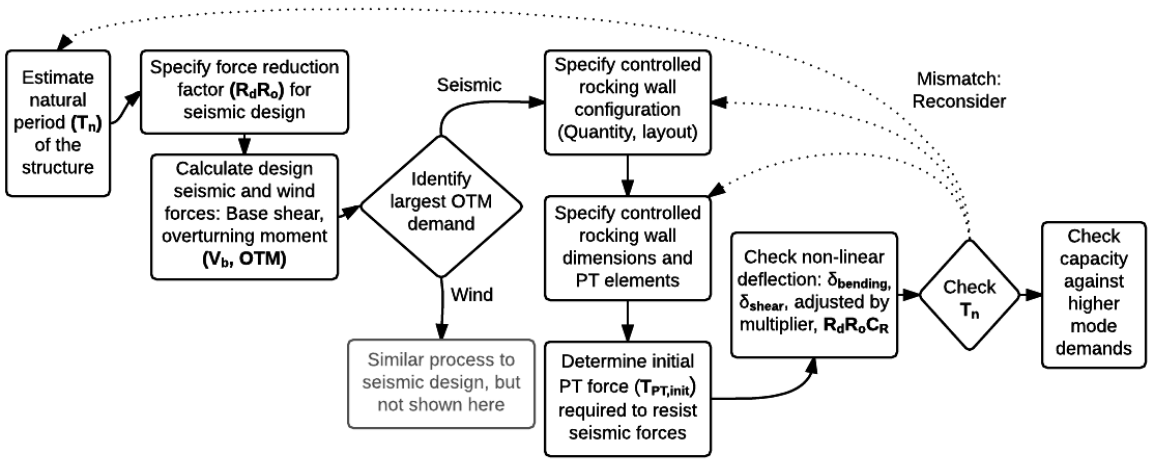

Figure 3.1: Process diagram for controlled rocking heavy timber wall design phase

3.2.1 Estimate The Natural Period (T_n) of the Structure

The force-based design procedure in the NBCC requires an estimate of T_n for the structure, to determine the seismic demand on the lateral force resisting system (NRCC, 2010). Force-based design codes like the NBCC use empirical formulas to estimate T_n, and these formulas rely on data from steel and concrete structures (Chopra & Goel, 1997; NRCC, 2010). Sarti (2015) investigated these empirical formulas in the context of controlled rocking heavy timber walls, and found them to significantly underestimate the wall's T_n. Therefore, a means of estimating T_n is required for the controlled rocking heavy timber wall, presenting an opportunity for future research. Nonetheless, a T_n of 1.80 s is assumed for the prototype presented here, based on modal analysis of the numerical model presented in Chapter 4, and the final step in the design process presents a means of checking this initial assumption.

3.2.2 Specify the Force Reduction Factor

In force-based seismic design, a reduction factor is applied in the structural design process to reduce the seismic force for designing specific elements. The reduced

force for design is related to the ductility available in the structural system, since the specific elements are expected to have a certain non-linear displacement capacity before failure. This concept is depicted graphically in Figure 3.2, reflecting the force-displacement response of a structural member designed for a reduced level of loading. Note, the Canadian force reduction factor, R_dR_o, is referred to in subsequent discussion.

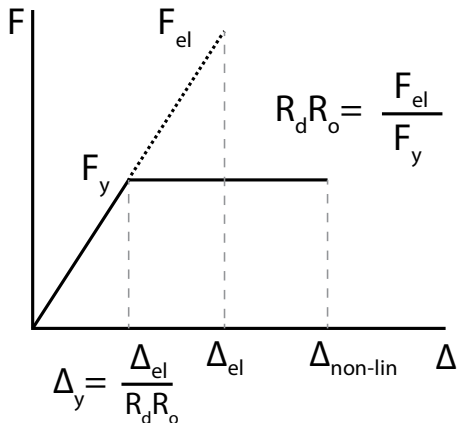

Figure 3.2: Force reduction factors (R_dR_o) in terms of controlled rocking wall response

The concept of designing to limit forces in specific members is fundamental to controlled rocking structures which concentrate structural deformations at specific ductile locations; in controlled rocking heavy timber walls, this is the base rocking joint. However, as discussed in Chapter 2 (Section 2.4.1), the peak displacement response ($\Delta_{non\text{-}lin}$) of a self-centering system is not effectively predicted by multiplying R_dR_o by the elastic displacement due to design forces. Instead, relatively large R_dR_o values can be selected for design of the controlled rocking heavy timber wall, but an additional non-linear displacement correction term is required at the end of the design process, to estimate the maximum $\Delta_{non\text{-}lin}$ demand; the additional term is referred to as C_R by Zhang (2015), and is shown in Figure 3.3. C_R is determined by a regression equation as part of the design process, in Section 3.2.7. By considering C_R in the later step, the controlled rocking heavy timber wall designer has some freedom in selecting R_dR_o for design. Furthermore, the designer can modify R_dR_o by considering the wind demand in the next step: R_dR_o can be increased to minimize

the design seismic demand relative to the wind demand, as long as the design wind demand does not exceed the rocking load.

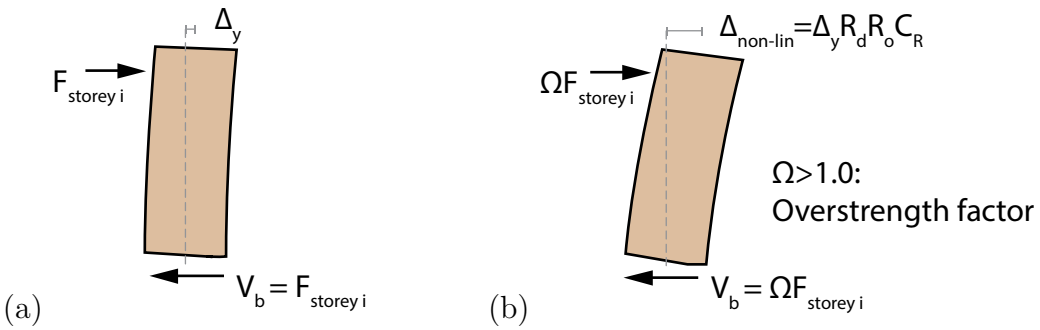

Figure 3.3: (a) Elastic displacement under design force, and (b) expected non-linear displacement

For the following controlled rocking heavy timber design, an R_dR_o of 8.0 is selected based on research that has suggested that it may be possible to control the peak displacements to within the 2.5% roof drift limit of the NBCC, with R_dR_o of 8.0. In the following step, the seismic demand is found to be larger than the wind demand; and in Section 3.2.7, $\Delta_{non\text{-}lin}$ is estimated to be below the NBCC limit of 2.5% for normal importance buildings; therefore, the resulting controlled rocking wall design could be modified in an additional iteration, and R_dR_o could be increased. However, if all other design variables are equal, the increase would be marginal over the selected R_dR_o of 8.0, so no additional iterations are considered for this prototype.

3.2.3 Calculate Seismic and Wind Demands

Seismic Demand Determination

Seismic demand is determined by distributing a design base shear value to each storey of the structure, resulting in storey shear forces and an overturning moment at the base (NRCC, 2010). The seismic overturning moment demand is important to the design of a controlled rocking wall, as this is the demand which initial post-tensioning forces are required to resist (Newcombe, 2011). The base shear to be distributed is determined by considering spectral acceleration ($S_a(T)$), tributary seismic weight (W_{trib}), and R_dR_o, in accordance with Equation 3.1 (NRCC, 2010). For the prototype design, unity is assumed for modifying factors of higher mode effects and special importance buildings (M_v and I_E, respectively). Higher mode

effects are accounted for with other methods that are specific to controlled rocking structures (see Section 3.4). $S_a(T)$ is a function of the natural period (T_n) of the prototype, assumed in Section 3.2.1. Notably, T_n estimated in Section 3.2.1 is much longer than the NBCC T_n estimate formulae, resulting in substantially lower $S_a(T)$, as shown in Figure 3.4.

$$V_b = \frac{M_V I_E S_a(T_n) W_{trib}}{R_d R_o} \qquad \textbf{Equation 3.1}$$

For Equation 3.1, W_{trib} is provided in Table 3.1 for the prototype design, and R_dR_o is discussed and identified in Section 3.2.2. For the prototype, the design base shear value (V_b) from Equation 3.1 is 420 kN, for T_n equal to 1.80 seconds.

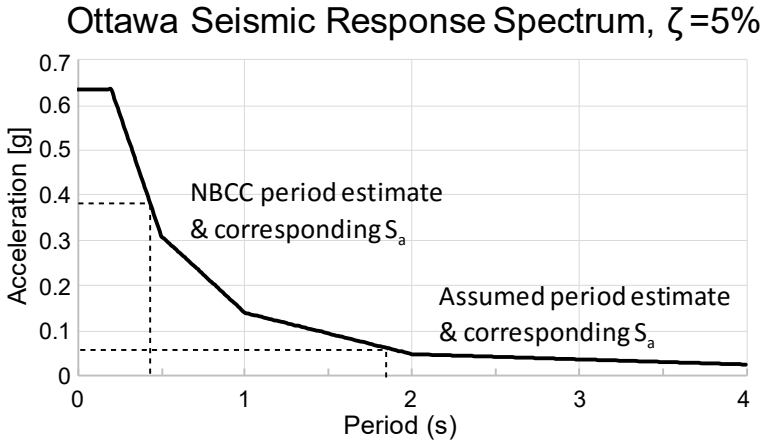

Figure 3.4: NBCC response spectrum, comparing seismic responses from two T_n estimates

Overturning moment at the base of the controlled rocking wall is a function of the design V_b: V_b is distributed over the wall height according to Equation 3.2, and overturning moments (OTM) at each storey are determined according to Equation 3.3. Given the floor height and storey weights, the base OTM for design of the prototype is 5,990 kN·m.

$$F_j = Force, storey\ j = V_b\left(\frac{W_j h_j}{\sum_{i=1}^{n} W_i h_i}\right) \quad \textbf{Equation 3.2}$$

$$OTM_j = Overturning\ Moment, storey\ j = \sum_{i=j}^{n} F_i(h_i - h_j) \quad \textbf{Equation 3.3}$$

Where $n = number\ of\ storeys$
$W = seismic\ storey\ weight$
$h_{i,j} = height\ at\ i^{th}/j^{th} storey$

Wind Demand Determination

In low-to-moderate seismic hazard regions, there is a possibility that wind demands could be larger than the design seismic demand, so the wind demands must also be checked. According to the Canadian building code (NRCC, 2010), buildings with a long period (T_n>1 s) should be analyzed by a dynamic wind analysis procedure, either involving wind tunnel experiments or a complex dynamic loading calculation requiring detailed structural damping and site specific data. To satisfy these complex analyses required by the NBCC, a more detailed wind analysis should be considered; however, the controlled rocking wall design will be selected such that seismic loading governs over the wind loading determined by the static analysis procedure, in lieu of the more complex dynamic design procedure.

The static analysis procedure is based on external pressures applied to the windward and leeward faces of a building: uniform positive and negative pressures add to a cumulative lateral force, effectively acting at half the building height. For a square building, the critical wind pressure loading case is presented in Figure 3.5. This figure includes pressure-gust coefficients (C_pC_g) which are applied in Equation 3.4 to calculate the uniform external pressures (p_e). Note that the NBCC wind loading calculations require individual C_p and C_g values to be determined for buildings taller than twenty meters, resulting in larger wind loads than for buildings under twenty meters.

$$p_e = I_w q C_e(C_g C_p) \quad \textbf{Equation 3.4}$$

Where $I_w = 1.0\ for\ Normal\ Importance\ buildings$
$q = 0.41\ kPa\ (Hourly\ wind\ pressure, 1/50\ years, Ottawa)$
$C_e = 0.7(h_{roof}/12)^{0.3}, for\ urban\ wind\ exposure$
$C_gC_p = pressure - gust\ coefficient\ (NBCC, Commentary\ I)$

The windward and leeward pressures combine to a net lateral force of 510 kN, effectively acting at half the building height. This results in a base OTM of 5,049 kN·m. There is an eccentricity of the design wind load due to gust effects at the building corners, this eccentricity is less than 3% of the building width, and so it is not considered in this thesis.

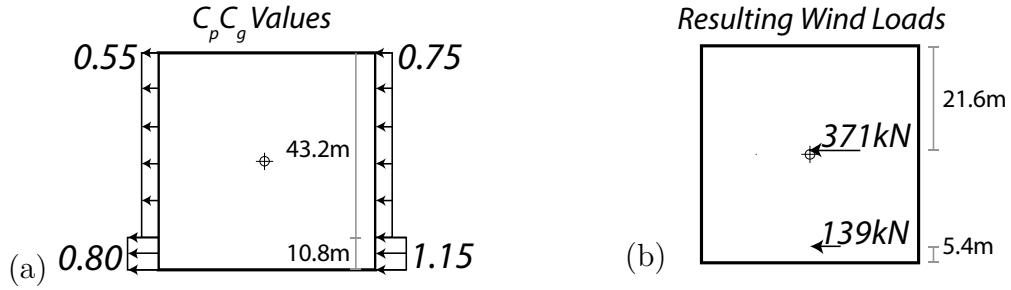

Figure 3.5: (a) Gust and pressure coefficients for wind load, and (b) resulting wind loads on prototype

Seismic and Wind Demand Conclusions

Base shear due to the static wind loading (510 kN) is greater than that from seismic loading (420 kN). However, OTM due to the seismic load distribution (5990 kN·m) is larger than that due to the static wind load calculation (5090 kN·m). Recall, the OTM is of particular importance to the design of controlled rocking walls; therefore, the seismic OTM demand is used in subsequent calculations. Base shear should be considered with respect to the design of a shear key element resisting the controlled rocking wall sliding at the base; however, the investigation of higher mode effects in Section 3.4 will present a governing base shear value for design.

The governing load decisions presented here are particularly dependent on the force reduction factor (R_dR_o) and T_n. R_dR_o can be reduced, generally resulting in a larger seismic design force. Alternatively, R_dR_o can be increased, resulting in a lower seismic design force, but the wind demand can eventually govern the design if the non-linear displacement demand does not govern first (discussed in Section 3.2.7). With respect to T_n, it is important to recall that the seismic demand is determined from an estimated value (Section 3.2.1) at this stage; after selecting the quantity of walls in the structure, T_n must be confirmed (Section 3.2.4 and 3.2.8). A shorter T_n

will increase the seismic design forces; a longer T_n will result in a lower force, resulting in the wind demand eventually governing.

3.2.4 Specify a Controlled Rocking Wall System Configuration

A certain number of controlled rocking walls is required to resist the seismic demand on the structure. This decision is dependent on an individual controlled rocking wall's ability to resist *OTM*. As such, a basic approximation of this *OTM* resistance capability is necessary, and can be made by approximating the resultant initial PT force ($T_{PT,init}$) acting at the middle of a wall, and determining the moment about a rocking toe. This calculation is shown in Equation 3.5.

$$OTM_{resist\ approx.} = \frac{l_w}{2}(T_{PT,init}) \qquad \textbf{Equation 3.5}$$

Where $l_w = wall\ length$

$T_{PT,init} = Total\ initial\ \ PT\ force$

In New Zealand, existing controlled rocking heavy timber walls have been designed with PT initially loaded to 800-1400 kN per wall, with two to four PT elements in a wall (Devereux et al., 2011; Opus International Consultants, 2014; Palermo et al., 2012). However, both Morris et al. (2012) and Yeoh et al. (2012) note that the resulting high level of stress has imposed long term creep problems, as discussed in Chapter 2. To avoid these problems in low-to-moderate seismic hazard regions, a maximum $T_{PT,init}$ of 180 kN to 220 kN is considered; and the manufacturer-standard panel length, l_w, is taken as 2.44 m (Nordic Structures, 2015). With this $T_{PT,init}$, the *OTM* resistance provided by each wall is approximately 220 kN·m to 270 kN·m. This assumes a wall configuration in which each wall shares approximately equal seismic weight. For the prototype, this means approximately twenty-two to twenty-seven walls are required (220 kN·m to 270 kN·m resisted per wall, up to 6000 kN·m total). Twenty-four walls are selected for the prototype design, and more precise moment calculations are provided in subsequent steps.

Note that with twenty-four 2.44-meter wide walls, an open architectural floor plan can easily be achieved, as shown in Figure 3.6. Larger panel lengths may also be used in design, but the 2.44 m panel is a standard size produced by manufacturers

in Canada and Europe (KLH UK, 2015; Nordic Structures, 2015). Joining two panels can be considered in future research, to develop a stiffer wall with significantly larger base connection moment capabilities.

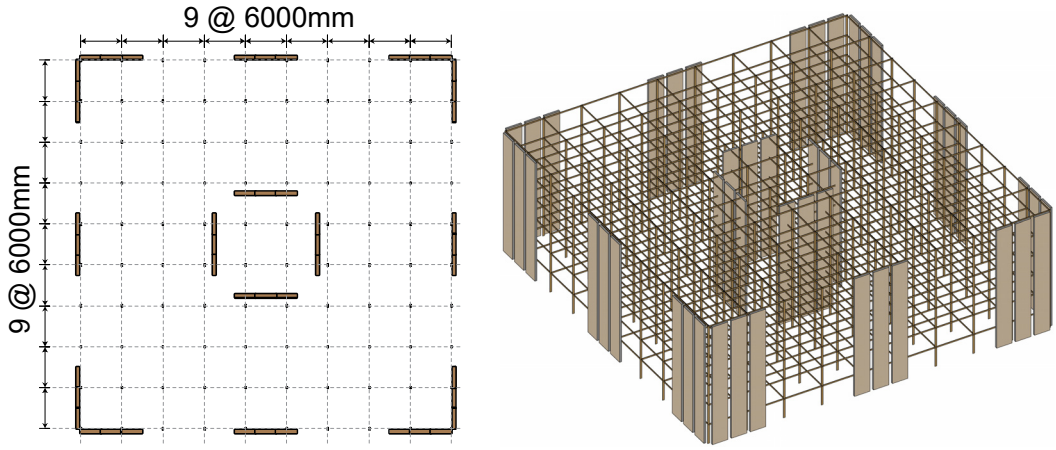

Figure 3.6: Design building archetype

3.2.5 Select Controlled Rocking Wall Panel Dimensions and PT Elements

CLT panels and PT elements are manufactured in a limited range of sizes/configurations with standard material properties. The selected elements for the prototype design are summarized in Table 3.2. Since an objective of the design process is to simplify the controlled rocking heavy timber wall design, only commercially available panel and PT elements are referenced for the prototype design, and logic for the CLT panel and PT element selection is presented below.

The chosen CLT wall panel is 315 mm thick, with properties referenced from Nordic Structure (2015), given in Table 3.2. The panel's layer configuration is suitable for a channel to be built into the middle layer for placing post-tensioning elements: the middle layer is a transverse grain layer with minimal structural importance for axial loading of the controlled rocking wall; layers are 35 mm thick, providing space for small PT elements and stability if a larger channel is needed for larger PT elements; and the outer two lamina are longitudinal layers which contribute to axial resistance of the controlled rocking wall.

The selected PT bars are 26 mm in diameter, which is the smallest commercially available bar from DYWIDAG Canada (DSI, 2015). Minimizing the size of the PT

element is important, in order to minimize the size of duct/channel required in the controlled rocking panel. Furthermore, only a small diameter should be required because the design should minimize PT forces in a low-to-moderate seismic hazard region, to avoid timber creep, PT relaxation, and frequent maintenance.

Two PT bar locations are specified, concentric about the center of the wall, each at approximately one-quarter of the wall length (see Figure 3.7). Specifying two bars, separated by approximately half the wall length, is a change from the centrally located designs in past research; however, it will help to minimize PT stress concentrations within the wall, avoiding damage to the face or edge of the wall panel (Sarti, 2015). Minimizing stress concentrations could also mitigate time-dependent creep concerns identified by Yeoh et al. (2012). Although the impact of PT stresses on wall panel creep (resulting in post-tension relaxation) was studied by Fragiacomo & Davies (2011) for LVL, resulting in a time-dependent creep model, estimating PT losses in CLT has not been studied, and presents an opportunity for further research. For the prototype, bar locations are specified from the bottom right of the wall in Figure 3.7; they are located at d_{PT2}: 620 mm and d_{PT1}: 1840 mm from the bottom right toe.

Table 3.2: Wall and Post-Tension Details

CLT Wall		Post-Tensioning (PT)	
Length, l_w	2,440 mm	Bar Diam.	26 mm
Height, h_w	19,800 mm	Area, A_{PT}	548 mm^2
Depth, t_{wall}	315 mm	E_{PT}	205 GPa
I_z	3.813 x10^{11}		
$E_{composite}$[1] (E_{CLT})	7,900 MPa	f_y	830 MPa
$f_{c,parallel\ grain}$ ($f_{c,//}$)[3]	13.03 MPa	f_{ult}	1030 MPa
$f_{v,perp.grain}$[3]	1.5 MPa		
d_{PT1}	1840 mm		
d_{PT2}	600 mm		
Density (ρ)	5.1 kN/m^3		
Shear Modulus [2]	518 GPa		
Shear Area (A_v=5/6 Cross-section)	640,500 mm^2		

[1] Composite theory (Gagnon et al., 2011)
[2] In-plane, perpendicular to outer lamina grain (Flaig, 2014)
[3] Strength considering gross cross-section

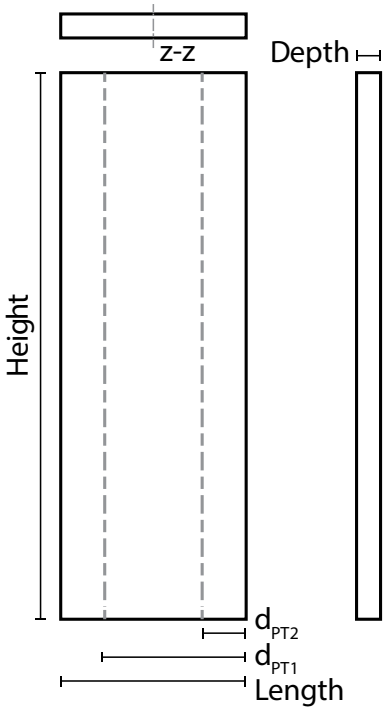

Figure 3.7: Wall diagram

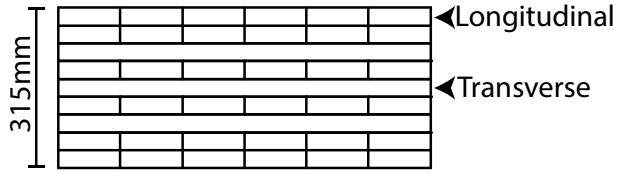

Figure 3.8: Top view of CLT panel, demonstrating layer composition; not to scale

3.2.6 Determine the Initial PT Force to Resist Seismic Forces

To resist the design OTM determined in Section 3.2.3, an initial PT force ($T_{PT,init}$) is required. The required $T_{PT,init}$ is determined by considering the connection forces at the controlled rocking wall base, and the OTM about the bottom corner of the wall when the controlled rocking system is at the peak of its linear response. The peak linear response is when the system begins to respond non-linearly to lateral load (i.e. begins rocking). When rocking begins, forces in the wall base are defined by stress conditions within the rocking toe, the wall self weight, and PT forces. To evaluate the base connection forces, a linear strain profile is assumed in the CLT

rocking toe, bound by a neutral axis (c); elastic material behaviour is assumed in the rocking toe, at the design rocking load, and can be confirmed using the base connection mechanics presented in Section 3.3. For design, the linear stress profile is represented by an effective point load (C_{CLT}) acting one third of the distance from the rocking corner, as shown in Figure 3.10 (a). C_{CLT} is a sum of the other forces acting on the wall (PT and self-weight) as shown in Equation 3.6.

$$C_{CLT} = F_{self\ wt} + 2T_{PT,init} \quad \textbf{Equation 3.6}$$

For design, the location of the neutral axis when rocking is initiated must be assumed. The logic for three possible assumptions is presented here, and reflected in Figure 3.9 for two different PT configurations. In Figure 3.9 (a), a graphic from Sarti (2015) suggests that rocking begins when c equals half the wall length. However, in discussing the technical details of controlled rocking heavy timber wall design, Sarti (2015) also recommends taking c to be 30% of the wall length (not pictured here). For prototype design in this thesis, a widely spaced PT configuration is specified (where approximately half the wall length is between the two PT elements), and c is assumed to be at the second PT element, near the rocking toe, as shown in Figure 3.9 (b). This location is equal to 25% of the wall length, which is reasonably similar to Sarti's suggestion of 30% of the wall length. The neutral axis location is important for constructing the elastic stage of a pushover curve, shown in Section 3.3.8, since it allows for an estimate of the base connection rotation when rocking is initiated, as discussed in Section 3.3. Numerical modeling of the pushover curve in Chapter 4 demonstrates the validity of the proposed assumption for the prototype evaluated in this thesis. However, the practical challenge of measuring the neutral axis depth is discussed in Section 4.2.1, and the sensitivity of the design process to this neutral axis depth assumption presents an opportunity for future research.

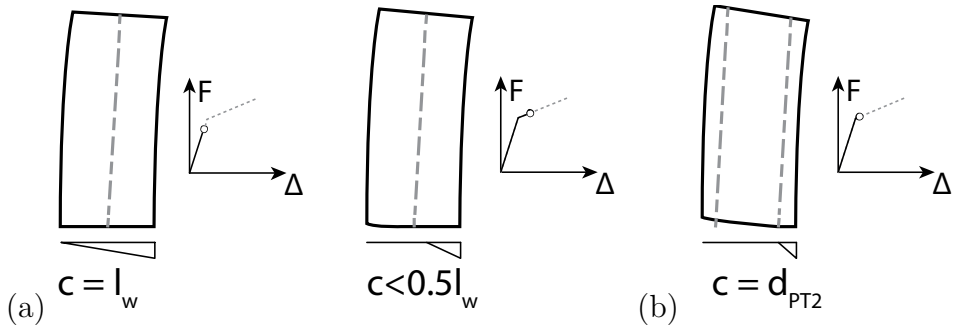

Figure 3.9: Controlled rocking heavy timber response, (a) suggested by Sarti (2015), and (b) suggested herein, for dual, widely spaced PT elements

Regarding the wall self-weight and its line of action: a very small amount of lateral drift is expected from the heavy timber panel. The total amount of drift can be analytically determined with the analysis procedure presented in Section 3.3, and confirmed by numerical modeling (Chapter 4). In both the analytical and the numerical modeling cases, the elastic bending and shear contribute very little to the lateral motion of the wall at peak drift. Because very little elastic drift occurs, the wall's self weight (Table 3.2) is simply assumed to act at the center of the wall length when the system begins rocking.

When the system begins rocking, PT elongation in the extended element (*PT1*) is countered by a minor relaxation in the element nearest the rocking toe (*PT2*) due to rocking toe compression (see Figure 3.10 (a)). This countering effect approximately balances the two PT forces; therefore, the PT force is simply taken as the initial force.

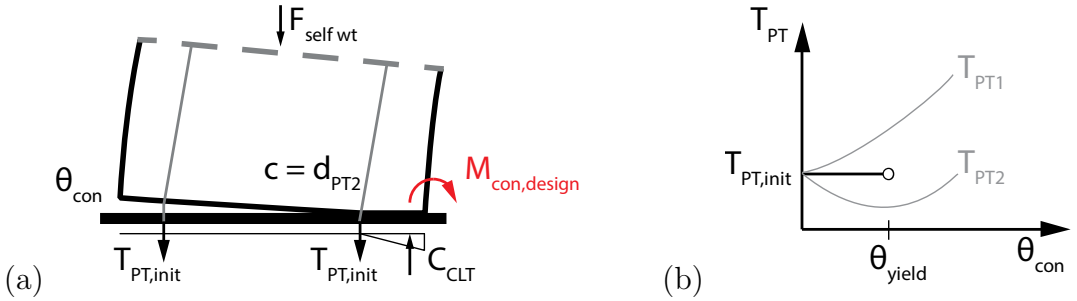

Figure 3.10: (a) Free body diagram of the controlled rocking wall base, for elastic design (b) Cumulative PT force unchanged up to the point of decompression

Finally, the CLT compression force (Equation 3.6) is factored into a moment relationship about the rocking toe (Equation 3.7) and solved for $T_{PT,init}$ (Equation 3.8). Recall that the building's seismic OTM demand (Section 3.2.3) is equally divided over twenty-four walls (Section 3.2.4), resulting in 250 kN·m demand on one wall ($M_{con,design}$).

$$M_{con,design} = F_{self\ wt}\frac{l_w}{2} + T_{PT,init}d_{PT1} + T_{PT,init}d_{PT2} - C_{CLT}\frac{c}{3} \quad \textbf{Equation 3.7}$$

$$T_{PT,init} = \frac{M_{con,design} - F_{self\ wt}\left(\frac{l_w}{2} - \frac{c}{3}\right)}{d_{PT1} + d_{PT2} - \frac{2c}{3}} \quad \textbf{Equation 3.8}$$

In the prototype, $T_{PT,init}$ is found to be 83.5 kN per PT element, referencing the properties outlined in Table 3.2 and the design base connection moment, $M_{con,design}$.

3.2.7 Check the Non-Linear Deflection

The structure's elastic deflection due to design forces must be evaluated and multiplied by both R_dR_o and Zhang's multiplier for self-centering system response, to determine a maximum non-linear deflection as discussed in Section 3.2.2. The maximum non-linear deflection is then checked against the 2.5% drift limit in the building code (NRCC, 2010).

Elastic deflection of the controlled rocking heavy timber panel can be determined from basic structural principles. However, for a simple structure like the prototype in which storey weights and heights are approximately equal, Sarti (2015) provides the derivation of a simple equation: the elastic shear and flexure deflection is simplified as a function of $M_{con,design}$ for a controlled rocking wall in which the earthquake loading distribution can be approximated as an inverted triangular distribution (equal interstorey height, H; equal seismic storey mass).

$$\delta_b = \frac{M_{con,design} H^2}{6 E_{CLT} I_z} \frac{n}{\sum_{i=1}^{n} i^2} \sum_{i=1}^{n} i^3 \left(3 - \frac{i}{n}\right) \quad \text{Equation 3.9}$$

$$\delta_s = \frac{M_{con,design}}{G_{CLT} A_v} \quad \text{Equation 3.10}$$

Where $n = number\ of\ storeys$
$I_z = moment\ of\ inertia\ of\ the\ panel$; *see* Table 3.2
$E_{CLT} = modulus\ of\ elasticity\ of\ the\ panel$; *see* Table 3.2

For the prototype, the deflection terms in Equation 3.9 and Equation 3.10 are solved using the design connection moment determined in Section 3.2.3. The resulting elastic deflection (sum of Equation 3.9 and Equation 3.10) is 10.1 mm. The elastic deflection is multiplied by the $R_d R_o$ selected in Section 3.2.2, to estimate the peak non-linear deflection of 80.8 mm according to equal displacement theory.

The additional multiplier for self-centering system displacements, by Zhang (2015) can be determined using the equation and regression coefficients first presented in Chapter 2. The tangential damping condition is considered for this calculation, as it was identified as the most conservative case, producing the largest displacement estimate (Zhang, 2015). The R term, corresponding to $R_d R_o$ in (NRCC, 2010), is 8.0; there is no energy dissipation contribution to the system response, so β is zero; and T_n was estimated as 1.80 s, as confirmed in the next step of the iterative design process. The result is a C_R equal to 2.04. Therefore, the expected non-linear deflection ($\Delta_{non\text{-}lin}$) is 164 mm, equal to 0.83% roof drift ($\theta_{non\text{-}lin}$). This non-linear deflection value is less than the 2.5% allowable drift for normal importance buildings in the Canadian building code (NRCC, 2010).

3.2.8 Check T_n of the Selected Configuration

Although T_n of the prototype was assumed in Section 3.2.1, the assumption must be checked considering the selected wall design and seismic loads associated with a controlled rocking wall in the structure. To check the assumption for the prototype, Sarti (2015) is referenced for research on T_n of a controlled rocking heavy timber wall.

As identified in Section 3.2.1, Sarti (2015) explored T_n of the controlled rocking wall through numerical modeling and experimental data. The Rayleigh method provided a good estimate of the initial period, but Sarti multiplied the Rayleigh–estimated period by 1.4 to match the numerical model's results (see Figure 3.11 and Equation 3.11). The magnified Rayleigh-period estimate accounts for an initial structural flexibility due to a flexible base connection, identified on Figure 3.11: the elastic stiffness of the controlled rocking wall is taken as the "yield-secant stiffness" (shown in Figure 3.11). This yield-secant stiffness is a function of the base connection model, which models the base connection with some degree of flexibility. Without the magnification, the Rayleigh-estimated period represents that of the controlled rocking wall with a rigid base connection.

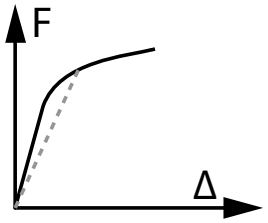

Figure 3.11: System pushover curve, including yield secant stiffness

$$T_1 = 1.4 \cdot 2\pi \sqrt{\frac{\sum_{i=1}^{n} F_i d_i^2}{g \sum_{i=1}^{n} F_i d_i}} \qquad \textbf{Equation 3.11}$$

$$d_i = \Delta \; of \; storey \; i \; due \; to \; forces, F_i$$

$$F_i = m_i g, applied \; at \; each \; storey$$

To investigate the period-estimation theory presented by Sarti, both the unmagnified Rayleigh method and Dunkerley's method were applied to the prototype design (for Dunkerley's method, see Figure 3.12 and Equation 3.12). Dunkerley's method is a variation of the Rayleigh method for approximating the natural frequency of the first mode of a multi-degree of freedom system (Chopra et al., 1997). The advantage of Dunkerley's method is that it is a simple solution, requiring only the seismic mass, and the cross-section and material properties of the selected wall panel, providing an upper bound to the T_n estimate, relative to the Rayleigh method (Chopra et al., 1997).

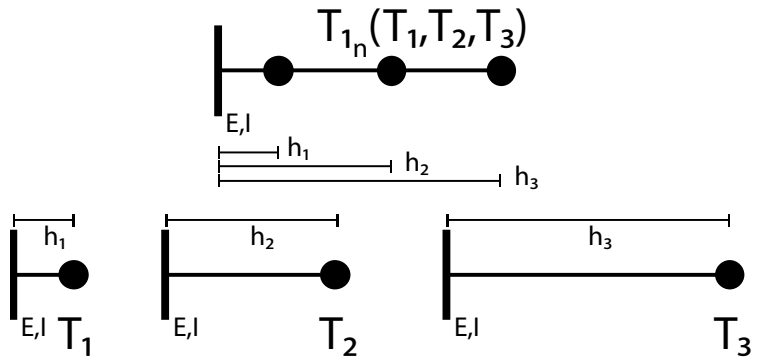

Figure 3.12: Explanation of Dunkerley's method, associated with Equation 3.12

$$\frac{1}{\omega_{1_n}^2} \approx \sum_{i=1}^{n} \frac{1}{\omega_i^2} \qquad \omega_i = 2\pi/T_{i_n} \qquad \textbf{Equation 3.12}$$

For the prototype, the results of the Rayleigh and Dunkerley methods were similar, at 1.58 and 1.61 seconds respectively. Alternatively, an eigenvalue analysis of the numerical model, presented in Chapter 4, results in a first mode T_n of 1.80 seconds. To match this result in the same manner as Sarti, a magnifier of approximately 1.12 is required. This magnifier serves the same purpose as for Sarti's model, adjusting for the yield-secant stiffness of the controlled rocking CLT wall, rather than the initial stiffness which would be analogous to a fixed cantilever. This theory can be confirmed with the numerical model presented in Chapter 4, by significantly increasing the base connection stiffness to create the same fixed-cantilever model that is assumed by the Rayleigh and Dunkerley method, and performing an eigenvalue analysis. The resulting first mode T_n (1.62 seconds) is very similar to the Rayleigh and Dunkerley estimates of 1.58 and 1.61 seconds.

There is a difference in magnifier values relating the initial stiffness to the yield-secant stiffness, between Sarti's research and the prototype design. This difference is due to the numerical modeling technique applied in the respective theses, which is discussed in Section 2.3.3. In summary, Sarti's numerical model base connection relies on spring stiffnesses that are related to the effective height of the controlled rocking wall, in accordance with a controlled rocking wall modelling analogy called the Monolithic Beam Analogy (MBA). In this thesis, the numerical model is based on the Winkler Spring Analogy (WSA), relying on spring stiffnesses with shorter

effective lengths (i.e. stiffer springs). In conclusion, these multipliers are functions of (at least) the numerical modeling technique: neither numerical model considers the base connection to be rigidly fixed. This intermediate base-fixity condition is likely true in practice, so this should be considered in evaluating T_n at the end of a design process. If modeling with the WSA however, a Rayleigh or Dunkerley method will be closer to the eigenvalue result of the numerical model than the MBA.

3.2.9 Summary of Initial Design Phase Outcomes

The seismic *OTM* demand on a prototype building was considered in the selection and design of controlled rocking heavy timber walls for the building. Twenty-four walls were selected to resist the *OTM* demand. Each wall is post-tensioned using two separated PT elements; both the wall and PT elements are summarized in Table 3.2. The required initial PT force is 83.5 kN per element (167 kN per wall) in order to resist the *OTM* demand before the controlled rocking system rocks and responds non-linearly. The maximum non-linear response is estimated to be 164 mm, or 0.83% of the wall height. All subsequent modeling assumes that the seismic storey weight is 367 kN for a floor, and 354 kN for the roof.

3.3 Analysis of Controlled Rocking Wall Response

The following sections present a controlled rocking wall analysis process, in which the base-connection response is analyzed at discrete points in the rocking stage of the controlled rocking heavy timber wall response, including at 1% and 2% roof drift, and at the initial rocking stage. The analysis is used to construct a plot approximating the wall's base shear and base connection moment response against lateral drift, shown in Section 3.3.8. The resulting pushover plot is necessary for the capacity design procedures presented in Section 3.4, and is also compared with the numerical model pushover in Chapter 4.

The pushover plot is discretized at 1% and 2% roof drift due to the base connection model: the base connection mechanics presented herein reference the Winkler Spring Analogy (WSA). At a given base connection rotation (θ_{con}), the WSA determines a base connection stiffness that is dependent upon the neutral axis depth

at that θ_{con}. The empirical relationship between the neutral axis depth and the connection stiffness adds an additional level of complexity, requiring iterations of the neutral axis depth for every different θ_{con}. A computer script could iterate through θ_{con} to produce a continuous pushover curve, including the base shear and connection moment; however, the discretized plot is efficient and matches closely with the numerical model pushover presented in Chapter 4.

The following base connection analysis process is summarized in Figure 3.13, which can be compared with a similar process by Sarti (2015). Most differences are identified in their respective steps, but some key points are highlighted here:

1. Since only two roof drift solutions are of interest (roof drift of 1% and 2%) it is necessary to evaluate the assumed rotation (θ_{con}) at the end of the process to ensure θ_{con} is associated with the roof drift (see Sections 3.3.1 and 3.3.7).
2. Any consideration for supplemental energy dissipation is excluded in this process, reducing the complexity of the structural mechanics to be considered.
3. The WSA is applied in this thesis, rather than the MBA, for modeling and analyzing stresses and strains in the controlled rocking wall base connection.

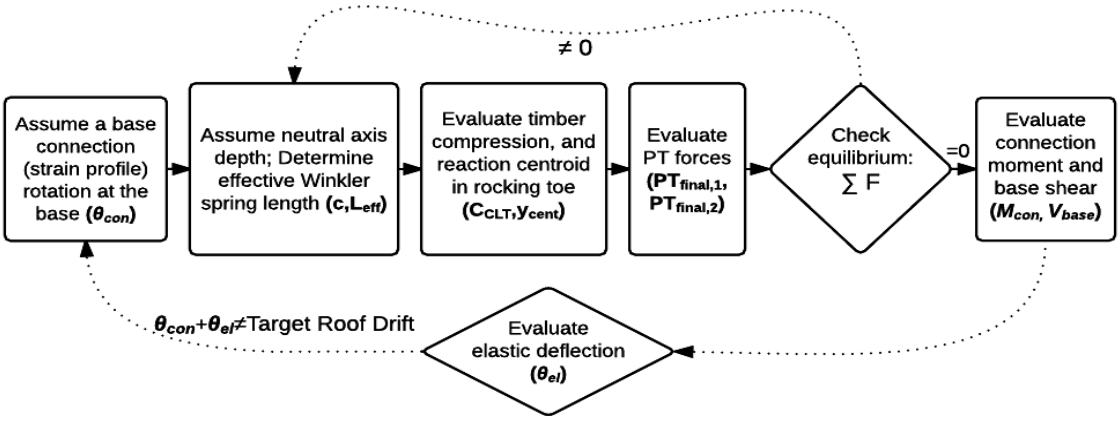

Figure 3.13: Pushover analysis process

3.3.1 Assume a Base Strain Profile Rotation (θ_{con})

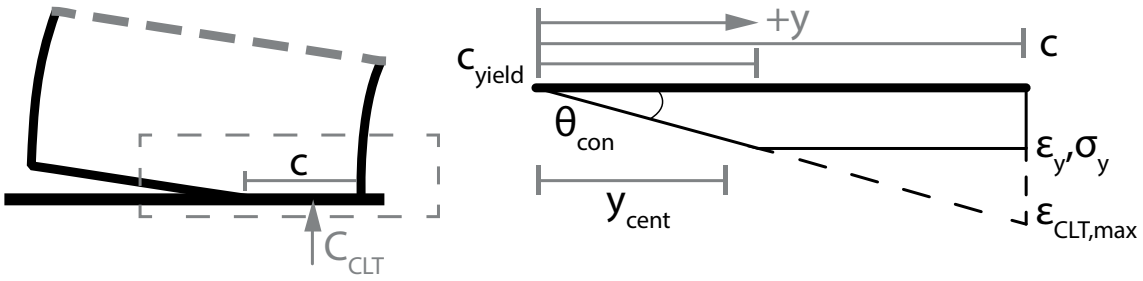

Figure 3.14: Visualizing the stress and strain profile on the rocking toe

The stress and strain profiles in the base connection interface of a controlled rocking wall can be considered as shown in Figure 3.14. In rigid body rocking with a flexible base, the θ_{con} term in Figure 3.14 is also the peak roof drift; however, this is not the case in a controlled rocking timber wall because elastic flexural and shear deformations also contribute to the roof drift (Newcombe, 2011), as depicted in Figure 3.15. The elastic deformations are not trivial to predict until a base connection response is known; therefore, the analysis procedure is conducted by assuming a θ_{con} term, and the base connection response is determined. Then the elastic drift contribution is evaluated and added to θ_{con} to determine the total roof drift. If a peak roof drift is of interest (for example, 1% and 2% roof drift), then structural mechanics can then be re-evaluated if the total roof drift does not meet the target roof drift of interest. Note that such an iteration is not necessary if a computer is iterating through a series of θ_{con} to produce a continuous pushover plot.

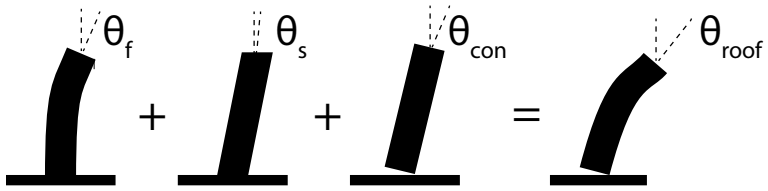

Figure 3.15: Contributions to roof drift in the non-linear stage of rocking

θ_{con} of 0.01897 radians is used for the following prototype calculations, targeting a total peak roof drift of θ_{roof} = 0.02 radians (2% of the wall height). This specific value is confirmed in Section 3.3.7, when the elastic drift is calculated. It is also compared to the numerical model testing in Chapter 4.

3.3.2 Assume Neutral Axis Depth and Determine Winkler Spring Length

The controlled rocking timber wall base can be visualized as a row of zero length Winkler springs, as shown in Figure 3.16, to understand the base connection and simplify the design and analysis procedure. An iterative process is undertaken between Sections 3.3.2 and 3.3.5 to determine the neutral axis depth (c) in the row of Winkler springs, for the current θ_{con} iteration.

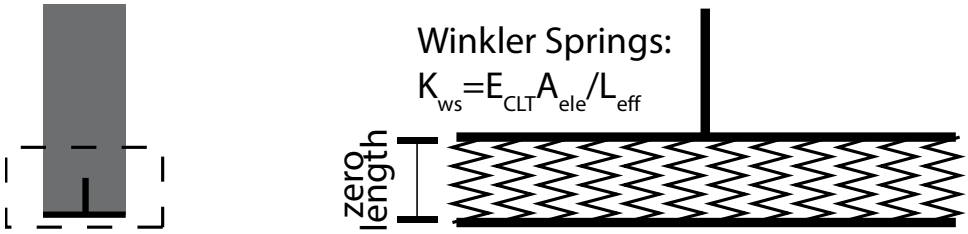

Figure 3.16: Controlled rocking CLT wall base connection visualized as row of Winkler springs

In the design process (Section 3.2), c was assumed to be located at the second PT element, closest to the rocking toe. However, in the rocking stage, c is expected to be between the second PT element and the rocking toe (consider Figure 3.7, rocking about right corner; also, Figure 3.9 (b)). An initial estimate is made for c, and an effective Winkler spring length (L_{eff}) is determined using the following empirically derived equation (Newcombe, 2015):

$$L_{eff} = 120\left(\frac{l_w}{c} - 1\right) \qquad \textbf{Equation 3.13}$$

For the following calculations, c is assumed to be 186 mm. c is checked at the end of the process, and by numerical modeling in Chapter 4. With c equal to 186 mm, L_{eff} is equal to 1456 mm.

3.3.3 Evaluate the Timber Rocking Toe Interface

A stress (σ) profile is overlaid on the associated strain (ε) profile in Figure 3.14. These stress and strain profiles are expected in the rocking toe of the CLT panel, assuming a bi-linear stress-strain relationship, as shown in Figure 2.11 (b) (Ganey, 2015). Strain in the rocking toe interface is described by Equation 3.14. Yield strength in compression is taken as CLT's compressive strength (13 MPa), and given

the yield strength, the yield strain (occurring at c_{yield}) is determined by dividing by E_{CLT}. In the prototype the yield strain is 0.00165 (Table 3.2).

$$\varepsilon_{CLT} = \theta_{con} y / L_{eff} \qquad \textbf{Equation 3.14}$$

Both c_{yield} and the maximum strain ($\varepsilon_{\mathrm{CLT,max}}$) can be determined by geometric relations. The compressive force in the rocking toe (C_{CLT}) and the effective location of that force (y_{cent}), are determined by the following relationships:

$$C_{CLT} = t_{wall} \int_0^c f_{CLT}(y)\, dy = t_{wall} \left[\sigma_y \frac{c_{yield}}{2} + \sigma_y (c - c_{yield}) \right], \quad c \geq c_{yield} \qquad \textbf{Equation 3.15}$$

$$y_{cent} = \frac{t_{wall}}{C_{CLT}} \left[\sigma_y \frac{c_{yield}^2}{3} + \sigma_y \left(\frac{c^2}{2} - \frac{c_{yield}^2}{2} \right) \right] \qquad \textbf{Equation 3.16}$$

Equation 3.15 and Equation 3.16 are derived by integrating the compression stresses over the rocking toe interface and equating the compression stress with an equivalent effective point load (C_{CLT} in Figure 3.14). These equations are limited to when the rocking toe has yielded, which is a reasonable assumption at 2% roof drift considering Newcombe's (2011) observations with LVL tests; yielding is an especially reasonable assumption given the weaker mechanical properties of CLT. For low drifts (when yielding is not expected), the principles of these equations still apply, although some modification is required to the integration in Equation 3.15, and to the moment calculation resulting in Equation 3.16.

In contrast to this section, the structural mechanics analysis by Sarti (2015) assumes there is no non-linearity in the rocking toe, even as the roof drift approaches 2%. This is a product of the Monolithic Beam Analogy (MBA), developed prior to the WSA: Newcombe (2015) demonstrated the inaccuracy of this assumption, concluding that the MBA underestimates the timber stress and strain by up to an order of magnitude, due to its reliance on a much longer effective spring length; see Section 2.3.3 for further background.

Newcombe (2011) also suggests that the effective length relationship (Equation 3.13) is only valid up to twice the yield strain. This limit should be checked at the extreme CLT fiber. It is also worth investigating Equation 3.13 in the context of

CLT panels, since finite element models and test results for LVL may not be the same for CLT, requiring a new effective length relationship. For the purpose of this thesis, the relationship is deemed acceptable, but this factor is noted for future research.

Compression in the CLT for the prototype is determined to be 503 kN, and the centroid of the compression region is 120 mm from the neutral axis.

3.3.4 Determine Post-Tension Forces

An initial PT force, $T_{PT,init}$, was previously calculated to achieve a base connection resistance of $M_{con,design}$ at the peak elastic response (Section 3.3.1). Beyond the elastic stage, PT forces must be determined from the controlled rocking wall uplift motion. Newcombe (2011) and Sarti (2015) suggested determining the uplifted PT force from the vertical elongation of the PT element at the wall base, considering the geometry depicted in Figure 3.17 (a), and Equation 3.17. The result of this simplification is evident in some of Sarti's (2015) experimental versus analytical plots: there is an underestimation of PT forces compared to the experimental data. This underestimation is identified by the measure lines in Figure 3.17 (b).

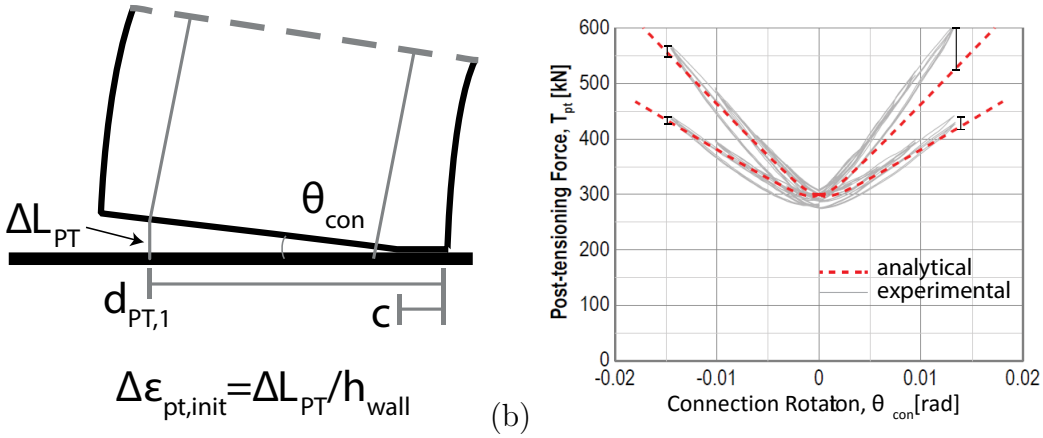

Figure 3.17: PT elongation (a) diagrammatically, (b) demonstrating underestimation of the analytical method

$$\Delta y_{PT,i} = \theta_{con} \cdot (d_{PT,i} - c) \qquad \textbf{Equation 3.17}$$

Since a lower PT force is expected in the PT elements for low-to-moderate seismic hazard regions, the underestimation observed in previous studies could be

significant relative to the overall PT forces. In response, a more detailed PT elongation analysis is proposed here, relying on the neutral axis depth, base connection rotation, horizontal drift, initial PT force, initial wall shortening, and basic geometric relations. The vertical PT elongation is the same as presented by Newcombe (2011) and Sarti (2015); however, the horizontal drift was neglected in previous studies.

Horizontal displacement is calculated from the expected peak drift, as per Equation 3.18.

$$\Delta x_{PT} = \theta_{target\ roof\ drift} \cdot h_{wall} \qquad \textbf{Equation 3.18}$$

Wall shortening is also considered, as shown in Equation 3.19, based on the static stress state (self-weight and initial PT).

$$\Delta_{CLT,relax} = \frac{2T_{PT,init} + F_{sw}}{A_{wall}E_{CLT}} \cdot h_{wall} \qquad \textbf{Equation 3.19}$$

It is reasonable to question the inclusion of the CLT relaxation term in the change of length calculation: the initial PT shortening is accounted for in the installation of the PT element, as the wall shortens before the PT is locked. However, comparisons of the analytical expectations and numerical model results show a better match when the term is included, as shown in Figure 3.18. In particular, including the relaxation term reduces the final PT forces slightly, such that one PT force underestimates the numerical model, and the other overestimates the model (±2%). This over- and underestimate balances the total PT force on the analytical system. Since the total PT force is referenced in subsequent base force calculations, this balance is beneficial. In physical testing, rocking toe compression and wall bending effects should be investigated to understand this phenomenon.

Three deformation values now define the horizontal and vertical translation of the top PT node, between the initial loading state and the target roof drift (Equation 3.17-Equation 3.19). Equation 3.20 is applied to approximate the change in PT length by adding the resultant of these translation vectors and subtracting the original length. Equation 3.21 defines the final PT force, given the approximated

change in PT length. For the prototype at θ_{con}=0.01897 rad, the first and second PT forces are 279 kN and 146 kN respectively (see Table 3.3).

$$\Delta L_i = L_{final,i} - L_{init} = \sqrt{(h_{wall} - \Delta_{CLT,relax} + \Delta y_{PT,i})^2 + \Delta x_{PT}^2} - h_{wall} \quad \textbf{Equation 3.20}$$

$$PT_{final,i} = PT_{init} + \frac{\Delta L_i}{h_{wall}} \cdot A_{PT} E_{PT} \quad \textbf{Equation 3.21}$$

Where $i = PT\ element\ identifier\ (1\ or\ 2)$

Table 3.3: Post-tension calculation variables and results

	PT#1 (i=1) (Furthest from rocking toe)	PT#2 (i=2) (Closest to rocking toe)
Δx_{PT}	396 mm	396 mm
Δy_{PT}	31.4 mm	7.85 mm
$\Delta_{CLT,relax}$	0.80 mm	0.80 mm
ΔL_i (Δy_{PT}, Δx_{PT}, $\Delta_{CLT,relax}$)	34.6 mm	11.0 mm
$T_{PT,init}$	83.5 kN	83.5 kN
PT_{final}	279 kN	146 kN

The PT_{final} estimate presented here is meant to be a closer prediction of PT forces, given the underestimation presented by the earlier approximation (Figure 3.17 (b)). This underestimation can affect other parts of the analysis as well, since subsequent sections (including the iteration of c) rely on PT_{final}. It is also important to minimize error in the PT force estimate given the relatively small design PT force in a low-to-moderate seismic hazard region compared to that required in a design for higher seismicity.

A comparison of PT_{final} estimates is shown in Figure 3.18, for the wall and PT properties provided thus far; the numerical model result is taken as the reference value. The PT_{final} estimate by Newcombe (2011) and Sarti (2015) is clearly the lower bound, whereas the estimate presented in this thesis (including wall shortening) bounds the PT force estimates from the reference case by +/-2.5%. The cumulative force matches the numerical model and, as shown in Chapter 4, leads to excellent neutral axis estimation relative to the numerical model with Winkler springs.

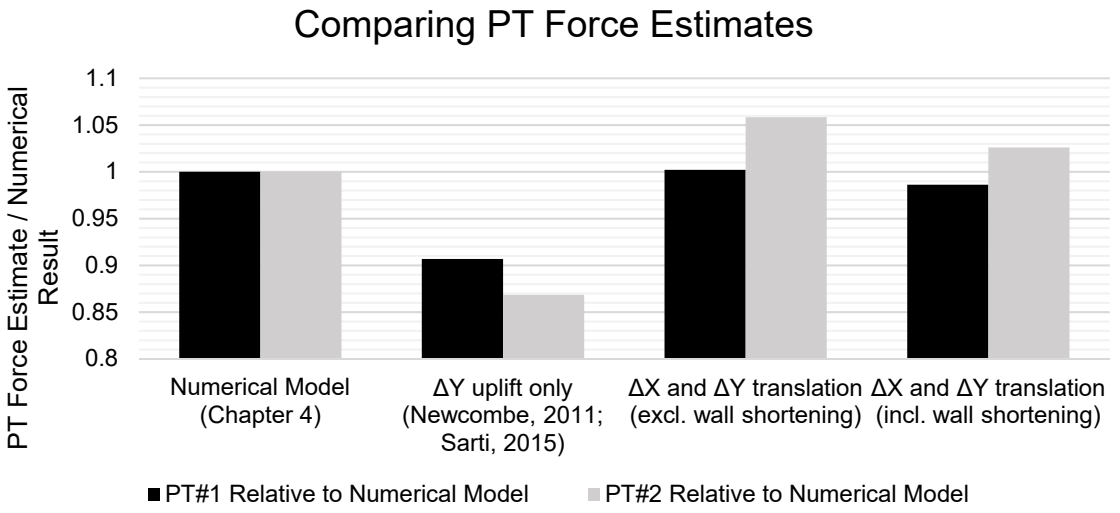

Figure 3.18: Comparing PT Force Estimates with Numerical Model Results

3.3.5 Check Force Equilibrium at the Connection Interface

Rocking toe compression, post-tensioning, and wall self-weight are combined, seeking force equilibrium at the connection interface. If equilibrium is not achieved, Sections 3.3.2-3.3.5 must be reiterated to converge on a satisfactory neutral axis depth (c) for the current θ_{con}. This iteration for c can be performed quickly in a spreadsheet, before moving out of this iteration loop. For the prototype, this equilibrium is confirmed with the final iteration of c equal to 186 mm, given θ_{con} equal to 0.01897 radians.

3.3.6 Calculate Connection Moment and Base Shear

Moment contributions are determined by considering the post-tensioning PT elements, wall self-weight (F_{sw}), and CLT compression region in the context of the controlled rocking wall system. These values were identified for the prototype in the previous sections, and are depicted in Figure 3.19.

During the non-linear stage of the controlled rocking wall response, base connection moment response (M_{con}) is determined by taking the moments about the middle of the base; the equation is provided in Equation 3.22. In this equation, the self-weight and CLT compression force terms can increase or decrease the connection moment term, depending on the direction of rocking taken for the analysis. PT forces

at the top of the wall are broken into their respective components, as shown in Figure 3.19. In recent controlled rocking heavy timber studies, only the vertical component is considered in the M_{con} equation; however, the horizontal component is a significant portion of the resulting M_{con} at 2% roof drift in the prototype, as seen in Table 3.4.

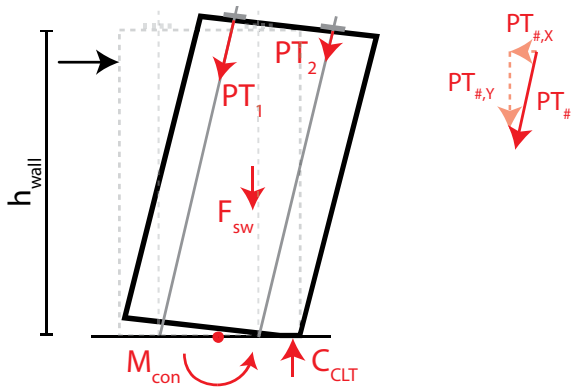

Figure 3.19: Controlled rocking wall forces and connection moment during non-linear rocking, assuming the roof is rocking to the right; includes example lateral forces

$$M_{con} = C_{CLT}\left(\frac{l_w}{2} - c + y_{cent}\right) + PT_{final,1,Y}\left(d_{PT1} - \frac{l_w}{2}\right) - PT_{final,2,Y}\left(\frac{l_w}{2} - d_{PT2}\right) + (PT_{final,1,X} + PT_{final,2,X}) \cdot h_{wall} - F_{sw}\frac{(\theta_{target\ roof\ drift} \cdot h_{wall})}{2} \quad \textbf{Equation 3.22}$$

F_{sw} only includes the wall self-weight, as per discussion in Section 2.3.3: various connection details have been proposed to ensure displacement compatibility between the uplifting wall and the associated floor beams, and these connections allow the wall to uplift independent of the rest of the building. F_{sw} is taken mid-way between the roof drift and the middle of the base, effectively assuming the wall's center of gravity will drift half as far as the roof. In the first mode response, most of the motion is rigid body rocking, so this is a reasonable assumption. For the prototype, the resulting M_{con} is 810 kN·m. The contributing moment values are presented in Table 3.4.

Table 3.4: Connection moment contributions (non-linear rocking stage)

Moment Contribution			% of M_{con}
M_{CLT}	575	kN.m	71%
$M_{PT,2,Y}$	-90	kN.m	-11%
$M_{PT,1,Y}$	171	kN.m	21%
$M_{PT,2,X}$	57	kN.m	7%
$M_{PT,1,X}$	109	kN.m	14%
M_{SW}	-15	kN.m	-2%
M_{con}	810	kN.m	100%

Equation 3.22 calculates the base connection moment, as did Equation 3.7 in the initial design phase. In the initial design phase however, the rigid body motion (θ_{con}) was assumed to be negligible, so only the initial vertical post-tensioning force was used in the M_{con} calculation. Furthermore, Equation 3.7 takes the moments about the bottom corner of the wall, while Equation 3.22 takes moments about the center of the wall base; either point is acceptable.

Finally, M_{con} is used to determine the controlled rocking wall base shear (V_{base}) at the current rocking state, θ_{con}, using Equation 3.23. In the prototype, V_{base} is determined to be 57.3 kN with an effective height of 14.24 m.

$$V_{base} = \frac{M_{con}}{H_{eff}} \qquad \textbf{Equation 3.23}$$

Where $H_{eff} = \frac{\sum_{i=1}^{n} m_i h_i^2}{\sum_{i=1}^{n} m_i h_i} = \text{effective SDOF height}$

3.3.7 Determine Total Roof Drift (Flexure and Rocking)

As identified in Section 3.3.2, a small portion of the roof drift is due to elastic flexure and shear in the timber panel (elastic drift, θ_{el}). The largest component, due to rigid body rocking, was assumed in Section 3.3.1 and relied upon in Sections 3.3.2 - 3.3.6 to determine the resulting connection moment and base shear (M_{con} and V_{base}).

Sarti's (2015) deflection analysis calculation, which was applied in Section 3.2.7 to determine θ_{el} at the initial rocking state (Equation 3.9-Equation 3.10), is recalled here in Section 3.3.7 to determine θ_{el} at the roof due to M_{con}, given the current θ_{con}.

The resultant θ_{el} in the prototype design, according to this method, is 0.167% of the wall height (0.00167 radians). θ_{con} was assumed to be 1.897% of the wall height (0.01897 radians), so the total roof drift is 2.06% of the wall height (0.0206 radians). This is 3% larger than the 2% roof drift targeted for the analysis. Although the difference is small, the following discussion will explore this finding further.

Considering a free-body diagram of the controlled rocking heavy timber wall with widely-spaced PT elements (Figure 3.20 (a)), a force-imbalance is realized at the top of the wall. The imbalance is especially apparent in Figure 3.20 (b), the representative figure for the numerical model. The imbalance causes a uniform moment over the height of the wall (M_{PT}), as shown in Figure 3.20 (c), resulting in elastic bending opposite the direction of wall rocking. This bending contribution motivates a modification to Sarti's method which leads to an alternative elastic bending drift estimate.

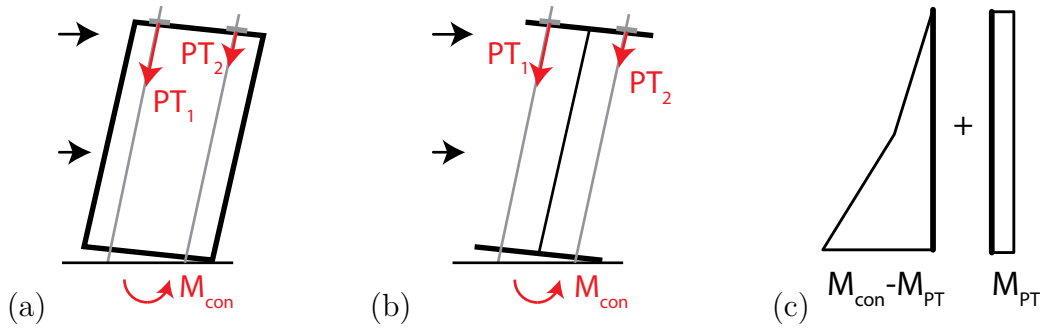

Figure 3.20: (a) Controlled rocking wall, considering PT force couple and connection moment; (b) numerical model representation (Chapter 4); (c) moment diagrams related to elastic bending

The proposed modification builds on Sarti's derivation of bending and shear drift due to seismic forces at the floor levels, and adds a bending drift term ($\theta_{PT,roof}$) which acts opposite to the direction of rocking:

$$\theta_{el} = \left[\frac{\delta_b + \delta_s}{h_w}\right] - \theta_{PT,roof} \qquad \textbf{Equation 3.24}$$

M_{PT} is concentrated at the top of the wall, and is calculated from the different PT forces located concentric about the center of the wall. The concentrated moment is calculated as:

$$M_{PT,roof} = (PT_{final,1} - PT_{final,2})d_{cent} \quad \text{Equation 3.25}$$

Where $d_{cent} = distance\ to\ PT\ from\ center\ of\ wall$

$PT_{final,1} > PT_{final,2}$

The direction of the PT moment causes bending in the opposite direction of the rocking motion, since the first PT to extend due to uplift is larger than the PT closest to the rocking toe (see Figure 3.17). Given the moment due to the PT imbalance concentrated at the roof, the drift at the roof is calculated from structural mechanics of a cantilever beam:

$$\theta_{PT,roof} = M_{PT}\frac{h_w}{2E_{CLT}I_z} \quad \text{Equation 3.26}$$

In the prototype, M_{PT} is determined to be 82.7 kN·m (10% of the connection moment in the current θ_{con} iteration, near 2% roof drift), and $\theta_{PT,roof}$ due to this PT couple is 0.0272%, opposing θ_{el} and resulting in a total estimated elastic drift of 0.140% of the wall height. In total, the roof drift is 2.03% of the wall height. This total roof drift is only 1.5% larger than the target, in contrast to 3.0% larger in the initial analysis estimate, and is considered close enough for a final iteration. Note that for the prototype, θ_{el} was calculated using M_{con} whereas M_{PT} should be subtracted from this value for a more rigorous application of this theory.

The lower modulus of elasticity associated with CLT, and the wider spaced PT elements proposed in this design, can result in more pronounced effects due to bending by the top-of-wall PT moment, relative to LVL specimens.

3.3.8 Pushover Plot Construction

The initial design phase (Section 3.2) and subsequent analysis of the controlled rocking wall in the rocking stage (Section 3.3) resulted in several key base shear and overturning moment values for the prototype design. These values occur when rocking is initiated, and at 2% roof drift, whereas the estimated peak non-linear drift for the prototype was 0.83%. These values are sufficient for a designer to construct a three-point pushover curve (including a point at the origin) which is necessary for the application of the capacity design procedures presented in Section 3.4. However,

the base connection mechanics principles applied in Section 3.3 can also be used to determine several other response values at key points in the rocking stage, including the contribution of rocking drift at the initial rocking state, and at an intermediate point like 1% roof drift. These additional points have been calculated and are used to construct a pushover curve for comparison with the pushover response from a numerical model in Chapter 4.

The calculated data points for the pushover plots are summarized in Table 3.5; the pushover plots are shown in Figure 3.21. Note that the initial rocking state is a combination of elastic deflections (Section 3.2.7) and rigid body rotation, which can be determined with the base connection mechanics principles of Section 3.3.

Table 3.5: Summary of pushover data points, determined in Sections 3.2-3.3

	Roof Drift, Δ (θ_{roof})	Base shear, V_b	Base connection moment, M_{con}
Initial State (Stationary)	0 mm (0 radians)	0 kN	0 kN·m
Initiation of Rocking (Design Response)	14.1 mm (0.712×10^{-3} radians)	17.5 kN	250 kN·m
1% Roof Drift	198 mm (0.01 radians)	34.6 kN	493 kN·m
Peak Roof Drift (Rocking)	402 mm (0.0203 radians)	57.3 kN	816 kN·m

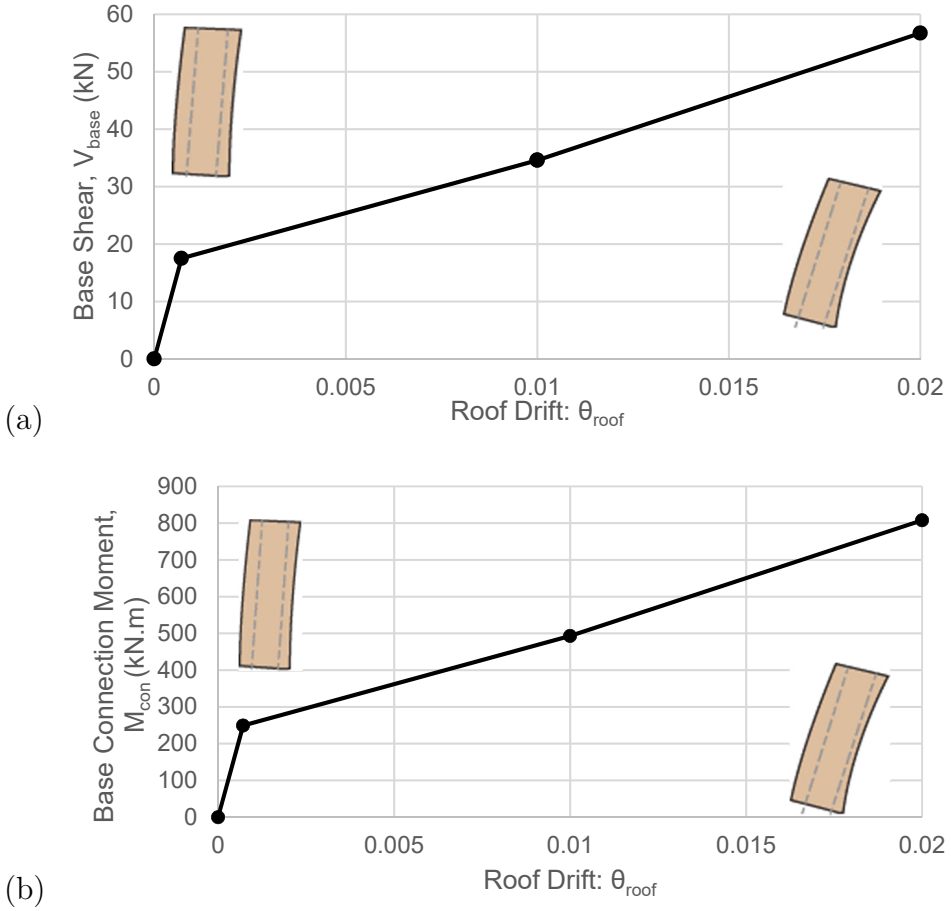

Figure 3.21: Prototype design pushover curves (a) base shear, and (b) base connection moment, versus roof drift

3.4 Capacity Design: Considering Higher Mode Effects

The design process presented thus far considers the first mode response to dominate the controlled rocking wall behaviour. By this process, the largest bending moment and shear demands are at the base of the wall, and therefore the timber panel's bending moment and shear strength capacities would be checked against these demands. However, Newcombe (2011) and Sarti (2015) found that higher modes of vibration also affected the controlled rocking wall's response, especially by imposing larger shear force and bending moment demands above the base of the wall. These findings are consistent with other controlled rocking systems, such as controlled rocking steel braced frames (Lydell Wiebe et al., 2015b), as discussed in

Section 2.4.2. Therefore, to evaluate the influence of higher modes on a controlled rocking heavy timber wall, a dynamic procedure, an equivalent static force (ESF) procedure, and a cantilevered beam analogy (CBA) are outlined here, based on research for the capacity design of controlled rocking steel braced frames: the dynamic and equivalent static force procedures were presented by Steele & Wiebe (2016), building on the theory for the CBA which was first presented by Wiebe & Christopoulos (2015). These procedures are applied to the prototype model to evaluate the peak higher mode demands, and these estimates over the wall height are compared with the numerical modeling results in Chapter 5.

3.4.1 Dynamic Procedure

The dynamic procedure relies on a simplified model of the controlled rocking system in which the boundary conditions are modified to those during rocking, as this is the state in which the peak response is observed. The model can be constructed in a commercial software engineering package, using boundary conditions as shown in Figure 3.22 (a), including a pin at the base corner to simulate rocking about the toe, and linear springs at the top-of-wall PT anchorage. The initial PT loads, determined in design, are placed on the linear springs. The wall is represented by beam elements between each storey, representing the shear and bending properties of the timber panel. These beam elements run along the centerline of the model, and rigid elements are used to connect the centerline to the rocking toe at the base, and the PT linear springs at the roof level. By defining the model in this manner, the rocking loads and higher mode effects can be captured with a static loading configuration and response spectrum analysis, respectively.

The first mode (rocking) response is imposed on the controlled rocking wall model using the equivalent static forces from the design procedure. The loads are magnified by an overstrength factor (Ω) to consider overstrength effects at a maximum state of response in rocking; the response of interest occurs when the wall is at the maximum expected non-linear displacement, $\Delta_{non\text{-}lin}$. Ω is determined by dividing M_{con} when the roof drift is equal to $\theta_{non\text{-}lin}$ (i.e. $\Delta_{non\text{-}lin}$ divided by the wall height), by $M_{con,design}$. These values are given in the pushover curve from the analysis

process, and are shown in Figure 3.22 (b). For the prototype model, $\theta_{non\text{-}lin}$ is 0.83%, corresponding to M_{con} of 450 kN·m, and $M_{con,design}$ is 250 kN·m; therefore, Ω is 1.80.

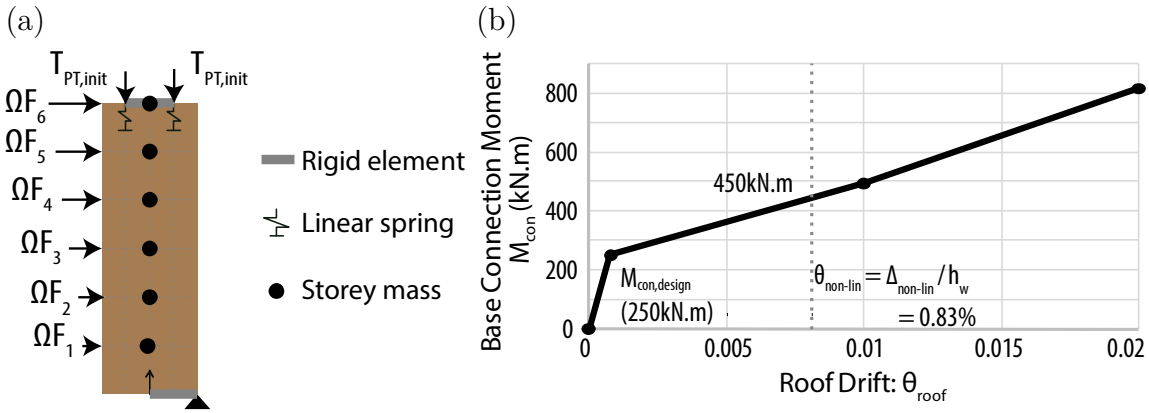

Figure 3.22: (a) Dynamic model; (b) Overstrength factor determined from pushover curve

Higher-mode effects are considered using a response spectrum analysis in which the response spectrum is truncated between the first and second mode period (T_n and T_2, respectively), since the first mode response is accounted for with the static loading. T_n is determined in the design process, and T_2 is determined by a modal analysis. For the prototype design, T_n and T_2 are 1.80 s and 0.36 s, respectively.

The magnified static response (r_1) and the response spectrum analysis results (r_2 and r_3) are combined according to Equation 3.27, in which r_2 and r_3 are combined using the square root of the sum of the squares (SRSS) combination method.

$$r_{total} = r_1 + \sqrt{r_2^2 + r_3^2} \qquad \textbf{Equation 3.27}$$

The response spectra for the prototype analysis are presented in Chapter 5, after the discussion of ground motion selection and scaling. However, the mean of the spectra presented in Chapter 5 is considered here, to determine the peak prototype shear force and bending moment demand for the purpose of capacity design in the controlled rocking CLT wall: the result of the dynamic method is a peak shear force demand of 335 kN, and a peak bending moment demand of 1,780 kN·m. The resulting envelope is shown in Figure 3.23.

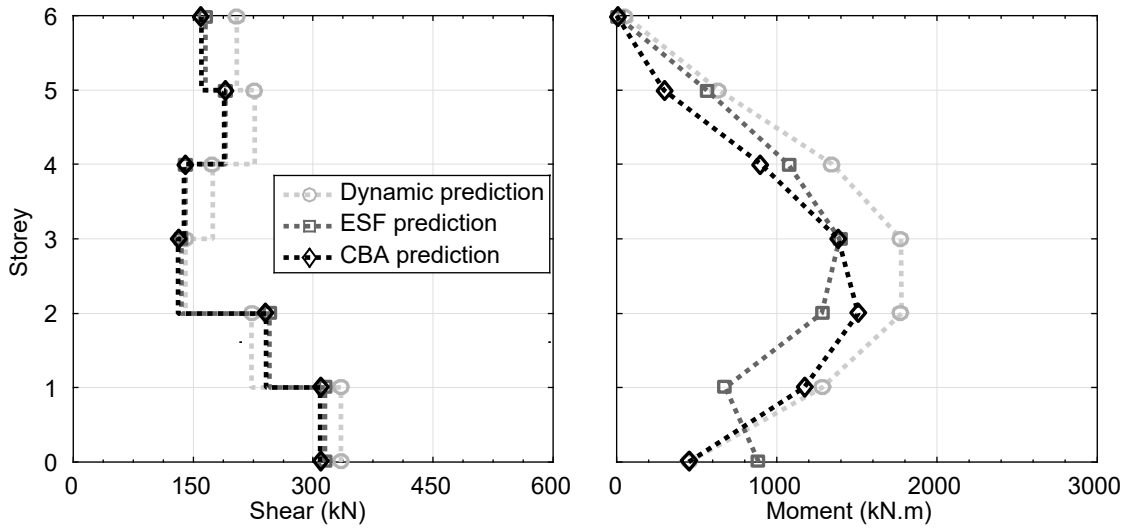

Figure 3.23: Higher mode estimates

3.4.2 Equivalent Static Force Procedure

The equivalent static force (ESF) procedure uses a fixed base model of the controlled rocking wall, with ESF's to account for the first three modes of vibration. The ESF model can be constructed in a commercial software engineering package. Unlike the model for the dynamic method, the ESF model does not require a modification of the boundary conditions. Furthermore, because the model does not capture uplift, it does not require springs for the PT elements. The model uses beam elements to represent the wall panel, including the shear and bending properties of the timber. The beams are fixed at the base of the wall, and rigid beams connect the beams to nodes where the PT is anchored at the roof level. Because no PT springs are used, and the ESF model does not capture uplift, the maximum PT loads expected in the system are manually imposed at the PT nodes, as determined through the rocking analysis procedure (Section 3.3).

Similar to the dynamic method, the inverted triangular load distribution from the base connection design process (Section 3.2.3) is applied to the wall model and magnified by Ω to account for the first mode response. The higher mode forces are defined by Equation 3.28 and Equation 3.29, derived by Steele & Wiebe (2016) from modal contribution equations presented by Wiebe & Christopoulos (2015) which are described in the CBA (Section 3.4.3). Steele & Wiebe (2016) discretized the modal

force contributions by integrating the modal contributions over each storey, and placing the load at the top of each storey. The result is an ESF at each storey, for each higher mode, described as a function of the acceleration response spectrum at the higher mode periods ($S_a(T_2)$ and $S_a(T_3)$), the tributary seismic weight (W_{trib}), the number of storeys (N), the mid-heights of each storey ($h_{mid,i}$), where i is the storey number, and the total wall height (h_w).

$$F_{2,i} = 0.569 S_a(T_2) \frac{W_{trib}}{N} \sin\left(\frac{4.49 h_{mid,i}}{h_w}\right) \quad \text{Equation 3.28}$$

$$F_{3,i} = 0.229 S_a(T_3) \frac{W_{trib}}{N} \sin\left(\frac{7.73 h_{mid,i}}{h_w}\right) \quad \text{Equation 3.29}$$

The higher mode periods can be calculated by modal analysis of either a multi-spring model (described in Chapter 4), a modified model like that used in the Dynamic Method (Section 3.4.1), or a fixed-base model. The multi-spring model is the most complex method, but is useful for non-linear time-history analyses as well. The dynamic method is relatively simple, whereas the fixed-base model is the simplest model. However, the fixed-base model does not account for the flexibility of the controlled rocking wall base, so a modification is needed for the modal analysis results. This phenomenon was investigated by Wiebe & Christopoulos (2015a), and non-dimensional modifiers were presented for the natural periods of flexural and shear beams; the modifiers are plotted for the spectrum of fixed to pinned base fixity in Figure 3.24. Assuming the controlled rocking heavy timber wall to be a flexural beam without rotational restraint at the base, the non-dimensional T_2 and T_3 modifiers are 1.43 and 1.23, respectively; since no rotational restraint is assumed, these modifiers are an upper bound estimate. The modal analysis results of the fixed base model can be modified by these factors and applied to Equation 3.28 and Equation 3.29. In the prototype model, modal analysis results from the multi-spring model, described in Chapter 4, are used for following ESF calculations: T_2 and T_3 are 0.38 s and 0.13 s, respectively.

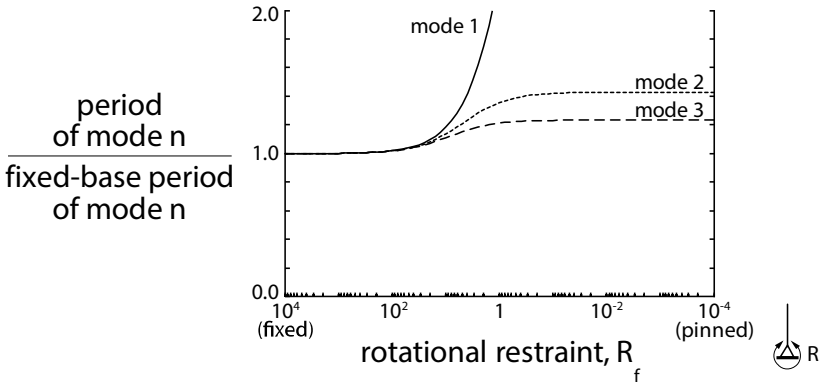

Figure 3.24: Effect of base fixity on modal periods of a flexural beam, modified from (Lydell Wiebe et al., 2015a)

The higher mode ESF's are added to the model to determine the higher mode responses; these are combined by the SRSS combination method, and added to the response due to the first mode force. The resulting shear and bending moment responses over the height of the wall represent the maximum system response due to rocking and higher mode effects.

The response spectra for the prototype analyses are presented in Chapter 5, after the discussion of ground motion selection and scaling. However, as with the dynamic procedure, the mean of the spectra is used to determine the peak prototype shear force and bending moment demand: the result of the ESF procedure is a peak shear force demand of 315 kN, and a peak bending moment demand of 1,390 kN·m, as shown in the design envelopes in Figure 3.23. Note that Figure 3.23 shows a relatively large base connection moment, estimated by the ESF procedure. This is explained by the discretized forces by Steele & Wiebe (2016). The discretized forces are located at the top of each storey; therefore, the moment contribution for the first storey is lumped at the height of the first storey, resulting in non-zero base connection moment from higher mode effects. However, this finding does not affect the capacity design procedure, because the base connection moment can simply be taken as the overstrength base connection moment (r_1), and because the higher modes increase the bending moment demand above the base, governing the design.

3.4.3 Cantilever Beam Analogy

The cantilever beam analogy (CBA) determines the peak force demand on a controlled rocking system using closed-form equations that describe modal bending moment and shear force contributions at a height, z, on an analogous cantilever beam (Lydell Wiebe et al., 2015b). The closed-form equations are non-linear functions of $M_{con,design}$, the total wall height (h_w), and $S_a(T_2)$ and $S_a(T_3)$. T_2 and T_3 were estimated using modal analysis of a multi-spring model, as discussed in Section 3.4.2. The modal contribution equations are summarized in Equation 3.30-Equation 3.35, including the overstrength factor Ω on the first mode response. After determining the modal contributions using these equations, the higher mode responses are combined with the SRSS combination method, the same as in the previous two procedures (see Equation 3.27). Considering the prototype design, the CBA estimates a peak shear demand of 310 kN and a peak bending moment demand of 1,510 kN·m. The resulting envelope is shown in Figure 3.23.

$$V_{1,max} = \frac{3}{2}\left(\frac{\Omega\, M_{con,design}}{h_w}\right)\left[1 - \frac{z}{h_w}^2\right] \quad \text{Equation 3.30}$$

$$V_{2,max} = 0.1265\, S_a(T_2)\left(\frac{W_{trib}}{g}\right)\left|\cos\left(4.49\left(\frac{z}{h_w}\right)\right) + 0.217\right| \quad \text{Equation 3.31}$$

$$V_{3,max} = 0.0297\, S_a(T_3)\left(\frac{W_{trib}}{g}\right)\left|\cos\left(7.73\left(\frac{z}{h_w}\right)\right) - 0.1283\right| \quad \text{Equation 3.32}$$

$$M_{1,max} = \Omega M_{con,design}\left[1 - \frac{3}{2}\frac{z}{h_w} + \frac{1}{2}\frac{z}{h_w}^3\right] \quad \text{Equation 3.33}$$

$$M_{2,max} = 0.0282\, S_a(T_2)\left(\frac{W_{trib}}{g}\right)h_w\left|\sin\left(4.49\left(\frac{z}{h_w}\right)\right) + 0.976\frac{z}{h_w}\right| \quad \text{Equation 3.34}$$

$$M_{3,max} = 0.00384\, S_a(T_3)\left(\frac{W_{trib}}{g}\right)h_w\left|\sin\left(7.73\left(\frac{z}{h_w}\right)\right) - 0.991\frac{z}{h_w}\right| \quad \text{Equation 3.35}$$

3.4.4 Strength Capacity of the Timber Panel

The controlled rocking heavy timber wall bending capacity is defined as the effective bending strength ($f_{b,eff}$) multiplied by the section modulus (S), and the shear capacity is defined as the effective shear strength ($f_{v,eff}$) multiplied by the shear area

of the gross wall section (A_v). A_v, $f_{b,eff,}$ and $f_{v,eff}$ are defined in Table 3.2, for the prototype design; S is a function of the cross section geometry identified in Table 3.2. The resulting shear force and bending moment capacities are 960 kN and 5,900 kN·m, respectively; these capacities are much larger than the peak demands estimated by the dynamic and ESF procedures, and the CBA. Considering the shear demand, the dynamic, ESF, and CBA estimations correspond to 35%, 33%, and 32% of capacity, respectively. Considering the bending moment demand, the dynamic, ESF, and CBA estimations are 30%, 24%, and 36% of capacity, respectively.

Despite the apparent reserve capacity in the prototype controlled rocking wall, timber engineers are still investigating the bending and shear properties of CLT: the in-plane shear and bending strength and stiffness values used in the capacity calculation are specified by the manufacturer based on research with small-scale specimens, such as beams and lintels (Gagnon et al., 2014). The performance of larger scale specimens like the nine-layer, 2.44 m wall in the prototype design, requires additional research to verify the strength capacity.

3.5 Summary of Design and Analysis

A prototype controlled rocking CLT structure was proposed for the region of Ottawa, Canada, without supplemental energy dissipation. In the prototype design, twenty-four walls are used in each principle orientation, with CLT panels that are summarized in Table 3.2. Considering a seismic hazard with a 2% probability of exceedance in 50 years, the design results in a natural period of 1.80 seconds, corresponding with a seismic base shear of 17.5 kN and a design overturning moment of 250 kN·m. The base overturning moment is resisted by a compression response in the CLT panel base, in addition to PT forces and the wall's self-weight. To maintain an elastic system response to the overturning moment, an initial PT force of 83.5 kN is required in two PT elements, 26 mm in diameter. The elements are located symmetrically, 620 mm from the centerline of the wall, in order to minimize stress concentrations in the timber, mitigating long term periodic maintenance due to timber creep (see Figure 3.7).

In the event of a design-level seismic event, the peak roof drift of the resulting design is estimated to be 164 mm, or 0.83% roof drift, which is well below the 2.5% limit by the NBCC (NRCC, 2010). Given the low drift estimate, the wall's response was analyzed up to only 2% drift in Section 3.3. At 2% drift, the neutral axis at the controlled rocking wall base is approximately 186 mm (7.6% of the wall length) from the extreme fiber of the rocking toe, resulting in maximum PT forces of 279 kN and 146 kN respectively, where the maximum is 61% of the PT bar's yield stress. This is notably less than the maximum forces in designs for higher seismic hazard regions, which can have initial PT forces of more than 200 kN per bar, and yield under the maximum considered earthquake scenario (Newcombe, 2011; Sarti, 2015). Furthermore, at 2% drift, the connection moment in the wall increases to 810 kN·m, and the base shear to 57.3 kN.

Finally, three higher mode estimation procedures were referenced from controlled rocking steel braced frame research, to estimate the influence of higher modes on the controlled rocking heavy timber wall. The procedures are referred to as the dynamic and equivalent static force (ESF) procedures, and the cantilever beam analogy (CBA). The shear force and bending moment demand estimates from the dynamic, ESF, and CBA procedures are 335 kN, 315 kN, and 310 kN and 1780 kN·m, 1390kN·m, and 1510 kN·m, respectively. The CLT panel's shear force and bending moment strength capacities are, respectively, 960 kN and 5900 kN·m, corresponding with shear demand ratios of 35%, 33%, and 32%, and bending moment demand ratios of 30%, 24%, and 36% of capacity for the dynamic, ESF, and CBA procedures, respectively. The results are shown in Figure 3.23, although the capacities are much larger than the bound shown in the plot. These results demonstrate consistent peak demand estimates by the three procedures which were originally presented for controlled rocking steel braced frames. Furthermore, the peak demand estimates are conservatively below the strength capacity of the controlled rocking wall.

4 Numerical Modelling

This chapter presents the numerical model development and validation for a controlled rocking CLT wall. The key features of the numerical model are outlined first, and are validated by modeling an experiment presented by Sarti (2015) and comparing the results. A variation of the model is also presented as a lower-bound of Sarti's experimental data, considering physical effects that could affect the system parameters. After validation against the experimental data, the chapter focuses on the prototype controlled rocking CLT wall designed in Chapter 3: the numerical model is analyzed in a pushover process and the results are compared with the pushover plot presented at the end of Chapter 3. Finally, damping models for controlled rocking heavy timber walls are investigated, and a damping model is applied to the numerical model of the controlled rocking wall prototype.

4.1 Numerical Model Development

The controlled rocking heavy timber wall numerical model in this work is built in OpenSees (Mazzoni et al., 2006), referencing the numerical models presented by Ganey (2015) and Sarti (2015). Unlike these studies, the model presented in this thesis uniquely relies on the Winkler Spring Analogy (WSA) presented in Newcombe (2011, 2015) to capture the behaviour of the controlled rocking wall base connection as a series of springs providing vertical stiffness. The WSA model defines the base connection stiffness as a function of the wall material properties and the design and analysis outcomes, whereas the methods presented by Ganey (2015) and Sarti (2015) require calibration to experimental data which is unavailable for the CLT design outlined in Chapter 3. Further general advantages to the WSA are discussed in Section 2.3.3.

The general wall model is outlined first, followed by a focus on the Winkler Spring base construction. This outline is generic to controlled rocking heavy timber walls. Subsequent sections present the material properties and dimensions to be applied to the model.

4.1.1 General Controlled Rocking Heavy Timber Model Construction

The numerical model is composed of the controlled rocking heavy timber wall and a leaning column, through which P-Delta effects from the gravity system are imposed on the wall. The wall and leaning column are presented as two parts of the general model, in Figure 4.1. These two parts are composed of (a) elastic Timoshenko beam elements, (b) rigid elastic beam columns (rigid elements), (c) truss elements, and (d) elastic beam columns; this is in addition to the elements describing the base, discussed in Section 4.1.2.

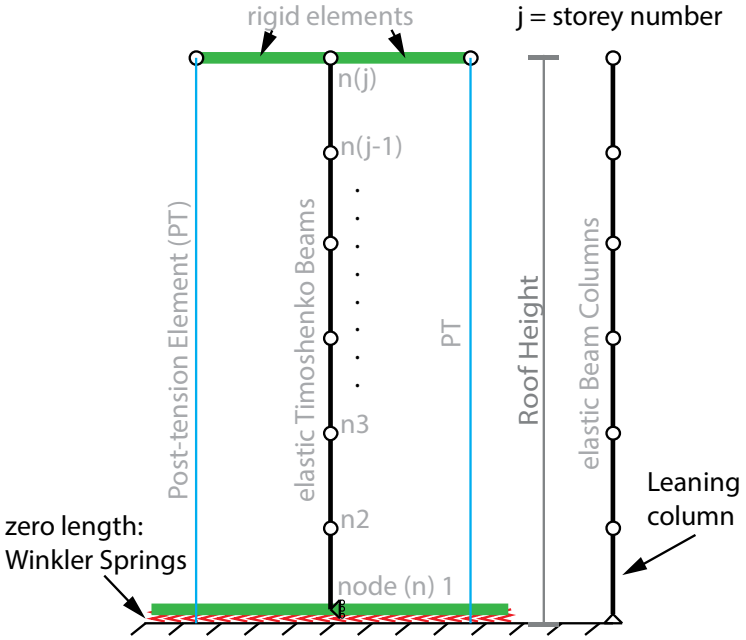

Figure 4.1: General numerical model, including node and element labels for reference

Elastic Timoshenko beam elements describe the heavy timber panel between storeys. These elements have both shear and bending properties associated with their response, as well as axial stiffness. Elastic Timoshenko beam elements remain elastic, which is deemed reasonable based on the observations from past controlled rocking LVL and CLT research (Ganey, 2015; Sarti, 2015), and the capacity design (Section 3.4) which suggested a capacity of three times the demand.

Rigid elastic beam column elements connect the top of the wall elements, (node *j*) with the post-tensioning (PT) elements; they are also implemented in the Winkler

Spring base (Section 4.1.2). Elastic beam column elements are similar to elastic Timoshenko beam elements, but do not have shear deformations associated with them. Furthermore, these particular elements are assigned large bending and axial stiffness properties.

Corotational truss elements are used to represent PT elements in the controlled rocking wall. The corotational truss element captures the changes in the system geometry which result in different force components as the PT element rotates. These elements are assigned the Steel02 material property in OpenSees, which captures yielding and plastic strain effects (Filippou et al., 1983). Steel02 also allows an initial stress value to be set, for post-tensioning the controlled rocking wall.

The leaning column is composed of elastic beam column elements. This element is the same as type (b), and has axial and bending stiffness components. However, instead of large stiffness properties like the rigid elastic beam column elements, the assigned axial stiffness reflects that of the gravity system components (columns) on which the tributary seismic mass is supported; furthermore, the leaning column's bending stiffness is negligible as the wall panel is assumed to be the only significant contributor to lateral force resistance.

4.1.2 Winkler Spring Base Modeling

The Winkler Spring base is shown in a minimized format in Figure 4.1, and expanded upon in Figure 4.2. This base is built with a finite number of spring elements: a larger quantity of fibers allows for a better representation of the stress and strain profile at the base, and an easier understanding of the neutral axis depth as the base rocks and uplifts, however the quantity of springs increases the computational time of the analysis procedure. An investigation is performed in Chapter 5, considering this parameter. Each Winkler Spring is connected at one end with a rigid beam column element, described in Section 4.1.1. These rigid elements are connected in series, and transfer forces from the wall elements through a node (*n1*) that is common to both Figure 4.1 and Figure 4.2. *n1* is locked in its horizontal degree of freedom, acting as a rigid shear key at the base.

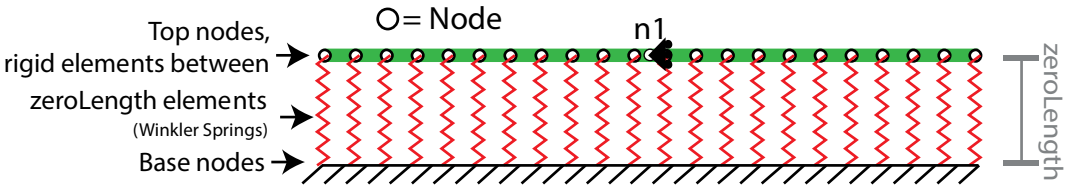

Figure 4.2: Winkler Spring base

The Winkler Springs are defined by zero length elements in OpenSees, and the material behaviour of the element is defined by an elastic perfectly plastic gap material: springs do not have any stiffness in tension, and the compression stiffness is constant until yielding at the compression strength of the CLT. For the numerical model presented in this work, the approximate compression yield point is taken as the compression strength of the timber. However, there is a limited amount of research available on the axial compression behaviour of CLT; therefore, further timber research is recommended to understand how to model the true compressive behaviour at the base of the CLT rocking wall. The numerical model material behaviour is presented in Figure 4.3, including the damage captured by the elastic perfectly plastic gap material, resulting in residual strains over multiple cycles of rocking.

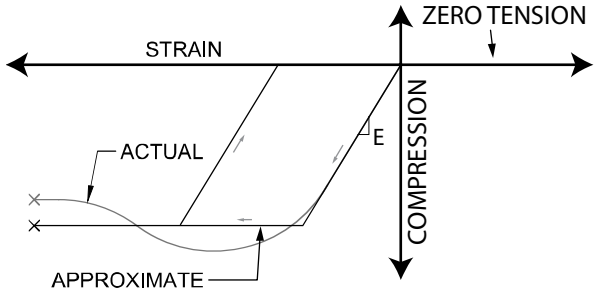

Figure 4.3: Controlled rocking wall base material behaviour in compression

Newcombe (2015) suggested that the ideal Winkler Spring model would allow for a variable connection stiffness, modifying the Winkler Spring stiffness for each new c determination. However, this is computationally difficult to implement within OpenSees, since c is not directly observable in the analysis results, and would have to be recalculated for each analysis step. Therefore, as noted in the analysis process in Chapter 3, the base connection stiffness is given in Equation 4.1, in which L_{eff} is

defined by a constant effective Winkler Spring length (Equation 3.13) where the neutral axis depth (c) is determined at a peak expected roof drift.

$$K_{Winkler\ Spring} = \frac{E_{timber} A_{spring}}{L_{eff}} \qquad \textbf{Equation 4.1}$$

Where $$A_{spring} = \frac{l_{wall} t_{wall}}{number\ of\ springs}$$

4.2 Numerical Model Validation

To validate the numerical model described in Section 4.1, the model is constructed and configured to match an experimental specimen tested in a previous study. As described in Section 4.1, all model parameters are chosen based on the reported physical test properties, with no empirical calibration.

4.2.1 Comparing With Sarti's (2015) Experimental Program

The selected experimental program for validating the numerical model is a controlled rocking LVL experiment presented by Sarti (2015). The experimental wall configuration is summarized in Table 4.1 and Figure 4.4; these are the "baseline" properties. Sarti (2015) outlines a PT-only test, in which the initial PT force is 200 kN (100 kN per PT element). High resolution plots are also available on which analytical and numerical model outputs can be overlaid. Notably, several of the wall configuration/material property values are inconsistently identified; these are noted in Table 4.1 and Figure 4.4, along with the selected values for model validation.

Table 4.1: Wall and Post-Tension Details

LVL Wall (Sarti, 2015)		Post-Tensioning (Sarti, 2015)	
Length, l_w	1,570 mm	**Bar Diameter**	32 mm
Height, h_w[1]	4,000 mm	**Area, A_{PT}**	804 mm^2
Depth, t_{wall}	190 mm	**E_{PT}**	170 GPa
E_{timber} (E_t)	11,000 MPa	**f_y**	830 MPa
$f_{c,parallel\ grain}$ ($f_{c,//}$)[2]	45 MPa	**f_{ult}**	1030 MPa
Density (ρ)	5.1 kN/m^3	**$L_{unbonded}$[3]**	Height+1 m = 5 m
Shear Modulus	550 GPa		
Shear Area (A_v=2/3 Cross-section)	198,870 mm^2		

[1]Actual panel height is 4100 mm: Drawing no. 1/11 (Sarti, 2015)
[2]Sometimes identified as 38 MPa: p.160, p.308 (Sarti, 2015)
[3]Extra meter of strained PT is unbonded below the wall and in the PT devices above the wall: p.309 (Sarti, 2015)
[4]Point loads possibly located at 1895 mm and 3895 mm from base: Drawing no. 1/11 (Sarti, 2015)

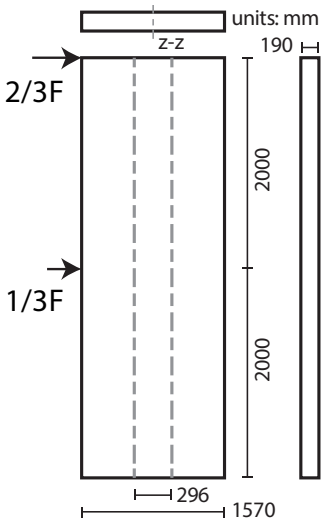

Figure 4.4: Sarti's experimental wall specimen[4]

Given the baseline configuration identified above, analysis is conducted according to the process outlined in Chapter 3 to estimate the wall response (i.e. neutral axis depth, base shear, connection moment and rotation) at both 1% (40 mm) and 2% (80 mm) roof drift. The results of the analysis process are summarized in Table 4.2, referred to as the "analytical model", and the data points are plotted in Figure 4.5. Next, the numerical model is tested in a quasi-static process, pushed to 2% drift (80 mm) at the top of the wall, as per Sarti's experimental test. Therefore, the effective length (L_{eff}) of the Winkler Spring is determined from the wall length and neutral axis depth (c) as per Equation 4.1, considering c when the wall is at 2% roof drift. The result is an L_{eff} of 856 mm, and effective Winkler spring stiffness of 3833 kN/m, divided by the number of base connection fibers in the model. The resulting quasi-static response data is presented in Figure 4.5, overlaid on Sarti's experimental data.

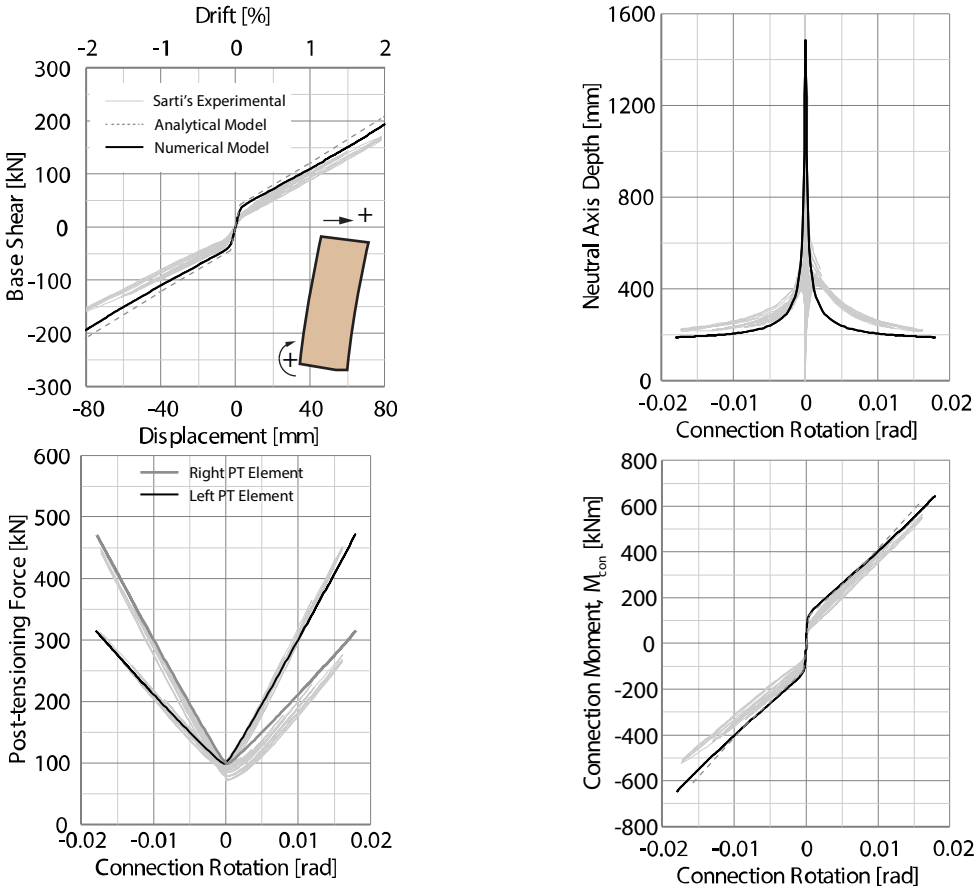

Figure 4.5: Comparing numerical model and analytical results with experimental data from Sarti (2015)

Table 4.2: Key analytical, numerical, and experimental data points

	Analytical	Numerical	Experimental	
	Result @ Wall Uplift			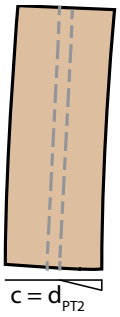
Neutral Axis Depth (mm), c	637mm	685mm	unknown	
Base Shear (kN), V_b	41	35	+25/-40 [1]	
Connection Moment (kNm), M_{con}	118	105	+90/-120 [1]	
Roof Displacement (mm)	~2	~2	~5	
	Result @ 1% Roof Drift			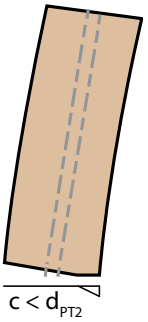
Neutral Axis Depth (mm), c	204	211	250-300 [2,4]	
Connection Rotation (rad)	0.0081	0.0088	unknown	
Base Shear (kN), V_b	120	110	80-110 [4]	
Connection Moment (kNm), M_{con}	340 [3]	367	330-370 [4]	
	Result @ 2% Roof Drift			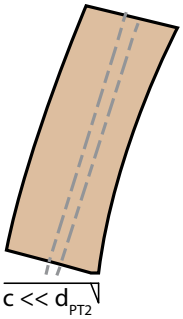
Neutral Axis Depth (mm), c	193	191	210-230 [2]	
Connection Rotation (rad)	0.0165	0.0176	0.016-0.017	
Base Shear (kN), V_b	215	191	150-175	
Connection Moment (kNm), M_{con}	620	636	520-550	

[1] Variance in rocking direction

[2] Overestimated due to experimental process; see discussion below

[3] Determined based on initial PT of 100 kN per bar. Used base connection moment calculation from Section 3.2.6 with initial PT, rather than to determine a PT for a target moment resistance.

[4] Variance due to hysteresis in experimental data

The overlaid plots in Figure 4.5, and the related key data points in Table 4.2 have several similarities and differences which are discussed individually, below. Note that the following discussion suggests several physical factors that may not be captured by the baseline numerical model. The combination of these factors is considered in Section 4.2.2.

Point of System Non-linearity: Rocking Load

For the purpose of this analysis, the wall uplift point (defining the rocking load) in the experimental and numerical data is an approximation of the largest value before the response curve becomes non-linear. Given this definition, the rocking load determined from the analysis process (analytical model) slightly overestimates the numerical model, due to the non-linearity of the numerical model response (41 kN and 35 kN of base shear, respectively; also, 118 kN·m and 105 kN·m base connection moment, respectively). However, the rocking load in the experimental specimen demonstrates a degree of variability, as seen in the base shear and connection moment plots where the system response becomes non-linear. In the negative rocking direction, the rocking load of the experimental specimen appears to closely match the analytical and numerical models; but it underestimates that load in the positive direction by as much as 25%. This discrepancy may be exaggerated by some minor unspecified asymmetry in Sarti's specimen, since the wall response presents an apparent intermediate stiffness, between the initial and rocking stiffness, for a small portion of its positive roof displacement/connection rotation response; this asymmetric intermediate stiffness response is not present in Sarti's other tests (Sarti, 2015).

Post-Uplift Stiffness

The post-uplift stiffness is reflected in the slope of the base shear and connection moment plots of Figure 4.5. Post-uplift stiffness is similar in all three cases (analytical, numerical and experimental), although a growing discrepancy can be seen at larger drifts (more than 1.5% roof drift). The phenomenon is also identified by Sarti, and can be attributed to the development of a softening response related to the wall where the PT elements are anchored: concentrated PT forces locally compress the experimental wall specimen, causing a deformation at the top of the wall which reduced the PT forces and the lateral response (Sarti et al., 2015c). This reduction effect is not accounted for in the analytical or numerical models, and in fact it is an objective of the design process (Chapter 3) to minimize this effect through an alternate, widely-spaced PT configuration and relatively large force

reduction factor. Physical testing is needed to provide further insight on this post-uplift stiffness discrepancy for the design proposed in this thesis.

Sarti (2015) also suggests that repeated cyclic testing softened (damaged) the rocking toes of the wall panel. It is expected that this softening affects the connection response by reducing the rigidity of the base corners, and consequently, reducing the post-uplift rocking stiffness.

For a better understanding of the effect of a damaged rocking toe, the material stiffness was reduced for several rocking toe fibers in the numerical model. The reduction is summarized as a 70% axial stiffness reduction within 80 mm of the edge of the wall (i.e. 40% of the neutral axis depth expected at 2% drift, for which the Winkler spring effective length is defined in the numerical model). The resulting quasi-static test data is presented in Figure 4.6. By reducing the stiffness to simulate a rocking toe with some minor damage, the post-uplift stiffness was reduced. The reduction in post-uplift stiffness, shown in Figure 4.6, helps to address the numerical model's overestimation of the base shear and connection moment at peak roof drift.

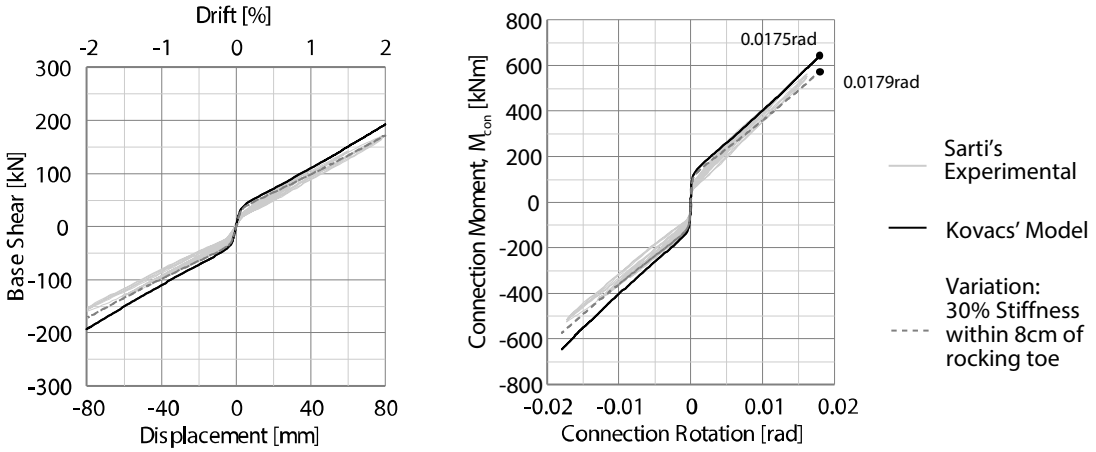

Figure 4.6: The effect of a damaged rocking toe on the connection and system response

Post-Tensioning Forces

Figure 4.5 shows that the general PT response in the numerical model matches that of the experimental model, although the peak PT forces are larger in the former due to the larger connection rotation (discussed in the next subsection).

Furthermore, a hysteresis is observed in the experimental response, reducing the PT force with subsequent cycles (the numerical model was only subjected to a single cycle, since none of the elements behaved inelastically). This PT force reduction through hysteresis can be attributed to the plastic timber strains observed in the experimental program: plastic deformations were observed under the top-of-wall PT anchorage due to concentrated PT stresses, so PT losses of as much as 25% are observed in the experimental test (Sarti et al., 2015c). Neither the analytical nor the baseline numerical model currently capture these PT losses due to compression deformations at the top of the wall. Therefore, to capture this effect, the PT material is redefined to include losses due to timber panel deformations. The modified system seeks to capture some hysteresis due to timber crushing below the top-of-wall PT anchorage. The result of this modification is evident in the PT force-deformation relation presented in Figure 4.7 and the modified PT material specifications are included in Table 4.3.

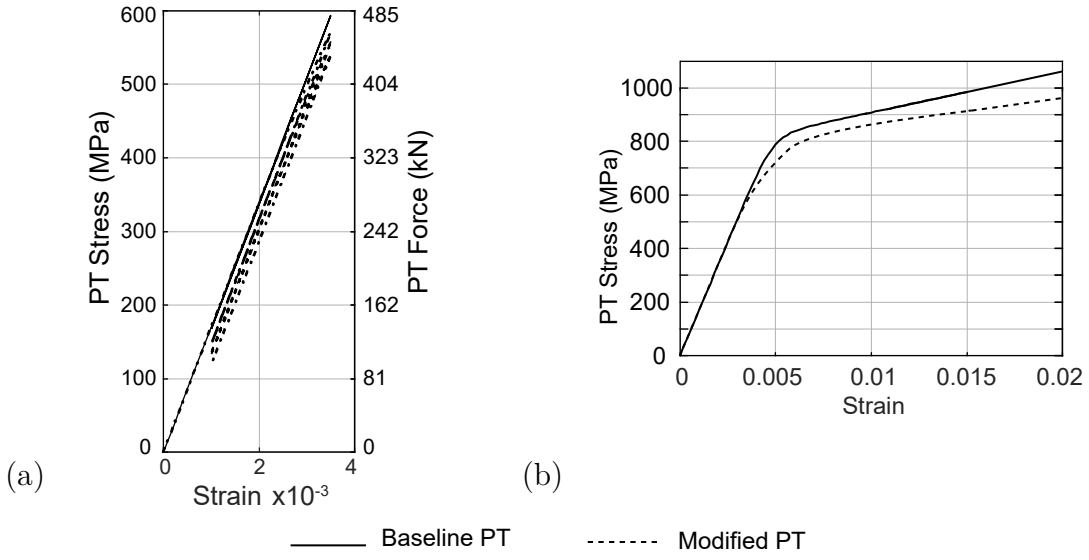

Figure 4.7: PT (a) hysteresis, and (b) response to large strain, for baseline and modified PT elements

Table 4.3: Numerical model PT specifications

OpenSees *Steel02* Material		
Property	**Baseline**	**Lower-bound**
E (GPa)	170	170
F_y (MPa)	830	830
Strain Hardening Ratio, b	0.09	0.05
R_0	10	4.5
C_{R1}	0.925	0.925
C_{R2}	0.15	0.15
a_1	0	0
a_2	1	1
a_3	0	0
a_4	1	1

Considering the response of the whole system: the numerical model was evaluated with the modified PT properties and a reduced initial PT force (30% reduction) under the quasi-static test sequence presented in (Sarti, 2015) (see Figure 4.8). The system response is overlaid on the experimental and numerical model response under the full 200 kN (100 kN/element) initial PT load, in Figure 4.9. The reduced PT force contributes to a better match with the experimental data at peak drift, lowering the peak base shear and connection moment. Furthermore, the modified PT properties result in some minor hysteresis, reflecting the experimental response.

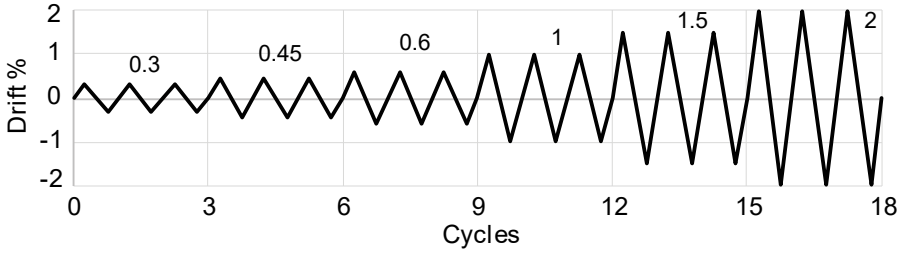

Figure 4.8: Displacement protocol applied to evaluate lower-bound numerical model

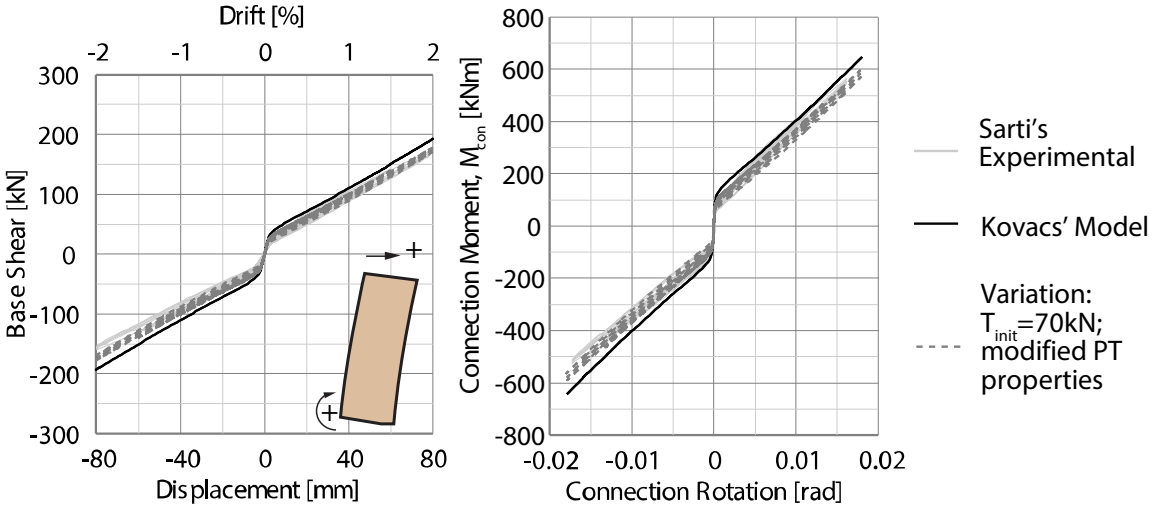

Figure 4.9: Effects of a reduced initial PT force on the connection and system response

Recall that an objective of the design process for this thesis (Chapter 3) is to minimize the potential for PT loss by specifying a widely-spaced PT configuration that minimizes concentrated PT stresses, and considering design for low-to-moderate seismic hazard regions. Physical testing of this proposed configuration is needed to provide insight on the potential for PT losses under this proposed design configuration, since the PT calibration above is only considering the PT forces in Sarti's experimental system.

Elastic and Connection Rotation Contributions to Lateral Drift

A roof drift of 2% (80 mm) was applied to all the models presented in Figure 4.5. This drift is a combination of rigid body rotation and elastic flexibility of the panels, as discussed in Section 3.3.1. Despite equal roof drifts, different connection rotations are observed in the numerical and experimental cases at 2% drift (see Table 4.4), suggesting that the numerical model is elastically stiffer than the experimental specimen by as much as 38%.

Table 4.4: Roof drift contributions, as read from Figure 4.5

	At 2% Roof Drift	
	Numerical Model	**Experimental Model**
Connection Rotation Contribution	~1.75%	~1.6-1.7%
Elastic Drift Contribution	~0.25%	~0.3-0.4%

Sarti's (2015) numerical model (not shown) similarly underestimated the elastic drift of the controlled rocking wall. Sarti suggested that the experimental wall's apparent flexibility may be attributed to some minor lateral timber compression at the rocking toe shear key, as the test progressed. Such a lateral compression would result in the lateral translation of the system, reducing the slope of the base shear versus roof displacement plots (seen in Figure 4.5). Furthermore, this minor lateral motion would not be recorded as a connection rotation, ultimately suggesting some additional elastic flexibility in the quasi-static test. These concepts are depicted in Figure 4.10.

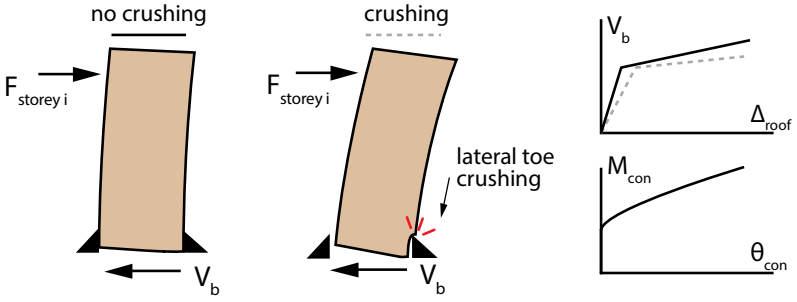

Figure 4.10: Lateral compression at the rocking toe shear key

Another possible explanation may be that the bending and/or shear stiffness of the experimental specimen was overestimated in the numerical model. Because Sarti combined smaller LVL panels to create the wall specimen, the possibility is introduced for the system to have reduced shear and bending stiffness parameters due to the shear transfer in the built-up section, without affecting the compression stiffness at the wall base. Therefore, a variation of the numerical model with a reduced wall bending stiffness was tested to investigate this proposal; the results are presented in Figure 4.11. In this numerical test, the bending stiffness of the controlled rocking wall was halved while the compression stiffness of the base was maintained. The result of this was an approximately 25% increase in elastic drift contribution at peak drift, resulting in a closer match with the elastic and connection moment contributions to roof drift observed in the experimental test data. An additional reduction in the shear stiffness (by 50%) also resulted in a minor elastic drift increase, although the effect is too small to show here. The system's apparent sensitivity to

these bending and shear stiffness terms suggests that the bending and compression stiffness of a CLT panel should be investigated further. Furthermore, this factor can have a significant effect on the dynamic properties of the wall panel, since the natural frequency of the wall would be reduced; this adds further significance to investigating the bending stiffness of these heavy timber panels.

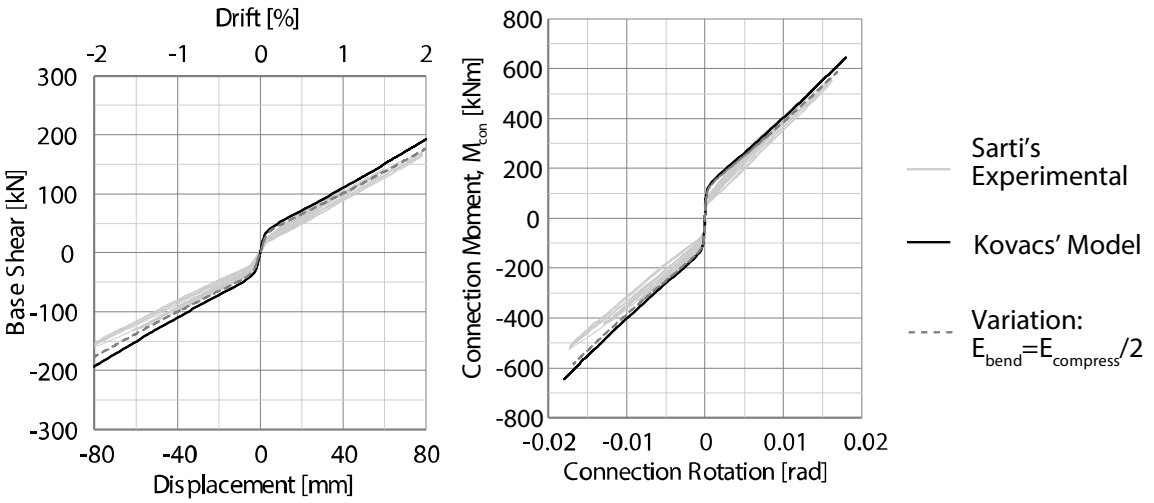

Figure 4.11: Wall response to reduced wall lateral stiffness, while maintaining the connection stiffness

Finally, the analysis process converged on a connection rotation value of 0.0165 radians at peak drift, whereas the numerical model experienced 0.0175 radians of connection rotation, as per Figure 4.5 and Table 4.2, suggesting a discrepancy between the analytical process and the numerical model representing Sarti's experimental test. The difference between the two models is related to the unique scale of Sarti's experimental setup. The analytical model assumes the PT is anchored at the base of the wall, although it accounts for the full-length of the PT in the strain calculation, as shown in Figure 4.12 (a). In contrast, the numerical model matches Sarti's experimental setup in which the PT is anchored one meter (25% of the wall height) into the foundation, as shown in Figure 4.12 (b); the length within the foundation is free to rotate as the wall rocks, as shown in Figure 4.13 (a). It will be shown in the pushover discussion for the prototype model of a full-scale design (Section 4.3.2) that this discrepancy does not exist in the context of a full-scale design, as shown in Figure 4.12 (c). Therefore, it is suggested that this scale factor leads to minor discrepancies (approximately 10%) between the analytical and

numerical model outputs. The implication of this suggestion is that the anchorage conditions of the PT within the foundation, and the depth of embedment in the foundation, may be significant factors in design and analysis. The geometry of the small-scale experimental setup is relatively simple to capture in the numerical model; however, the small-scale geometry and the rotational restraint condition of the PT length within the foundation, may not be applicable to a full-scale wall; for example, the PT embedded in the foundation may be restrained as shown in Figure 4.13 (b). Therefore, Sarti's PT conditions are not incorporated in the analytical model.

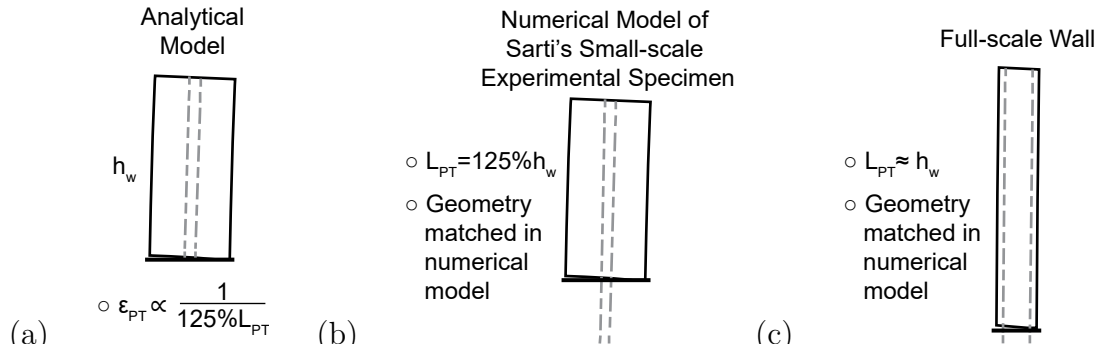

Figure 4.12: Analytical and numerical model scale discrepancies

Figure 4.13: PT anchorage conditions of concern for small-scale testing

Neutral Axis Depth

The analysis process and numerical model both converged on the same neutral axis depth, within 1% of each other, at peak roof drift. However, the experimental results demonstrate a larger neutral axis depth, by as much as 20%. This neutral axis depth discrepancy was identified by Newcombe (2015) as a consequence of the instrumentation of experimental specimens, and is to be expected in a comparison of experimental and numerical results. The particular issue that Newcombe identified was with the assumption of a linear base profile of the wall specimen, when in fact the base exhibits some curvature, especially at larger degrees of uplift, as depicted

in Figure 4.14. Researchers, including Sarti (2015), often assume a linear function to determine the neutral axis depth from their potentiometer readings, but in fact the most uplifted potentiometers (A and B in Figure 4.14) will cause that interpolation to overestimate the actual neutral axis depth. The effect is especially evident in the graph included in Figure 4.14, showing a plot of the wall base uplift deformation versus the linear approximation.

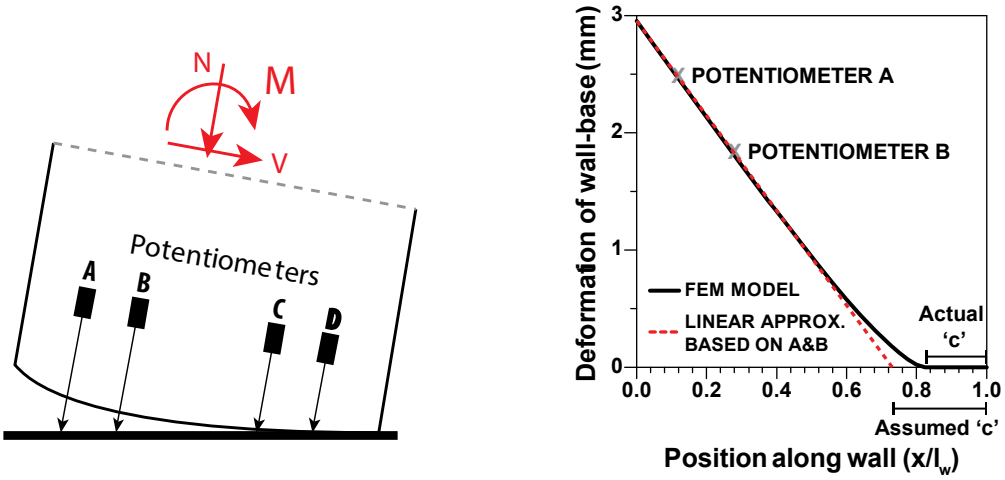

Figure 4.14: Experimental instrumentation leads to neutral axis overestimation

The wall base curvature is not captured in the numerical model, and interpolation is also relied upon to determine the neutral axis depth; however, the base connection is modelled with many more fibers (approximately one every ten millimeters), which act like the potentiometers in the experimental test. By observing the strain in these fibers in the compressed toe, the numerical model outputs a better resolution of the wall base compression forces.

4.2.2 Application of Model Validation Conclusions

The similarities and differences explored above help to determine which physical behaviours or attributes might have influenced the experimental test, and how these factors can be considered by the numerical model. This exploration concluded that the following physical behaviours could be significant:

1. Loss of PT force:
    a. Due to top-of-wall crushing under large PT stresses;
    b. Due to plastic PT strains

2. Lateral and vertical rocking toe compression / damage
    a. Due to lateral compression / translation against the shear key;
    b. Due to vertical crushing / plastic strains in rocking

3. Dissimilar bending and base compression stiffness terms

Items 1, 2 (b) and 3 were discussed independently in the numerical model in Section 4.2.1, while item 2(a) was discussed but not included in the model because of the complexity of doing so. It is expected that several of these physical behaviours occur simultaneously in the experimental model.

The significant physical factors presented above are now considered in the numerical model, acting together to affect the controlled rocking wall response. However, these modifications are not necessarily as substantial as those presented above, since partial combinations resulted in an acceptable lower bound to the observed behaviour. The modified system has a 30% bending stiffness reduction (to 7,700 MPa), and 36% shear stiffness reduction (to 350 MPa), motivated by the discussion in Section 4.2.1. A damaged rocking toe is modeled by assigning a 40% compression stiffness reduction to the base fibers within 200 mm of the rocking edges. Finally, the PT material modifications presented in Table 4.3 are applied to the wall to develop hysteretic behaviour reflective of some top-of-wall crushing beneath the PT anchorage; the initial PT force is also reduced by 25%. The combined modifications are summarized in Table 4.5.

Table 4.5: Lower-bound system modifications

Property	Modifier	Resulting System Properties
$E_{bending}$	-30%	7,700 MPa (elastic Timoshenko beams)
$E_{compress}$	100%	11,000 MPa except
(Base Connection)	-40%	6,600 MPa within 20 cm of rocking edges
$T_{PT,init}$	-25%	75 kN/PT element
G_{timber}	-36%	350 MPa
PT Material	OpenSees parameters modified to account for timber crushing under PT anchorage (see Table 4.3)	

The resulting system is tested according to the quasi-static displacement protocol defined by Sarti (see Figure 4.8), and the modified system response is compared with

Sarti's experimental data in Figure 4.15; the modified system represents a lower bound response to Sarti's experimental data. Recall that this lower bound model is expected to be a conservative estimate of the controlled rocking CLT response, given the design process presented in Chapter 3: as discussed in Section 4.2.1, many effects mimicked by the lower bound model are mitigated by the design process and recommended configuration for low-to-moderate seismic hazard regions.

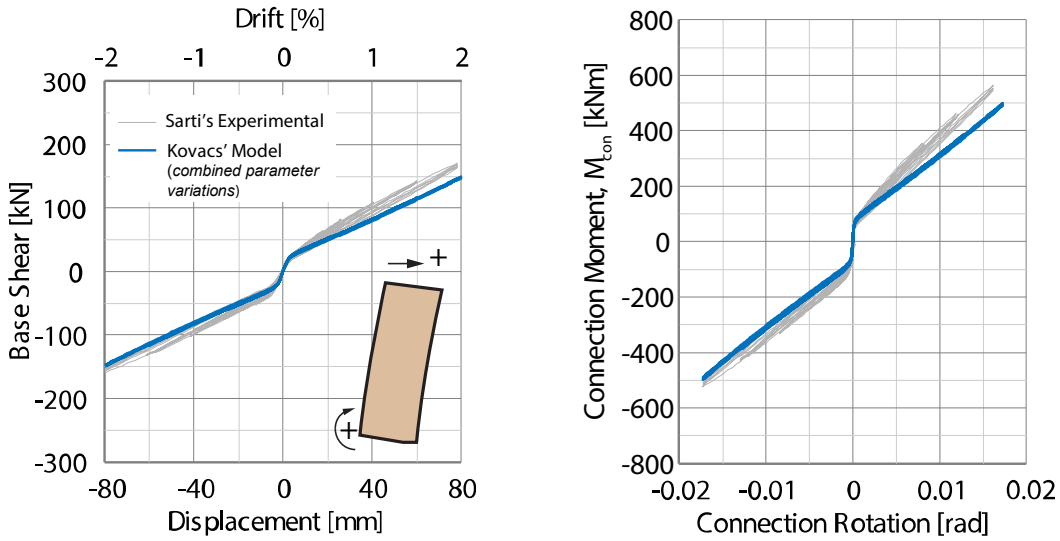

Figure 4.15: Combined system modifiers, compared to Sarti's experimental data

Overall, the numerical model presented in Section 4.1 is able to capture the important features of a controlled rocking heavy timber wall response, as per comparison in Section 4.2.1 with experimental results published by Sarti (2015). This confirms the ability of the WSA to represent a controlled rocking heavy timber wall using specified material property and wall configuration values, with a minimal degree of calibration to consider practical material and wall panel conditions. It is likely that any required calibration presented in Section 4.2.2 could be reduced or eliminated through material research and careful design decisions which reduce timber damage effects due to PT.

4.3 Verification of Prototype Numerical Model

CLT material properties and controlled rocking wall dimensions/configuration are applied to the numerical model outlined in Section 4.1, to reflect the Ottawa

prototype designed and analyzed in Chapter 3. The resulting numerical model was tested in a modal analysis, which confirmed the first mode period of 1.80 s used in the design process. Furthermore, a static pushover procedure is conducted and investigated herein, to compare with design and analysis results from Chapter 3. Recall that Chapter 3 concluded with a unidirectional pushover curve, including key responses from the design and analysis process.

4.3.1 Preparing the Numerical Model and Lateral Pushover Procedure

The prototype material properties and wall configuration are identified in the design phase of Chapter 3. In the prototype, PT is anchored at the base of the wall, rather than deep in the foundation as it was for the validation process in Section 4.2. As in Section 4.2.1, the numerical model's base connection stiffness is a function of the neutral axis depth (186 mm) at 2% roof drift; therefore, the Winkler spring length is 1454 mm, as per Equation 4.1. The base connection stiffness is assigned to the Winkler spring elements, and a lateral static pushover test is applied out to 2% (396 mm) roof drift. Note that this is less than the 2.5% roof drift allowance for normal importance buildings according to the Canadian building code (NRCC, 2010). 2% pushover is deemed acceptable since the expected peak drift, as per the design and analysis stage of Chapter 3, is only 0.83% (Chapter 3). The force distribution is proportional to that used in the design stages of Chapter 3, which was essentially an inverted triangular distribution.

4.3.2 Pushover Results

The results of the pushover process are presented in Figure 4.16, overlaid on the analytical pushover curves which were first presented at the end of Chapter 3. With respect to the system response parameters (base shear and connection moment), the two models match very well, with only a slight (less than 5%) overestimation of the rocking load, by the analytical model relative to the numerical model. This discrepancy is due to the analytical model's simplification of the base response at the rocking load: the rocking event was assumed to occur at a definite point in the wall's pushover response, when the neutral axis reached the second PT element. Practically, the system does not have a discrete point where it transitions from its

initial to post-uplift stiffness. However, this transition occurs quickly, so only a minor discrepancy is seen around the system yielding point.

Another significant similarity is the base connection rotation at a given base moment: both the analytical and numerical models have matching connection rotation terms throughout the uplifted response. This is in contrast to the analytical and numerical model of Sarti's experimental setup in Section 4.2. In that case, the analytical model did not capture the exact geometry of the numerical model or Sarti's experimental model, resulting in the discrepancy. In this case, the numerical model positions the base PT connection at the bottom of the wall, rather than deep in the foundation, resulting in matching system geometries. For a full-scale (mid-rise) controlled rocking wall design, this geometry may be more applicable, as long as the PT is not embedded within the foundation at a significant depth compared to the total height of the wall.

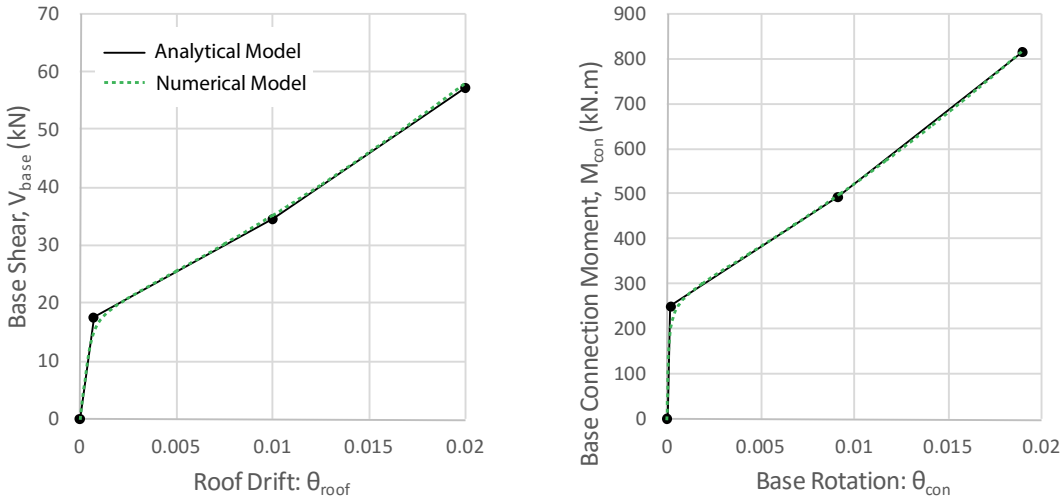

Figure 4.16: Comparing analytical and numerical model pushover results for Ottawa prototype

One final interesting behaviour noted in these pushover plots is the upward concavity (second-order stiffening) of the response parameters in the uplifted range of response. This second-order stiffening is due to the increasing lateral contribution to the wall response, by the PT element, as the wall rotates.

4.4 Inherent Controlled Rocking System Damping

The final numerical model development step is the incorporation of inherent damping. Inherent damping is important to the following chapter (Chapter 5), because it relates to the numerical model response under dynamic motions. Some background to controlled rocking system damping is presented below, and the final numerical model implementation is provided thereafter.

4.4.1 Inherent Damping Background

Based on previous controlled rocking heavy timber research, there are two main controlled rocking damping contributions to consider: Rayleigh damping of the superstructure, and impact damping of the rocking joint (Marriott, 2009; Sarti, 2015).

Rayleigh Damping

The Rayleigh damping model is commonly used in non-linear time-history analyses (Chopra & McKenna, 2015). This model incorporates a damping matrix (expressed as in Equation 4.2) in the numerical model's system of equations; its implementation typically involves determining eigenvalues for at least two modes of the system, and specifying damping ratios for each mode, as per Equation 4.3. Chopra (2007) suggests that selecting the same ζ for both modes is reasonable, based on experimental data, meaning Equation 4.3 can be solved and simplified for a_0 and a_1 as per Equations 4.4 and 4.5.

$$\boldsymbol{c} = a_0\boldsymbol{m} + a_1\boldsymbol{k} \qquad \textbf{Equation 4.2}$$

Where $\mathbf{m}$ and $\mathbf{k}$ are the system mass and stiffness matrices, respectively

$$\frac{1}{2}\begin{bmatrix} 1/\omega_i & \omega_i \\ 1/\omega_j & \omega_j \end{bmatrix}\begin{Bmatrix} a_0 \\ a_1 \end{Bmatrix} = \begin{Bmatrix} \zeta_i \\ \zeta_j \end{Bmatrix} \qquad \textbf{Equation 4.3}$$

Solution for a_0 and a_1:

$$a_0 = \zeta\frac{2\omega_i\omega_j}{\omega_i + \omega_j} \quad \text{and} \quad a_1 = \zeta\frac{2}{\omega_i + \omega_j} \qquad \textbf{Equations 4.4 and 4.5}$$

Rayleigh damping has several variations, including initial stiffness-proportional and tangent stiffness proportional damping, referring to the stiffness matrix in Equation 4.2. Stiffness-proportional damping can induce large damping forces,

especially when a numerical model begins yielding (Charney, 2008; Chopra et al., 2015); this is a significant concern in the controlled rocking system response. Alternatively, the tangent stiffness proportional stiffness damping model is recommended as a solution (Chopra et al., 2015). Although tangent stiffness damping has several criticisms of its own, as per Chopra & McKenna (2015), the tangent stiffness model results in improved responses and presents a conservative response.

Impact Damping

Impact damping was explored in-depth by Marriott (2009), but is generally ignored when supplemental energy dissipation elements are provided in a system because hysteretic damping will overcome impact damping to govern the response. However, Marriott concluded that lightly damped controlled rocking wall systems can be sensitive to the small impact damping contribution. Marriott considered both rigid (precast concrete) and heavy timber walls in his research. In a controlled rocking heavy timber wall without supplemental energy dissipation, Marriott's conclusion is especially relevant, and presents an opportunity for further research regarding impact damping.

4.4.2 Damping Implementation

Given the discussion regarding Rayleigh and impact damping in Section 4.4.1, only tangent-stiffness proportional Rayleigh damping is applied to the numerical model. If impact damping is in fact a significant factor in the controlled rocking heavy timber response, then this decision results in a conservative numerical model response, and future research regarding the impact damping mechanism will result in reduced system responses.

To implement Rayleigh damping in the numerical model, critical damping of 5% (ζ=5%) is assumed and applied to the first and third modes. This resulted in the coefficients for Equation 4.2, which were applied to the Rayleigh damping term in OpenSees. At each step of the numerical model response analysis, the system stiffness matrix and the two coefficients are re-determined and applied to the Rayleigh damping term. Discussion on the effect of the damping term, and sensitivity of the model's response to damping, are included in Chapter 5.

5 Numerical Model Analysis

This chapter presents the results of non-linear time history analysis (NLTHA) of the prototype controlled rocking CLT wall that is outlined in the previous chapters. First, the selection and scaling of a ground motion suite to the uniform hazard spectrum for Ottawa, Ontario is presented, including twelve ground motions. Next, the model is investigated for sensitivity to various parameters using a subset of the ground motion suite. Finally, the full scaled ground motion suite is used in the NLTHA of the prototype model and its lower-bound variation (presented in Section 4.3): the model's overall performance is evaluated and the behaviour of the Winkler springs and PT elements are investigated individually.

5.1 NLTHA Introduction & Preparation

The NLTHA procedure applies acceleration time-histories to the numerical model, simulating earthquake ground motions on the structure, in order to investigate the response to a seismic hazard represented by the time-history (ground motion) record. In the analysis procedure, the model's element and material properties capture dynamic and non-linear behaviour, including P-Delta effects, damping, and non-linear material responses; capturing these effects in a NLTHA is computationally demanding, but it allows engineers to investigate both the system and element behaviour in a building subjected to dynamic loading. However, given the complexity of the model and material properties being studied, it is important to ensure that the time history records input to the model are reflective of the seismic hazard for the region of interest, so that the conclusions drawn from the modeling response are relevant to the regional hazard. Furthermore, it is important to understand the model's sensitivity to several analysis parameters, to be confident in the conclusions drawn from a full investigation. For this reason, ground motion selection and scaling is presented first, followed by an investigation of several analysis parameters, before investigating the model's response to the full ground motion suite.

5.1.1 Ground Motion Selection and Scaling

The following NLTHA reflects Canadian seismic hazards by scaling a suite of acceleration time-history records to the NBCC response spectrum for Ottawa, representing a 2% chance of exceedance in fifty years (NRCC, 2010). The time-history records selected for the NLTHA are synthetic motions, developed by Atkinson (2009), representing Eastern Canadian seismic hazards. The synthetic motions were developed due to a lack of high quality records of historical seismic events in Eastern Canada, especially considering the variety of site conditions associated with the region's ground motions (i.e. near and far sources, different event magnitudes, and different soil conditions). By considering Eastern Canadian seismic sources and site conditions, Atkinson (2009) reproduced waveforms in the synthetic motions to reflect expected natural seismic events in the region.

For the NLTHA analysis presented in this chapter, both magnitude six and seven events from near and far sources are considered at a site with soil Class C (as per the prototype building design). The event names are referred to in the following discussion and figures as follows: "M#$_m$.near_Rec#$_R$" and "M#$_m$.far_Rec#$_R$" where #$_m$ is the magnitude, "near" or "far" refers the to source distance and #$_R$ is the record number, from Atkinson's records. For example, M6.near_Rec01 refers to a near-source record of magnitude six, labelled record "01" in Atkinson's record set.

Selection and scaling of the ground motions relies on a method outlined by Atkinson et al. (2015). First, twelve records are selected from the record sets outlined by Atkinson (2009), including three each from both near and far M6 and M7 events. Next, acceleration and displacement response spectra are plotted for the records, including the mean spectra for each of the four record sets (sets identified by magnitude and distance), and the NBCC design spectrum. The individual record spectra are defined as $S_g(T)$, whereas the NBCC design (target) spectrum is defined as $S_T(T)$. From the unscaled records, two period ranges of interest are identifiable from the dominance of the mean spectra: M7 near and far record sets dominate in the long period range (beyond one second) while the M6 near and far record sets dominate below this period range; this characterization of seismic hazard is consistent

with the discussion in Atkinson (2009) regarding Eastern Canadian seismic hazard. Given this characterization, M6 events are selected for scaling over a range of $0.2T_1$ to T_1, and M7 events are scaled over a range of T_1 to $2.0T_1$, where T_1 (1.80 s) is the natural period of the structure. Over these scaling ranges, a scaling multiplier (S_M) is calculated for each record, as per Equation 5.1 (Dehghani & Tremblay, 2016). The individual spectra are scaled by S_M, resulting in new mean spectra for the four record sets. These new mean spectra cannot be more than 10% below the target spectrum over the range of interest (Atkinson et al., 2015), so the differences between the new mean spectra and the target spectrum are calculated and a second scaling multiplier ($S_{M2,mean}$) is determined for those sets where the mean spectrum is more than 10% below the target spectrum; $S_{M2,mean}$ is determined at the period where the maximum difference (max Δ) is calculated, as per Equation 5.2. The scaling multipliers for each record set are summarized in Table 5.1, and the scaled acceleration and displacement response spectra are included in Figure 5.1 (a) and (b), respectively. Note that the scaled spectra are significantly larger than the design spectrum in the short period range due to the natural period of interest and the scaling range.

$$S_M = \sum_{i=\substack{lower\\bound}}^{\substack{upper\\bound}} \left(\frac{S_T(T_i)}{S_g(T_i)} \right) / n_i \qquad \textbf{Equation 5.1}$$

$$S_{M2,mean} = \left[\frac{90\% \cdot S_T(T_i)}{S_g(T_i)} \right]_{max\ \Delta} \qquad \textbf{Equation 5.2}$$

Where n_i =number of spectra values over the range, and
$S_{M2,mean}$is calculated where the difference between the mean and target spectra exceeds -10%

Table 5.1: Scaling multipliers for each ground motion set

	M6.near			M6.far			M7.near			M7.far		
Record Number:	**1**	**4**	**7**	**4**	**10**	**22**	**16**	**37**	**40**	**7**	**13**	**19**
Initial Scaling (S_M)	0.601	0.775	0.631	3.12	1.59	3.48	0.793	0.731	0.824	1.50	3.22	2.64
$S_{M2,mean}$	x 1.39			x 1.23			x 1.02			x 1.06		
Resultant Multiplier	0.832	1.07	0.877	3.84	1.96	4.28	0.809	0.746	0.841	1.59	3.41	2.80

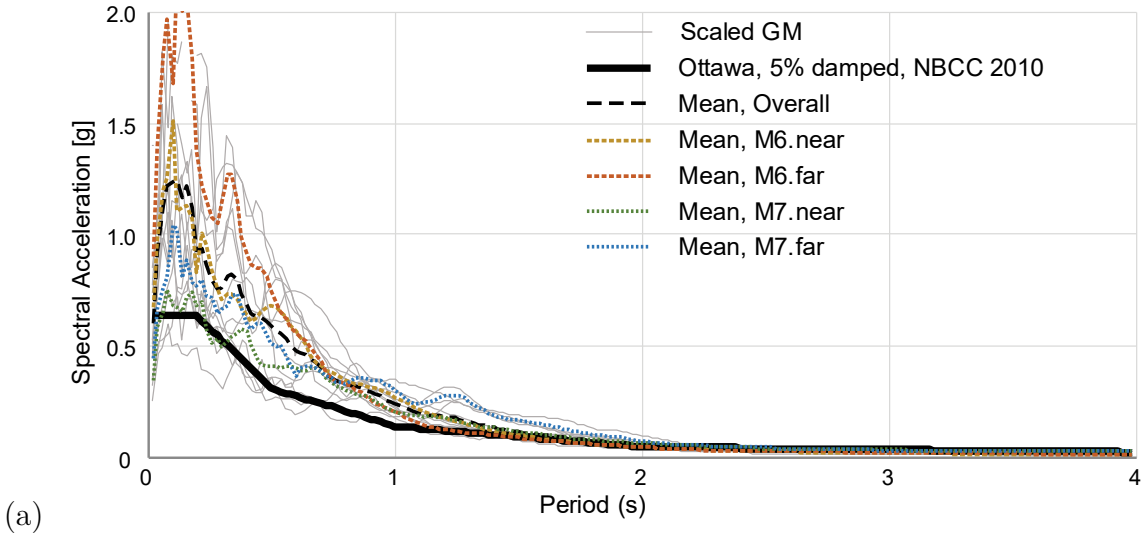

(a)

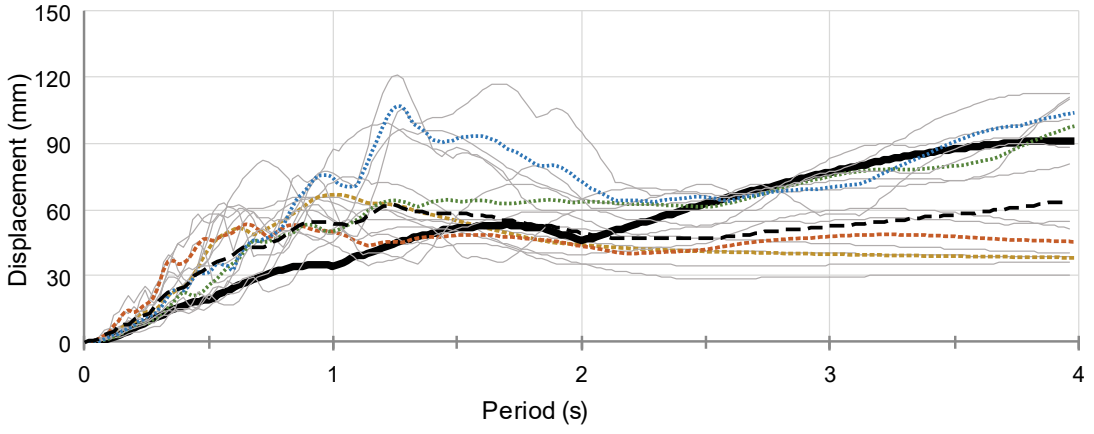

(b)

Figure 5.1: Scaled (a) acceleration and (b) displacement response spectra

5.2 Analysis Parameter Sensitivity

Four of the twelve scaled ground motions, including one each from M6 and M7, near and far events, are used to investigate the numerical model's sensitivity to several analysis parameter settings. First, the analysis time step is studied to ensure that the system behaviour is accurately captured. Next, the number of Winkler Springs in the base connection is investigated to understand the model's sensitivity to the discretization of the base connection interface. Finally, the model's sensitivity to the damping ratio is investigated to evaluate the variability in the system's response due to this assumed modeling parameter.

Analysis Time Step

Figure 5.2 and Figure 5.3 show the peak roof drift and floor acceleration responses, respectively, recorded in the four scaled ground motions, considering seven analysis time step parameters ranging from 0.01 s to 0.0001 s. The results show a consistent peak roof drift and peak floor acceleration response for the time steps between 0.0001 s and 0.002 s. For larger time steps, the peak responses diverge. In controlled rocking systems, convergence of the peak accelerations often requires the shortest time step (L. Wiebe, 2009); and at smaller time steps, the analysis takes proportionally longer, and produces more data (e.g. halving the time step doubles the analysis time and output data). Therefore, a 0.002 s time step is used for the NLTHA in Section 5.3.

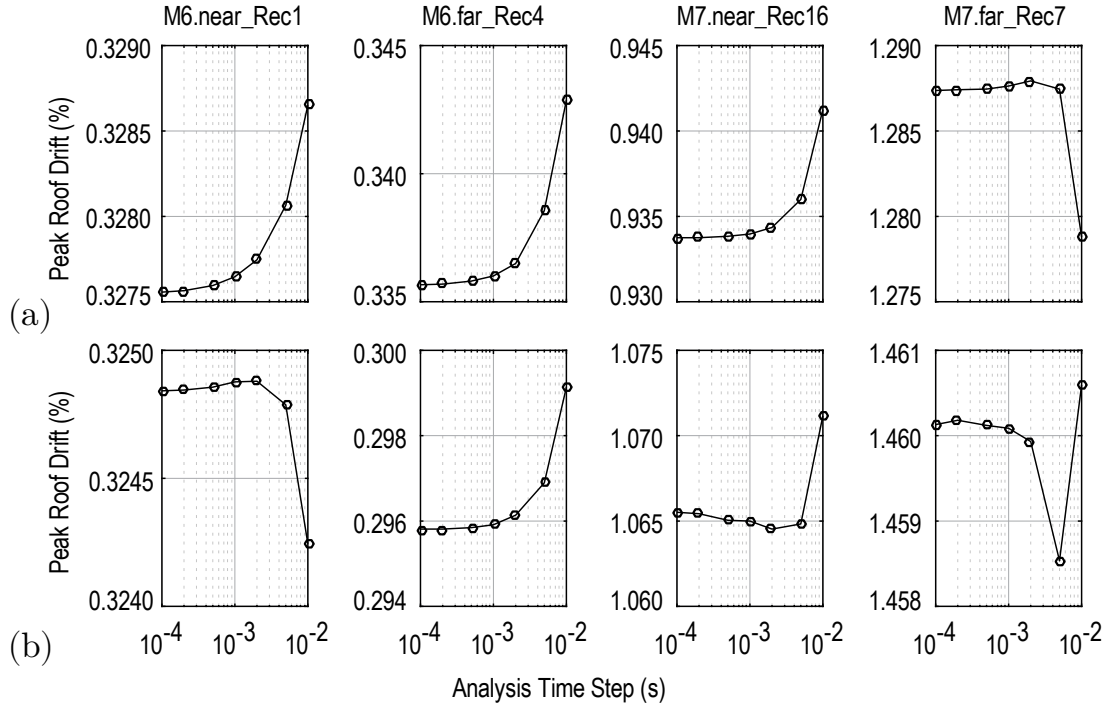

Figure 5.2: Analysis time step sensitivity to peak roof displacement in (a) baseline, and (b) lower-bound model

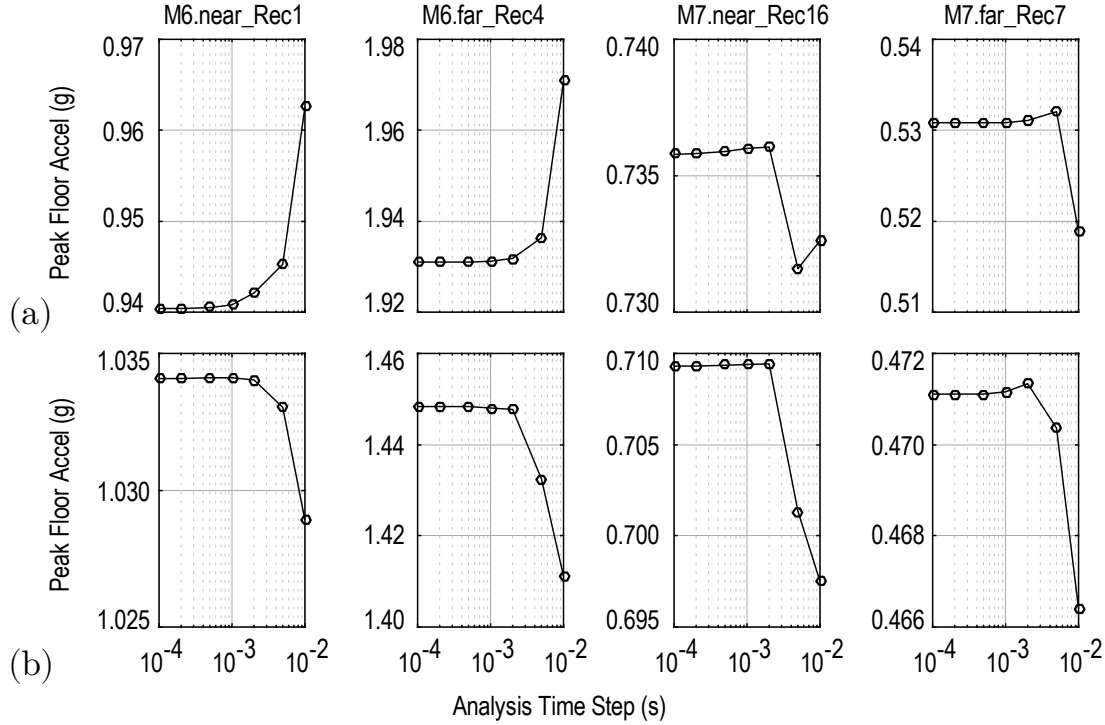

Figure 5.3: Analysis time step sensitivity to peak floor acceleration in (a) baseline, and (b) lower-bound model

Number of Winkler Springs

The number of Winkler springs was varied in a sensitivity investigation related to the base connection model. The results are presented in terms of the percentage of the wall that is represented by a single Winkler spring. The prototype model was tested considering ratios of 0.54% (186 springs over 2440 mm) to 6.25% (sixteen springs over 2440 mm). The analysis times were almost directly proportional to the number of springs: the longest analysis required fifteen minutes, whereas the shortest analysis required just 80 seconds.

Roof drift time history results are presented in Figure 5.4, demonstrating the similarity in the roof drift response for the baseline and lower-bound models. The peak roof drift in every case is within 1% of the largest response; the largest response occurs in the model with the largest number of springs. The only significant variation seen in this data is after several cycles of rocking, in which the roof drift is slightly out of phase in the case with the fewest springs; however, the response from the higher resolution of springs clearly converges, as seen by the overlap of the time-history records. For the analyses, an intermediate quantity of 122 springs was used, such that each spring represents 0.82% of the wall length. Although these results suggest a lower number of springs could be used, 122 springs are used in the NLTHA presented in Section 5.3, as a compromise between computation time and the resolution of recorded information at the base connection.

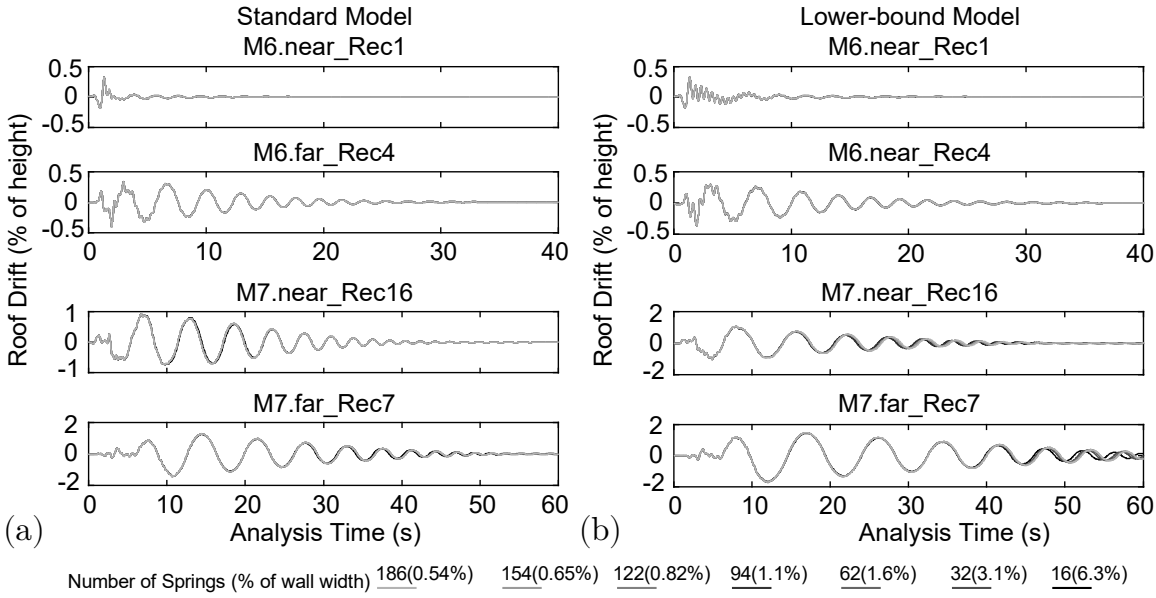

Figure 5.4: (a) Baseline model, and (b) lower-bound model time-history records investigating roof drift sensitivity to quantity of Winkler springs in the base connection

Damping Ratio

As per the damping discussion in Chapter 4, the damping applied to the numerical model is a tangential stiffness Rayleigh damping model, with a critical damping ratio (ζ) of 5% applied in the first and third modes. However, the value of ζ is only an assumption, and further research is needed to understand the inherent damping in a controlled rocking CLT wall. Because of the uncertainty in this parameter, the sensitivity of different response parameters in the numerical model must be investigated. For this investigation, the four scaled ground motions were considered on the baseline and lower-bound models with varying ζ values. The results are normalized to the 5%-damped case, and the peak interstorey drift, floor acceleration, storey shear, and bending moments are compared in Figure 5.5 and Figure 5.6, for the baseline and lower-bound models respectively.

In Figure 5.5, the largest responses of the baseline model (relative to the 5% damped case) are from the lowest damping response of 2%. The largest difference is a 50% larger storey shear response when the damping is only 2%. Otherwise, the other response parameters are equal to or less than 30% larger than the 5% damped case. In Figure 5.6, the largest responses of the lower-bound model (relative to the

5% damped case) are from the lowest damping response of 2%. The largest difference is a 50% larger storey shear response when the damping is only 2%; however, there are several other response parameters that are equal to or less than 45% larger than the 5% damped case.

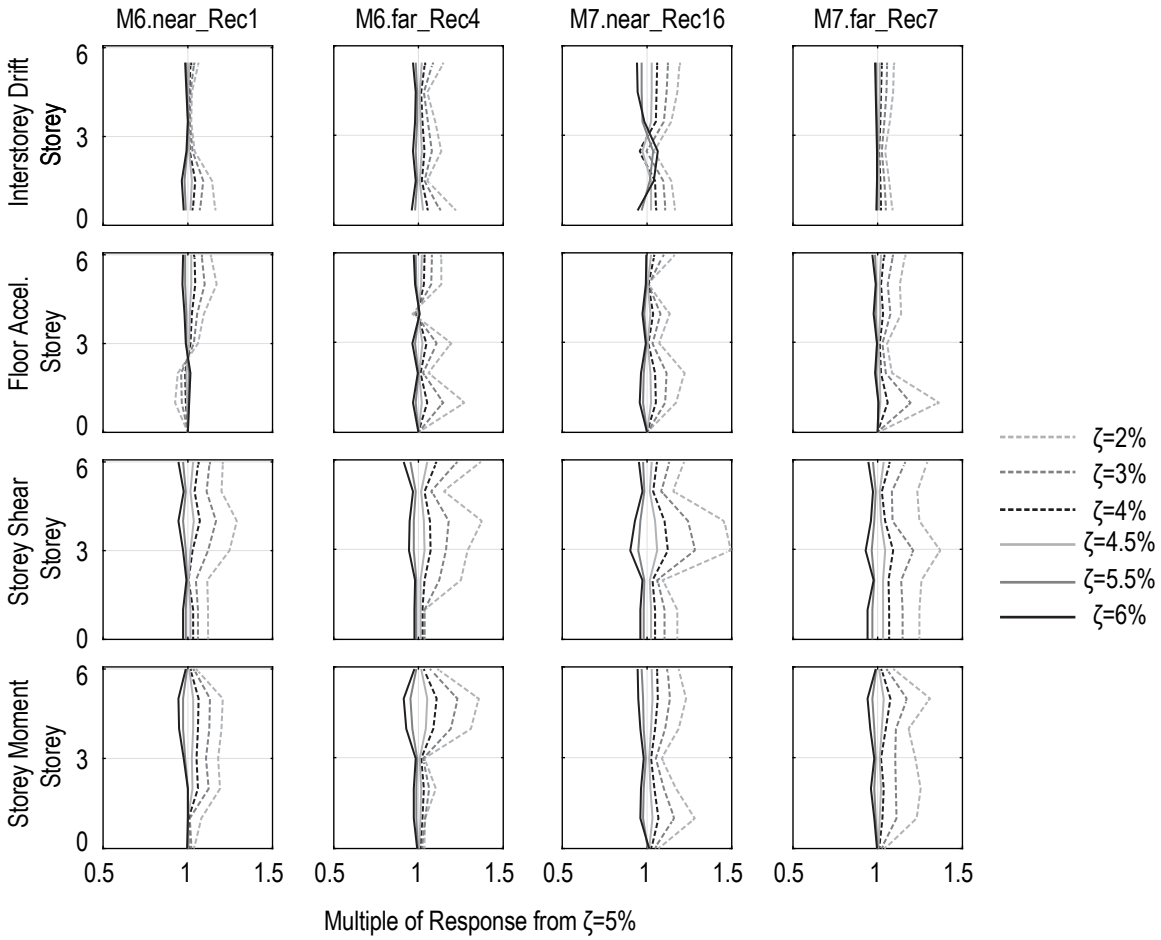

Figure 5.5: Sensitivity of response parameters in the baseline model, to the critical damping ratio

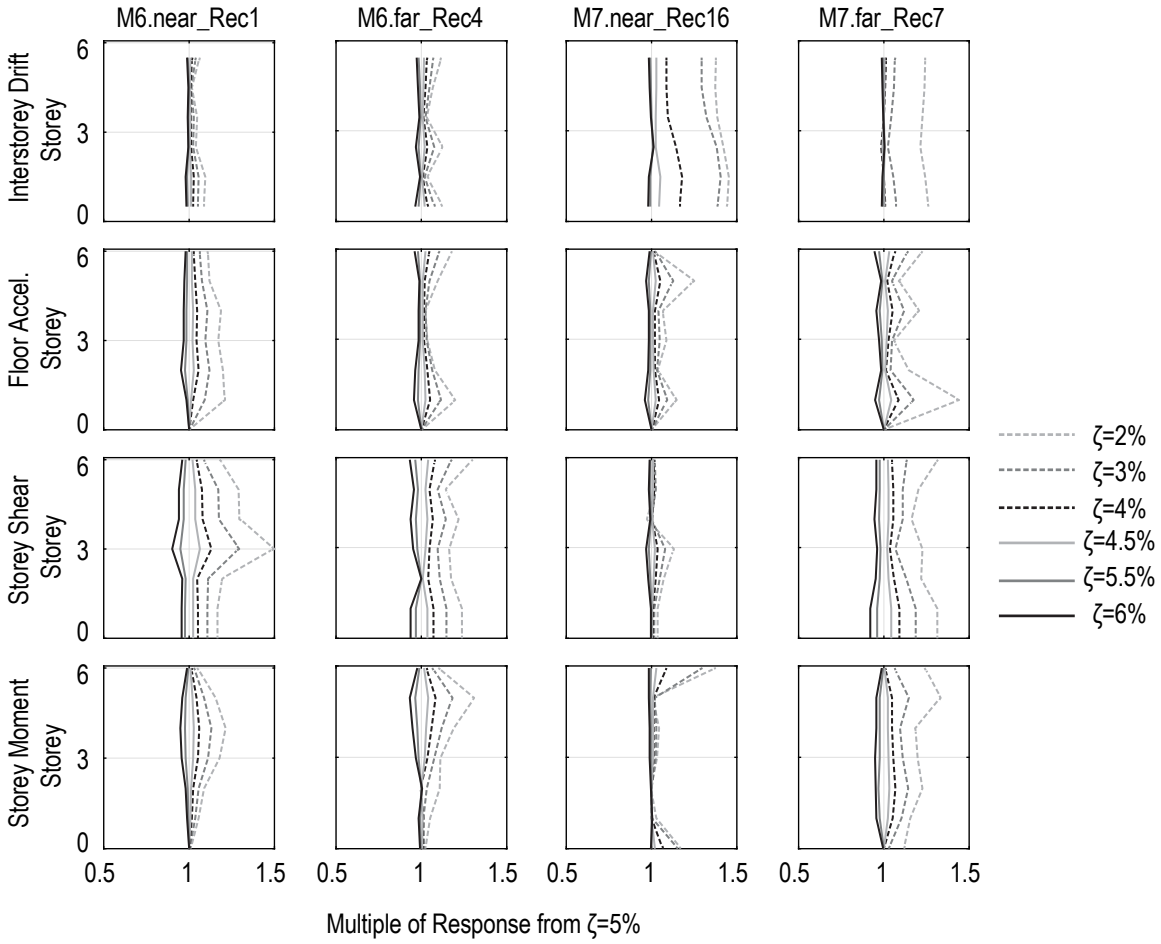

Figure 5.6: Sensitivity of response parameters in the lower-bound model, to the critical damping ratio

5.3 NLTHA Results

The following sections investigate the response of the prototype six-storey controlled rocking heavy timber wall subjected to the moderate seismic hazard of Ottawa, Ontario. System response parameters include storey drift, interstorey drift, shear force and bending moments over the height of the wall, and storey accelerations, to investigate the general performance of the system. Other response parameters include the hysteresis of the Winkler springs at the rocking toes, and the post-tensioning element hysteresis, to investigate the performance of these individual components of the system.

5.3.1 Storey Displacements

Figure 5.7 shows the peak storey displacements from the full suite of ground motions for the baseline model, overlapped with those for the lower-bound model. Both the baseline and lower-bound responses from the individual records are similar, as shown by the similarly-shaped dotted lines near the baseline model responses. The plots also include the mean response from the ground motion suite, and the non-linear displacement estimate determined from the design process (Chapter 3). The results show that the mean baseline and lower-bound responses match closely; however, the non-linear displacement estimate of 0.83% overestimates the mean roof drift (0.65%) from both models. This overestimation is likely because the design equation from Zhang (2015) was conservative for the case when β=0. Furthermore, the design equations from Zhang (2015) were calibrated using relatively low-frequency ground motions from California, as opposed to Eastern North American ground motions with relatively less low-frequency content. This theory is supported by the comparing the responses from the Eastern Canada M6 and M7 events in Figure 5.7: M6 events, with less low-frequency content (see Figure 5.1) did not have as large displacements compared to the relatively low-frequency M7 events. However, the system response to the M6 events demonstrates a larger degree of non-linearity above the mid-height. This non-linearity in the displacement profile suggests that the higher mode response of the system is more significant for these records, as investigated further in subsequent sections.

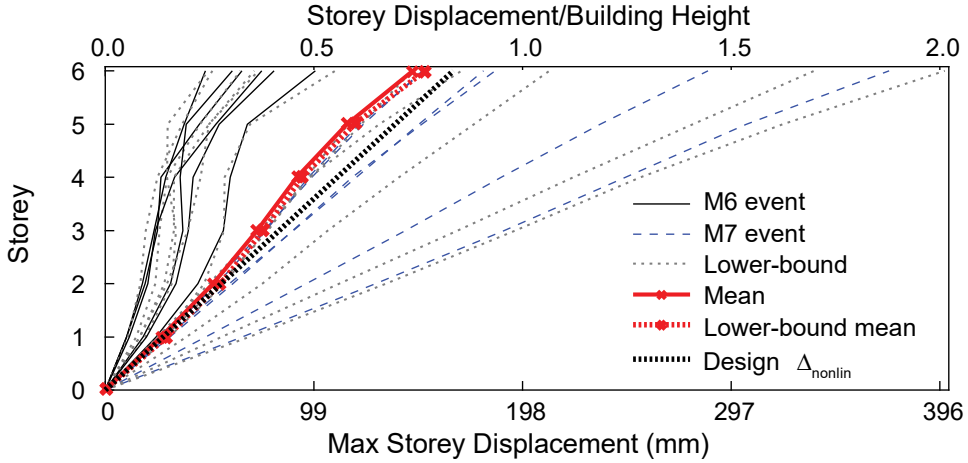

Figure 5.7: Peak storey drifts for the baseline and lower-bound prototypes

5.3.2 Interstorey Drift

Figure 5.8 shows the peak interstorey drift responses from the full ground motion suite, including the mean responses for the baseline and lower-bound models. Considering the baseline model responses, the non-uniformity of the interstorey drifts over the wall height for each ground motion record provides further evidence of the system's higher-mode response. Non-uniformity is especially evident in the M6 events, whereas the M7 events are more uniform but exhibit larger interstorey drifts. This observation is consistent with the discussion presented previously: the high-frequency content of the M6 events excites the higher modes, while the M7 events dominate in the long-period range that drives the displacement response.

The lower-bound model is presented as a comparison to the baseline model in Figure 5.8. Whereas the baseline model exhibited non-linearity (higher-mode response) in only a subset of the ground motion records, the lower-bound model exhibits more non-linearity in the majority of the records. The difference is likely associated with the 30% and 36% reduction in the wall's bending and shear stiffness parameters, respectively, since these parameters are directly associated with the dynamic behaviour of the system; the softened rocking toe and the reduced initial post-tensioning force, as per Table 4.5, likely also contributed to the differences between the two responses.

Both the baseline and lower-bound models exhibited a relatively low mean peak interstorey drift response, with a maximum of 1.1% in the lower-bound model, compared to the NBCC limit of 2.5% for normal importance buildings (NRCC, 2010).

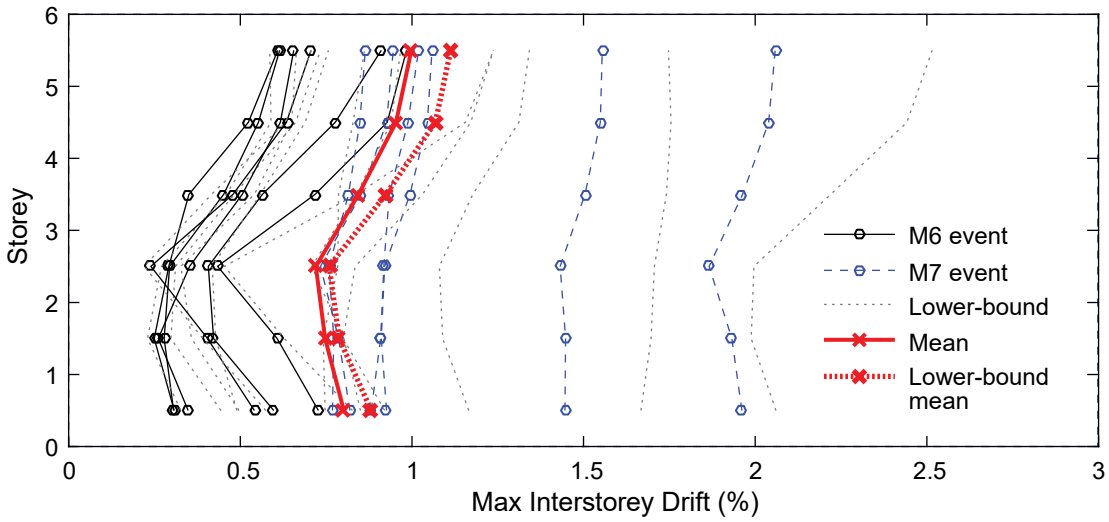

Figure 5.8: Peak interstorey drifts for the baseline and lower-bound prototypes

5.3.3 Storey Forces: Shear Force and Bending Moment

Peak storey forces are shown in Figure 5.9, separated into baseline and lower-bound model results in (a) and (b), respectively. Figure 5.9 (a) also includes the results of the higher mode estimation procedures presented in Chapter 3. Figure 5.9 (b) separates the M6 and M7 events to investigate the influence of frequency content on higher mode responses.

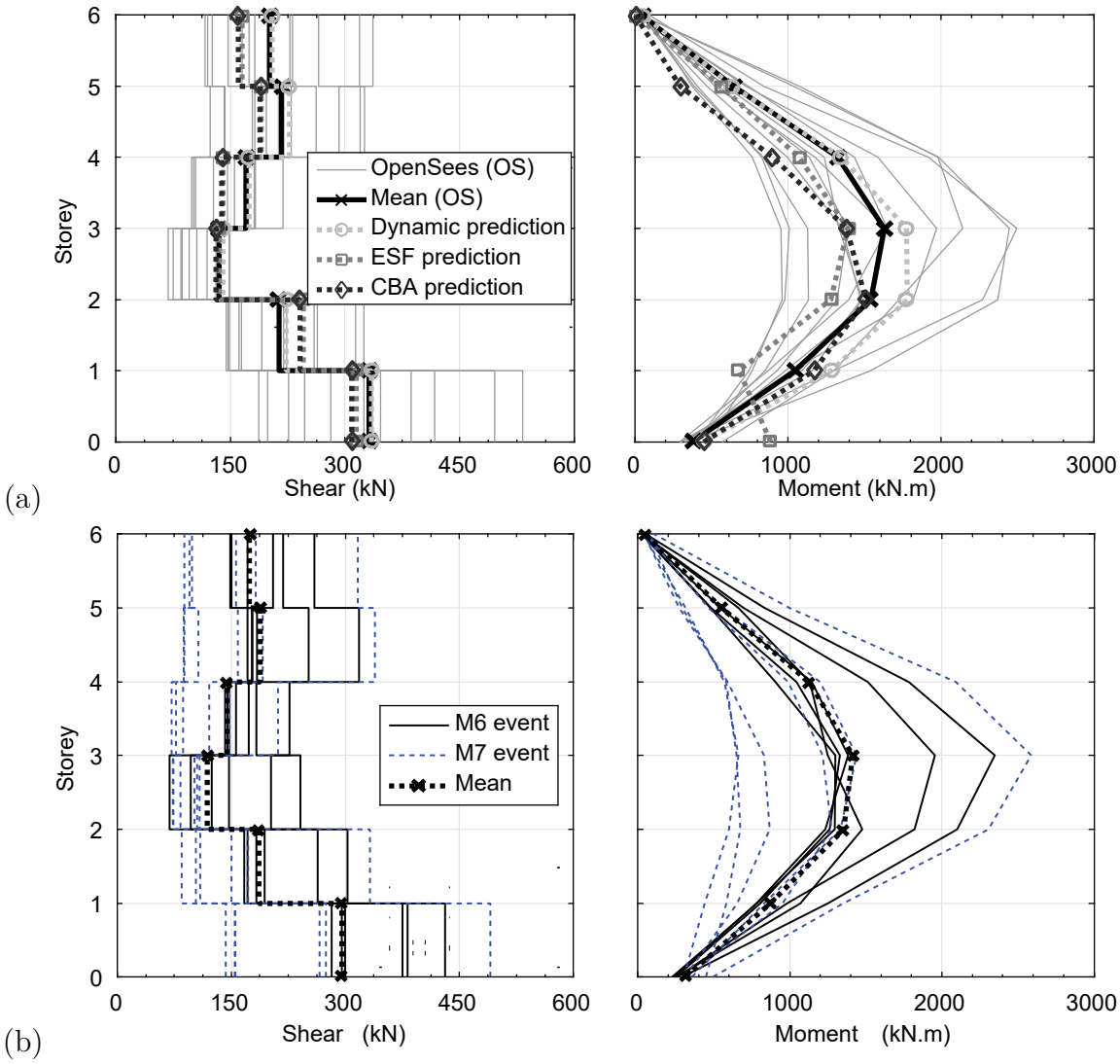

Figure 5.9: Peak storey forces for (a) baseline model, including higher mode estimates from Chapter 3, and (b) lower-bound model

Figure 5.9 (a) shows the peak forces over the height of the wall, which indicate higher mode vibrations in the controlled rocking heavy timber wall. One indication of the higher mode effects is that the mean base connection shear force (330 kN) is much larger than that determined by the equivalent static force procedure (18 kN) for the base connection design (Section 3.2). Nonetheless, the peak shear force was effectively captured, both at the base and over the wall height, by the dynamic and equivalent static force (ESF) procedures, and the cantilever beam analogy (CBA)

presented in Section 3.4. These higher mode estimation procedures estimated peak base shear demands of 335 kN, 315 kN, and 310 kN respectively.

Another example of the higher mode response in the OpenSees NLTHA results is the bending moment demand: a maximum bending moment of 1,630 kN·m was observed at the mid-height (third storey) of the wall. This demand is more than four times that at the base, but was also captured by the dynamic, ESF, and CBA procedures which estimated third-storey bending moment demands of 1,780 kN·m, 1,390 kN and 1,390 kN·m, respectively; this represents an overestimate of 10% in the dynamic procedure and an underestimate of 7% in the ESF and CBA procedures. Notably, a higher peak demand of 1,510 kN is estimated by the CBA at the second storey; this is 2% lower than the NLTHA results.

The significant mid-height peak bending moment demand is in contrast with the findings from Newcombe (2011) and Sarti (2015), where only a minor increase in bending moment demand was observed above the base connection, prompting the suggestion that the design base connection moment could be used to check the strength capacity (Newcombe, 2011). However, Newcombe and Sarti were evaluating the performance of controlled rocking LVL walls designed for high seismic hazards of New Zealand, rather than controlled rocking CLT walls for the moderate seismic hazard demand of Eastern Canada. The difference, as seen in the results presented here, is a lower base design force, and relatively more high-frequency content, increasing higher mode effects.

Finally, the mean base connection moment in the baseline model is 375 kN·m, whereas the design base connection moment was 250 kN·m. The mean observed roof drift of 0.65% from the NLTHA corresponds with an overstrength factor (Ω) of 1.60 (see Section 3.4.1 for the Ω calculation). If Ω is 1.60, the expected base connection moment is 400 kN·m, which is only 7% larger than the mean base connection moment. However, the dynamic and CBA higher mode estimation procedures both estimated a base connection moment of 450 kN·m, overestimating the mean peak demand by 20%. These estimation procedures are related to Ω calculated from the estimated peak non-linear roof displacement (Ω=1.80, as shown in Section 3.4.1),

and therefore the overestimate in the base connection moment is due to the overestimate of the peak non-linear roof displacement, discussed in Section 5.3.1. If Ω is recalculated for the NLTHA observation of 0.65% roof drift (i.e. if Ω=1.60), then both the dynamic and CBA procedures result in base connection moment estimates of 400 kN·m. The ESF estimate, however, is significantly different: the peak base connection moment estimate by the ESF procedure is 890 kN·m. This overestimate is explained by the discretized forces presented by Steele & Wiebe (2016) in Section 3.4.2. The base connection moment estimated by the ESF procedure should therefore not be considered in this case.

Considering the OpenSees NLTHA results for the lower-bound model in Figure 5.9 (b): the peak storey force envelopes are similar to those from the baseline model, except that the mean peak shear and bending moment demands are generally slightly lower than those in the baseline model. For example, the mean peak base shear is 295 kN, 10% lower than the baseline model. Furthermore, the mean base connection and mid-height bending moments are 313 kN·m and 1,410 kN·m, respectively, which are 17% and 13% lower than the respective forces in the baseline model. Comparing the structural responses in the M6 and M7 events also reinforces earlier findings regarding ground motion frequency content: high-frequency content of the M6 events is a significant driver of higher mode demands, as per the generally larger strength demands by the M6 records.

5.3.4 Storey Accelerations

Storey accelerations are considered due to their significance with respect to acceleration-sensitive elements, such as non-structural components. Figure 5.10 shows the peak storey accelerations of the baseline and lower-bound models, with the responses due to M6 and M7 events identified. A maximum allowable storey acceleration of 1.80 g is also indicated on the plot, based on non-structural component research by Rahman & Sritharan (2007, 2015) in controlled rocking precast concrete structures: 1.80 g represents a floor acceleration limit for a maximum considered earthquake (equivalent to 2% chance of exceedance in 50 years, as per the design in this thesis). In Figure 5.10, the mean peak storey acceleration

occurs at the roof level, and is similar in both the baseline and lower-bound models. The acceleration is 0.85 g in the baseline model and 0.83 g in the lower-bound model; these accelerations are less than half the 1.8 g limit. The largest acceleration envelopes were recorded in the M6 events, driven by the higher frequency content of these ground motions; this is consistent with the discussion in the previous sections.

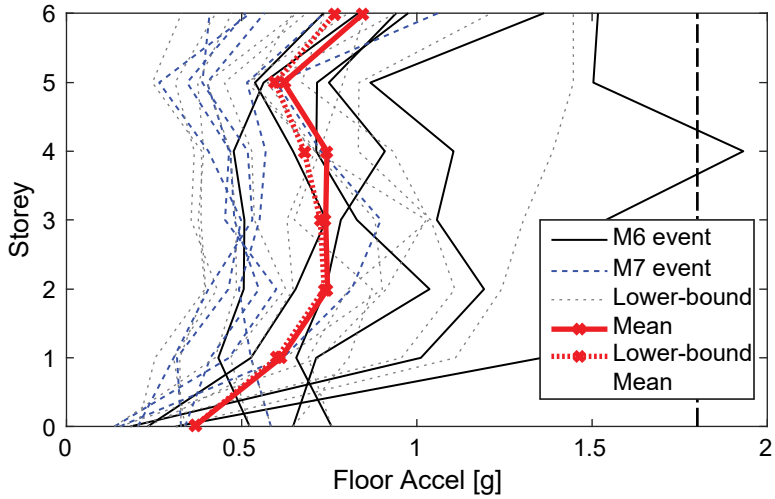

Figure 5.10: Peak storey accelerations

5.3.5 Rocking Toe Hysteresis

To investigate the performance of the base connection model, four rocking toe hysteresis records are shown in Figure 5.11, for the left and right outermost Winkler springs in the baseline wall model. The ground motions represented in this figure include one each from the M6 and M7, near and far ground motion suites. The records show the elastic behaviour of the Winkler springs in the rocking toe for the ground motions where the outermost fiber did not reach the yield stress (13 MPa), and elastic-perfectly plastic behaviour of the springs for the ground motions where the outermost fiber yielded (at 0.165% strain).

Figure 5.12 shows the hystereses for the left and right outermost Winkler springs in the lower-bound models, in which the Winkler springs' modulus of elasticity was reduced by 40% within 200 mm of the rocking edges of the wall. Due to the decreased modulus of elasticity, the initial stiffness in these hystereses is lower than in the baseline model; otherwise, the rocking toes yield at the same yield strength. However,

the reduced initial stiffness results in a larger yield strain; therefore, the yielding behaviour observed in the baseline model is not observed in the lower-bound case.

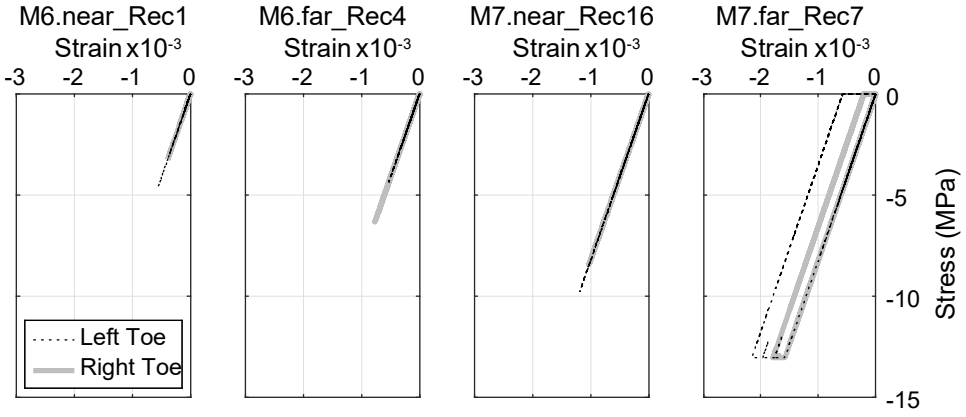

Figure 5.11: Outermost (left and right) rocking toe fiber hysteresis for baseline model

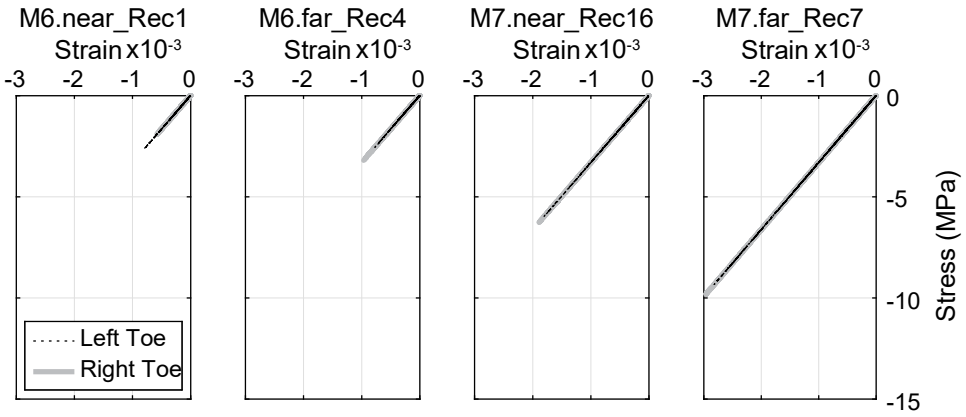

Figure 5.12: Outermost (left and right) rocking toe fiber hysteresis for lower-bound model

5.3.6 Post-tensioning Hysteresis

Figure 5.13 shows the post-tensioning (PT) hysteresis for the same four ground motion records presented in the rocking toe investigation. All four records show the PT hysteresis is within the elastic range, since the yield force is specified as 830 MPa. In comparison, the largest PT demand is 400 MPa. Furthermore, the largest PT demands occur in the M7 events, in which the relatively low-frequency ground motion content drives the displacement demand (i.e. rigid body rocking) of the system; recall from the analysis process that rigid body rocking causes the PT elongation, so this relationship is logical. The PT elements also recorded stresses lower than the pre-stress (T_{init}) in all four events: this is consistent with the behaviour

discussed in the design chapter, which suggested the PT element closest to the rocking toe will initially lose some stress as the rocking toe compresses. Finally, some variability is observed in the PT hystereses, especially in the M6 events. The variability in the PT response reflects the first mode shear and bending, in addition to the higher mode elastic flexure and shear response of the rocking panel; the backbone of the hystereses, which is more evident in the M7 events, reflects the rigid body rotation.

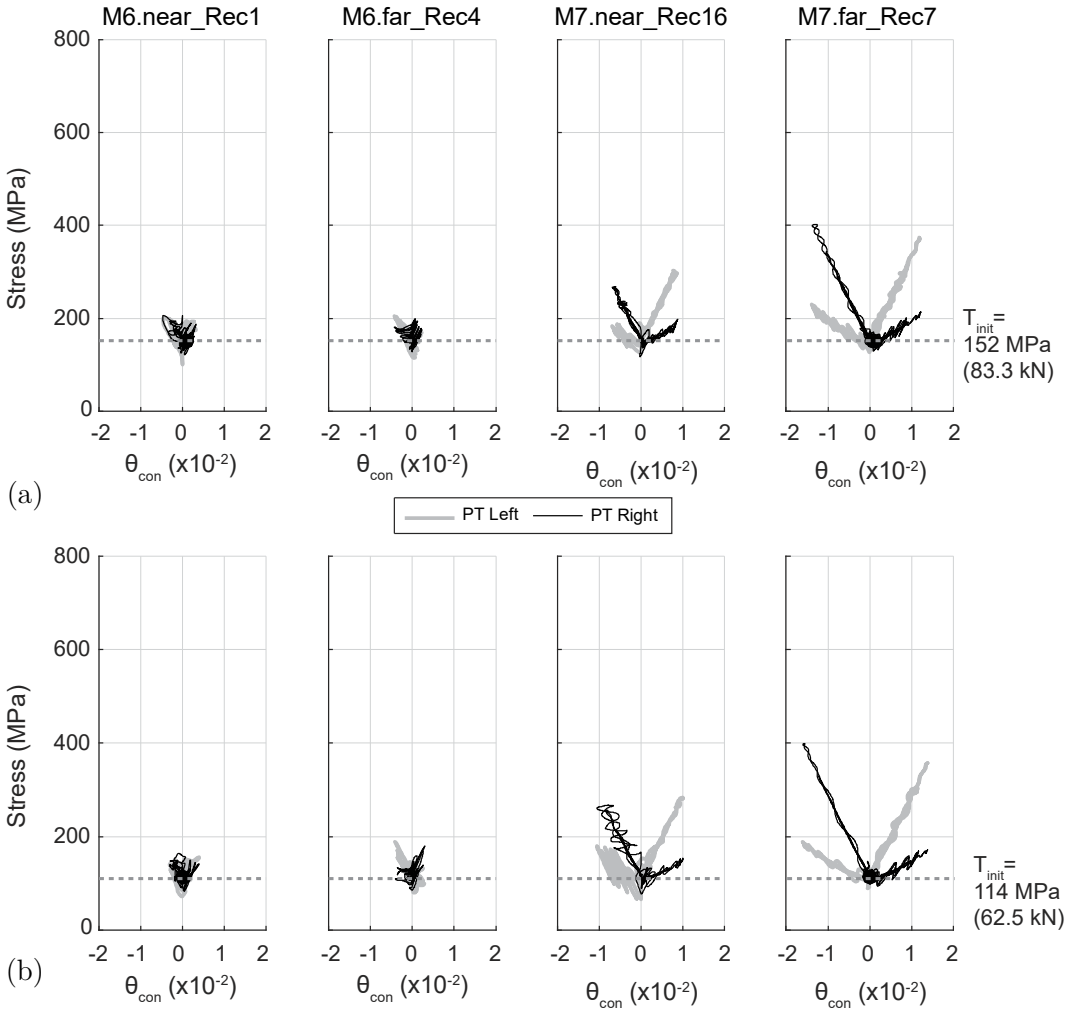

Figure 5.13: PT hysteresis for the (a) baseline model, and (b) lower-bound model

6 Collapse Fragility of Controlled Rocking Walls in Eastern Canada

An Incremental Dynamic Analysis (IDA) is conducted to evaluate the collapse fragility of a three-, six-, and nine-storey controlled rocking heavy timber structural design. The design of the three structures considered the moderate seismic hazard demand of Montreal, Quebec, in eastern Canada. All three designs are modelled in-plane, as per the numerical modelling theory presented in Chapter 4, and the models are subjected to a ground motion suite scaled to a specific intensity. The intensity is incrementally increased, and interstorey drifts are observed as a measure of collapse. The resulting peak interstorey drift response provides insight regarding the probability of collapse of the controlled rocking heavy timber system designed without supplemental energy dissipation.

6.1 Summary of Designs for Analysis

The designs considered in the following IDA investigation include three-, six-, and nine-storey controlled rocking CLT walls, designed for the seismic hazard of Montreal, Canada, with a 2% probability of exceedance in 50 years. Each baseline model is also associated with a lower-bound variation according to the modifications presented in Section 4.2.2. Specific controlled rocking wall design details are outlined below, and summaries of the design are presented in Table 6.1. For the lower-bound variation, several parameters are modified according to Table 4.5, including a reduced post-tensioning force, a reduced bending and shear stiffness of the wall, and a reduction in the Winkler spring stiffness within 200 mm of the rocking toes. The nine-storey design has a smaller footprint of 24 meters square (576 m^2), whereas the six- and nine-storey designs are 54 meters square (2,916 m^2). All three buildings were designed with the same tributary seismic weight (per unit area) as the prototype presented in Chapter 3.

Table 6.1: Summary of designs for IDA investigation

3-storey	6-storey	9-storey
Building Dimensions: 54 meters (square) x 9.9 meters (3.3 meters per storey)	Building Dimensions: 54 meters (square) x 19.8 meters (3.3 meters per storey)	Building Dimensions: 24 meters (square) x 29.7 meters (3.3 meters per storey)
Sample layout: 16 walls, each 2.44 m long 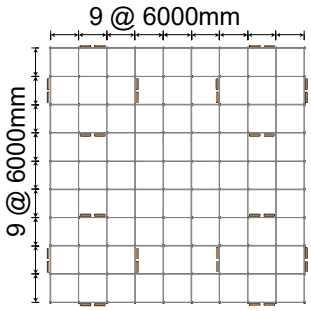	Sample layout: 12 walls, each 4.88 m long 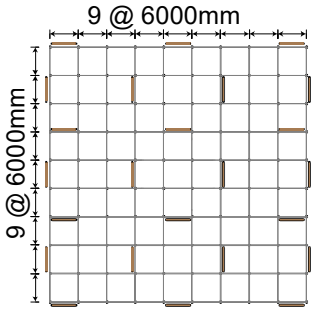	Sample layout: 8 walls, each 4.88 m long 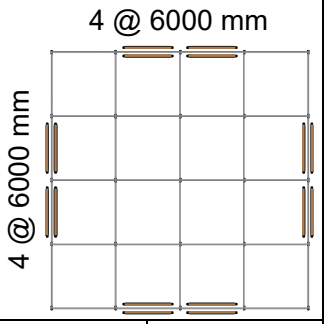
R_dR_o = 18.0 | T_n = 0.74 s	R_dR_o = 19.0 | T_n = 1.04 s	R_dR_o = 4.0 | T_n = 1.09 s
$M_{con,design}$ (seismic, wind) [1]: 1,891 kN·m, 1,050 kN·m	$M_{con,design}$ (seismic, wind) [1]: 5,350 kN·m, 5,170 kN·m	$M_{con,design}$ (seismic, wind) [1]: 11,000 kN·m, 10,600 kN·m
Peak non-linear θ_{roof} estimate (%): 2.3% (<2.5%)	Peak non-linear θ_{roof} estimate (%): 1.4% (<2.5%)	Peak non-linear θ_{roof} estimate (%): 0.5% (<2.5%)
Initial PT force per bar [2]:39 kN	Initial PT force per bar [2]:32 kN	Initial PT force per bar[2]:222 kN
[1] $M_{con,design}$ for the whole building. Wall designed for $M_{con,design}$/number of walls [2] PT elements and configurations within the wall are identified below		

Seismic demand on the three-storey design was determined with a force reduction factor (R_dR_o) of 18.0. This design is governed by the estimated peak non-linear roof drift of 2.5% for normal importance buildings (NRCC, 2010); the estimated peak drift is 2.3% for the design presented above. The three-storey design uses a 2.44 m long wall with post-tensioning (PT) bars located 600 mm from both edges of the wall (two PT bars total). The CLT panel is 315 mm thick, including nine layers; and the PT elements are 26 mm in diameter. The CLT panel and PT elements are the same as those specified in the prototype wall designed in Chapter 3, and studied in the previous chapters. Each PT element is post-tensioned to 39 kN, to resist a design seismic overturning moment of 118 kN·m/wall.

Seismic demand on the six- and nine-storey designs was determined with R_dR_o of 19.0 and 4.0, respectively. These factors were chosen to minimize the design seismic demand without reducing it below the design wind demand, determined using the Canadian building code (NRCC, 2010). In the nine-storey design, design-level wind loading governed the design of the base connection such that the seismic demand could not be reduced by an R_dR_o value larger than 4.0. The six- and nine-storey designs also use the same 26 mm diameter PT bar and nine-layer, 315 mm thick CLT panel as the three-storey design; however, the six- and nine-storey designs use 4.88 m long walls to increase the elastic stiffness of the designs. In the 4.88 m walls, PT elements are located 1220 mm from each edge (two PT bars total), and are pre-stressed to 32 kN and 220 kN in the six- and nine-storey design respectively.

6.2 Incremental Dynamic Analysis (IDA)

6.2.1 Background

IDA is performed by subjecting a structural model to a suite of ground motions, and increasing the ground motion intensity relative to the uniform hazard spectrum (UHS) level. The IDA process is outlined in the FEMA P695 report (Applied Technology Council, 2009) in which a full suite of ground motions is incremented until all the motions cause the model to collapse. The number of ground motions that caused collapse at each intensity increment is used to construct a collapse fragility curve, describing the probability that the structure will collapse if subjected to a certain level of ground motion relative to the UHS. Furthermore, the same process can provide limit state fragility curves, to determine the probability of meeting or exceeding other structural limits, such as peak bending moment or shear force demands.

Completing a full IDA for a suite of forty-four ground motions can be time consuming; therefore, Baker (2015) presented and investigated an alternative to conducting a full IDA procedure, called Multiple Stripes Analysis (MSA). The MSA method minimizes the number of IDA intensity increments needed to predict fragility curve parameters, including the median collapse intensity (θ) and the variance (β), assumed to be from a log-normal distribution. To predict these fragility parameters

with fewer analyses, the MSA procedure uses statistical inference: Baker (2015) uses a likelihood-function to calculate the likelihood that an available IDA dataset, observed at as few as two intensity increments, fits a particular log-normal distribution. Then the fragility curve parameters (θ and β) are defined to maximize the likelihood that the observed data comes from the log-normal distribution described by θ and β. By this procedure, the resulting fragility curve parameters are known as maximum likelihood estimates of the fragility curve (Baker, 2015).

Baker (2015) evaluated the MSA process using 45 ground motions at three intensity measures (135 analyses) near the mean collapse fragility, comparing the resulting fragility curve estimates against a full IDA process using 20 ground motions (227 analyses). With collapse data from just three intensity measures, MSA was shown to be more efficient, estimating approximately the same fragility curve parameters given 1,000 unique structural analysis data sets. It is important to note that some initial estimate of the θ parameter is required to reduce the IDA process to only three intensity measures. As such, a larger number of intensity levels can be spread over a wide range, in the practical application of MSA (Baker, 2015).

In the following sections, collapse, bending moment, and shear force limit state fragility curves are estimated for the three-, six-, and nine-storey designs, using MSA. The limit state for collapse is 10% peak interstorey drift, and the limit-state for bending moment and shear is taken as unity of the respective demand-capacity ratios. First, the number of limit state-exceedance events at several intensity measures is determined. Next, the quantities of exceedance events are input to Baker's (2015) maximum likelihood function, to determine θ- and β-parameters describing the log-normal fragility curves to which the IDA observations most likely belong.

6.2.2 Preparing the IDA Procedure

Forty-four ground motions are used from Atkinson (2009), consisting of eleven magnitude six and seven records, from both near and far sources. The median of the ground motion set is scaled to the 5%-damped UHS for Montreal, Canada (NRCC, 2010) at the first mode period (T_1) of each design; the amplification factor applied

to scale the ground motions beyond this intensity is the intensity measure (IM). The three-, six-, and nine-storey designs have periods of 0.74 s, 1.04 s, and 1.09 s, corresponding with scaling factors of 1.430, 1.315, and 1.450, respectively, for the UHS-level (IM=1). The three scaled ground motion sets are similar, and the UHS-level scaled spectra for the three-storey design is shown in Figure 6.1. Next, each scaled ground motion is scaled again, for a series of incremental dynamic analyses: Baker notes that MSA is not sensitive to the selection of IM's, and that the maximum likelihood estimate of collapse fragility parameters can benefit from more levels. Therefore, the ground motions are scaled from 50% (IM=0.5) to 700% (IM=7) of the UHS-level at 50% increments, and a NLTHA is conducted at each increment.

To account for various failure modes of the wall, several modifications are made to the model and to the analysis settings. To account for collapse of the model, peak interstorey drift is observed at each iteration of the analysis, and if it exceeds 10%, the analysis concludes. Also, to account for failure of the timber in the base connection, and because Newcombe's (2011) empirical Winkler spring relationship is only applicable up to twice the yield strain, the Winkler springs are limited to two times the yield strain in compression. Once this limit is reached, the spring is removed from the model. Furthermore, the PT bars are specified for up to 9% strain before fracture (DSI, 2015); however, large PT strains are likely to result in significant forces under the PT anchorage, crushing the timber and creating significant inelasticity in the overall PT response. Therefore, the PT elements are removed from the model if their tensile strain exceeds 2%. Further research is required to effectively model the PT response at large drifts, so the 2% limit is considered to be conservative for this collapse fragility investigation. Finally, a spring was included at the base of the PT elements to only allow tensile resistance.

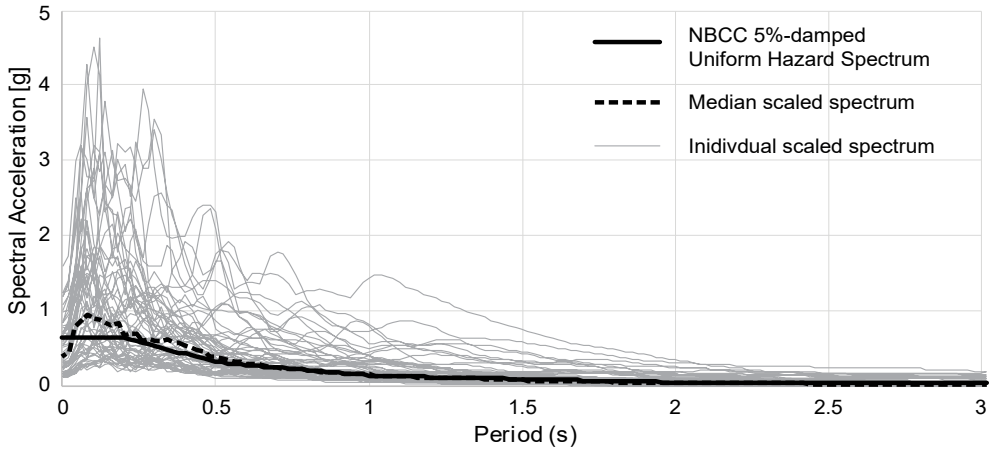

Figure 6.1: Scaled ground motions for IDA of the three storey design

6.2.3 Investigating Collapse

Several representative time-history records are presented in Figure 6.2 to investigate the concept of gravity system collapse in the IDA. The records include one each from the baseline and lower-bound variations of the three designs, showing the roof drift at the largest non-collapsed record, and at the subsequent IM that caused collapse. The roof drift time-histories in Figure 6.2 show similar behaviour before diverging when the roof drift is near a peak, at which point the roof drift increases rapidly in the failing record, ending the analysis due to an observed interstorey drift of 10% in one of the storeys, or due to non-convergence.

Collapse of the gravity system occurs when a large rocking motion causes several Winkler springs to fail. After several Winkler springs reach their maximum limit of twice the yield strain and their response is removed from the model, the rest of the springs can follow in succession, creating a rapid collapse mechanism. Furthermore, as Winkler springs are removed from the model, the re-adjustment of stresses in the rocking toe can cause a zipper effect of failing springs which is computationally difficult to analyze when the structural motion is still imposing larger drifts or increasing the forces in the rocking toe. These analyses required a reduced time-step of 0.0005 s (compared to 0.002 s for the other analyses), and a higher resolution of Winkler springs to achieve convergence in the analysis up to the time in the respective plots. This increased the analysis time by more than ten times that required for the preceding intensity, and sometimes this was still not able to converge

up to 10% drift; but the representative roof drift time-histories shown in Figure 6.2 demonstrate that non-convergence occurs as these models are collapsing. This issue was observed in several records, for all designs; however, it was most significant in the six- and nine-storey models because a given base rotation in the 4.88 m long walls requires a larger strain in the rocking toe.

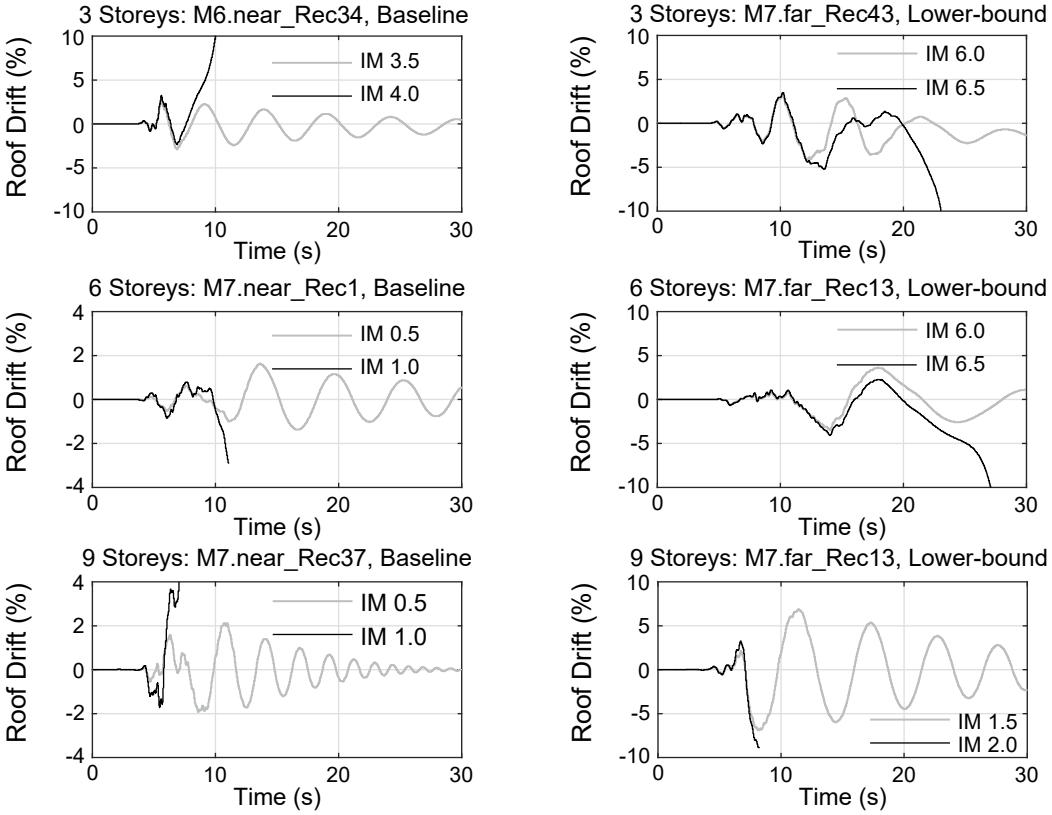

Figure 6.2: Roof drift time-histories from near-failing and failing records

6.2.4 IDA Results and Multiple Stripes Analysis (MSA)

The left side of Figure 6.3 shows the peak interstorey drift results from the IDA, for the baseline and lower-bound three-, six-, and nine-storey models. The IDA results are processed by MSA: the cumulative number of collapsed models at each IM are shown in the histogram in the middle of Figure 6.3, and the count is input to a likelihood function that is subsequently maximized according to Baker (2015), resulting in the collapse fragility curves presented on the right side of Figure 6.3. The collapse fragility curves are defined by θ and the record-to-record variability

(β_{RTR}) parameters identified on each plot. θ is also summarized in Table 6.2, along with the total variability parameter, β, for all three models. β is a function of the β_{RTR} term defined by the IDA results. However, β accounts for several additional uncertainty terms, as suggested by the FEMA P695 performance evaluation procedure (Applied Technology Council, 2009), including design requirements (β_{DR}), modelling (β_{MDL}), and the test data (β_{TD}); these terms are combined using Equation 5.1, where the additional uncertainty terms are taken as 0.5, since this is the most conservative value suggested by the FEMA P695 (Applied Technology Council, 2009). Table 6.2 also includes the probability of collapse at the UHS-level (IM=1) which corresponds with the Maximum Considered Earthquake (MCE) in the Canadian building code. The results generally estimate less than 10% probability of collapse in both the baseline and lower-bound three-, six-, and nine-storey models, with the exception of the baseline three-storey model, which has an 11.7% probability of collapse due to an MCE event. 10% is the suggested maximum limit by FEMA P695 (Applied Technology Council, 2009).

$$\beta = \sqrt{\beta_{RTR}^2 + \beta_{DR}^2 + \beta_{MDL}^2 + \beta_{TD}^2} \qquad \textbf{Equation 6.1}$$

Relatively lower probabilities of collapse are observed in the lower-bound IDA results, compared to the baseline in each design. This is because the larger Winkler spring stiffness in the baseline models, compared to the lower-bound models, results in a lower yield strain, as shown in Figure 6.4 (a). The lower yield strain means a lower failure strain ($\varepsilon_{failure}$, equal to twice the yield strain) causes the spring to be removed from the model. In comparison, the rocking toe springs in the lower-bound model are not removed until a larger strain, and therefore a larger rigid body rocking motion can occur before the extreme Winkler spring is removed, as shown in Figure 6.4 (b). The result is a relatively larger drift in the lower-bound IDA results, before the model losses its lateral stability due to the removal of Winkler springs.

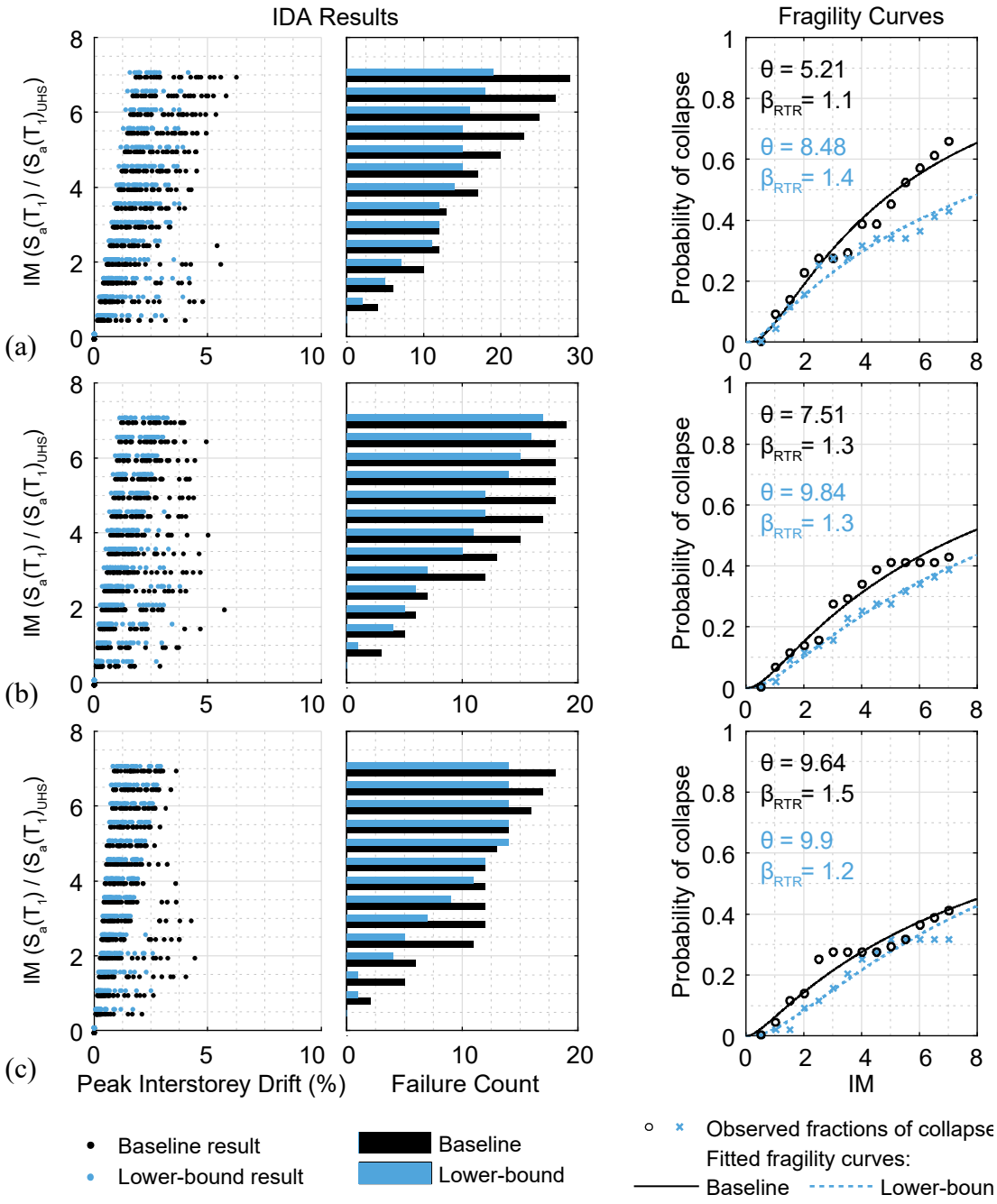

Figure 6.3: IDA results and collapse fragility curves for (a) three- (b) six-, and (c) nine-storey designs

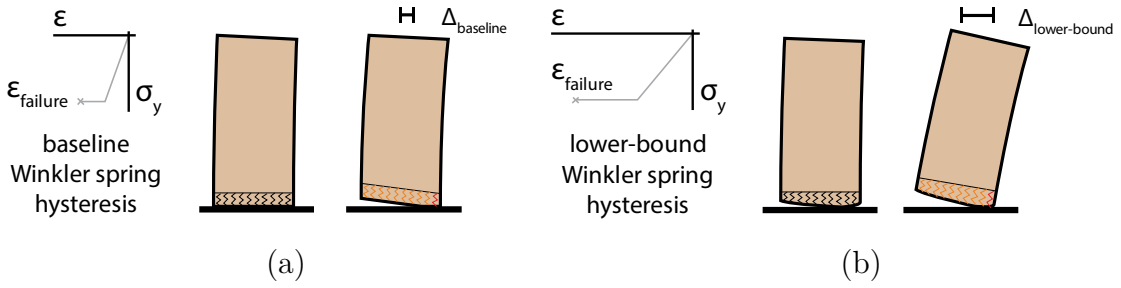

Figure 6.4: (a) Baseline and (b) lower-bound Winkler spring removal limits based on strain

Table 6.2: Fragility curve parameters and probabilities of collapse due to MCE-level event

	3-storey			6-storey			9-storey		
	θ	β	P[1](%)	θ	β	P[1](%)	θ	β	P[1](%)
Baseline	5.21	1.4	11.7	7.51	1.5	9.6	9.64	1.7	9.2
Lower-bound	8.48	1.6	9.7	9.84	1.5	6.7	9.90	1.4	5.6

[1] Probability of collapse due to MCE-event

The performance evaluation procedure in FEMA P695 suggests applying a spectral shape factor (SSF) to account for a conservative bias introduced by the spectral shape of the ground motion suite (Applied Technology Council, 2009). The SSF increases θ, thereby reducing the probability of collapse at the MCE-level, as shown in Figure 6.5. SSFs have been presented for the FEMA P695 ground motion suites, but have not been determined for the ground motion suites applied in this study, so no SSFs have been applied to the fragility curve results in this study.

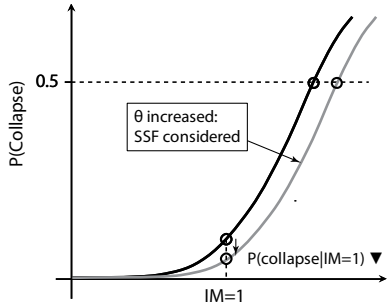

Figure 6.5: Increased probability of collapse due to consideration of spectral shape factor (SSF)

Recall that the definition of collapse in this fragility assessment is related to excessive roof drift of the gravity system. Limit states such as bending moment and shear failure due to higher mode effects are not captured in the model, and could occur prior to collapse of the gravity system. Additional research is needed to capture

these failure modes in the model, and this is discussed further in Section 6.3 and Chapter 7. However, to investigate the existing model, the IDA results in Figure 6.6 and Figure 6.7 consider the peak shear and bending moment demand-capacity ratios, respectively. A limit state exceedance event occurs if demand equals or exceeds shear or bending moment capacity of the CLT panel, as determined in Section 3.4.4; the capacity of the three designs is summarized in Table 6.3. The resulting fragility curves are presented alongside the IDA results, including the estimated fragility curve parameters from MSA.

Table 6.3: Shear and bending moment capacities

	V_{cap}	M_{cap}
3-Storey	960 kN	5,900 kN·m
6-Storey	1,920 kN	23,700 kN·m
9-Storey	1,920 kN	23,700 kN·m

Figure 6.6 and Figure 6.7 show that at the UHS-level intensity (IM=1), very few shear capacity exceedance-events were observed and no bending moment exceedance-events were observed in the three designs. However, the number of exceedance-events accumulates quickly compared to the interstorey drift exceedance-events (collapse) in Figure 6.3. This results in lower θ and β parameters for the fragility curves, and lower probabilities of exceedance at the MCE-level for the shear and bending moment demand-capacity limit state, as shown in Table 6.4, compared to the collapse limit states (see Table 6.2); Figure 6.8 includes the collapse and both the demand-capacity limit state fragility curves, overlaid for a graphic comparison.

Table 6.4: Shear and bending moment demand-capacity curve parameters

		3-storey			6-storey			9-storey		
		θ	β_{RTR}	P^1(%)	θ	β_{RTR}	P^1(%)	θ	β_{RTR}	P^1(%)
Shear	**Baseline**	3.87	0.71	2.8	3.13	0.64	3.8	5.16	0.76	1.5
	Lower-bound	4.44	0.74	2.2	3.73	0.68	2.5	6.33	0.69	0.4
Bending Moment	**Baseline**	5.39	0.85	2.3	5.27	0.72	1.0	7.18	0.96	2.0
	Lower-bound	6.62	0.91	1.9	7.09	0.86	1.1	8.37	0.85	0.6

[1] Probability of collapse due to MCE-event

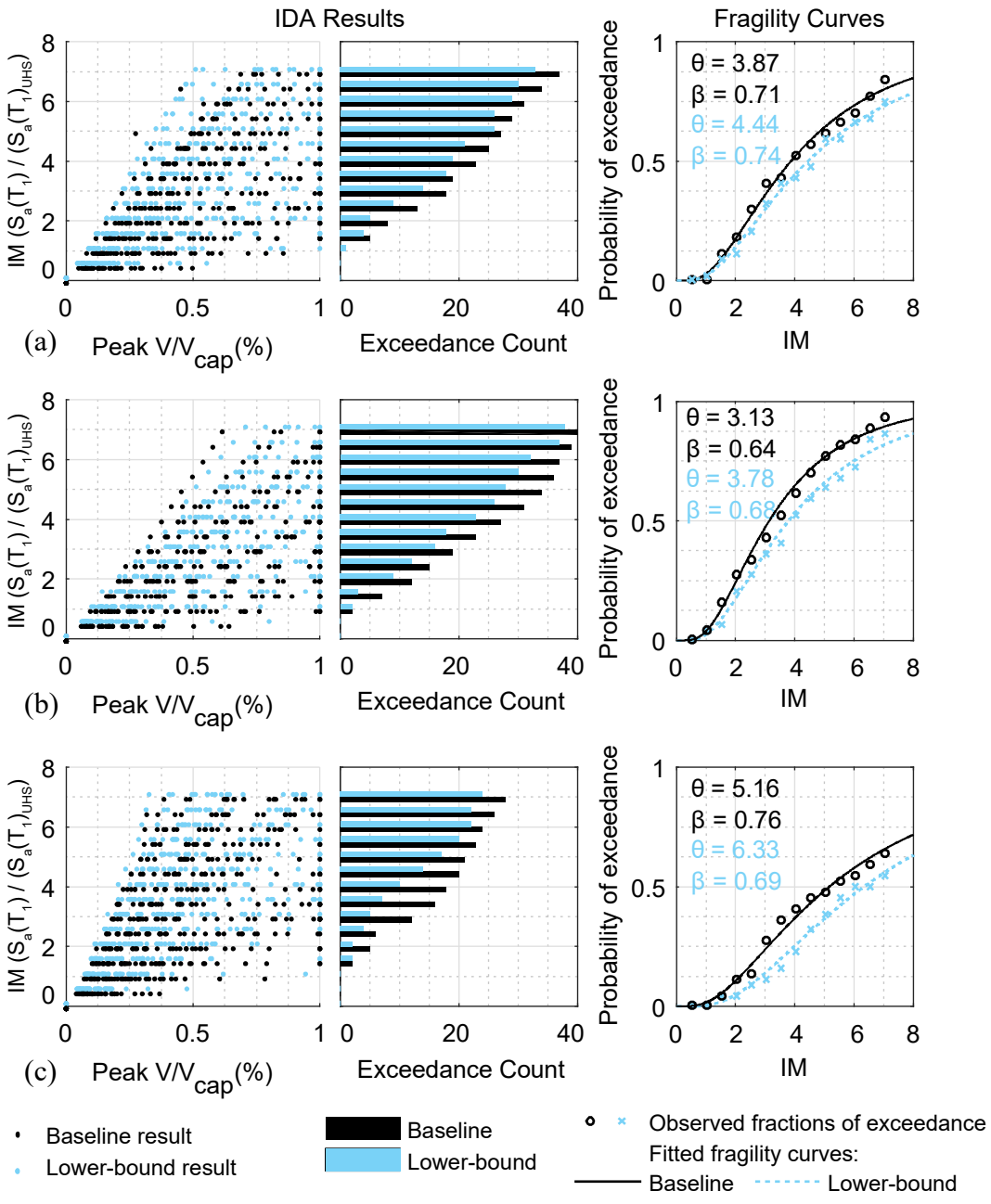

Figure 6.6: Peak shear demand-capacity and fragility curves for (a) three- (b) six-, and (c) nine-storey designs

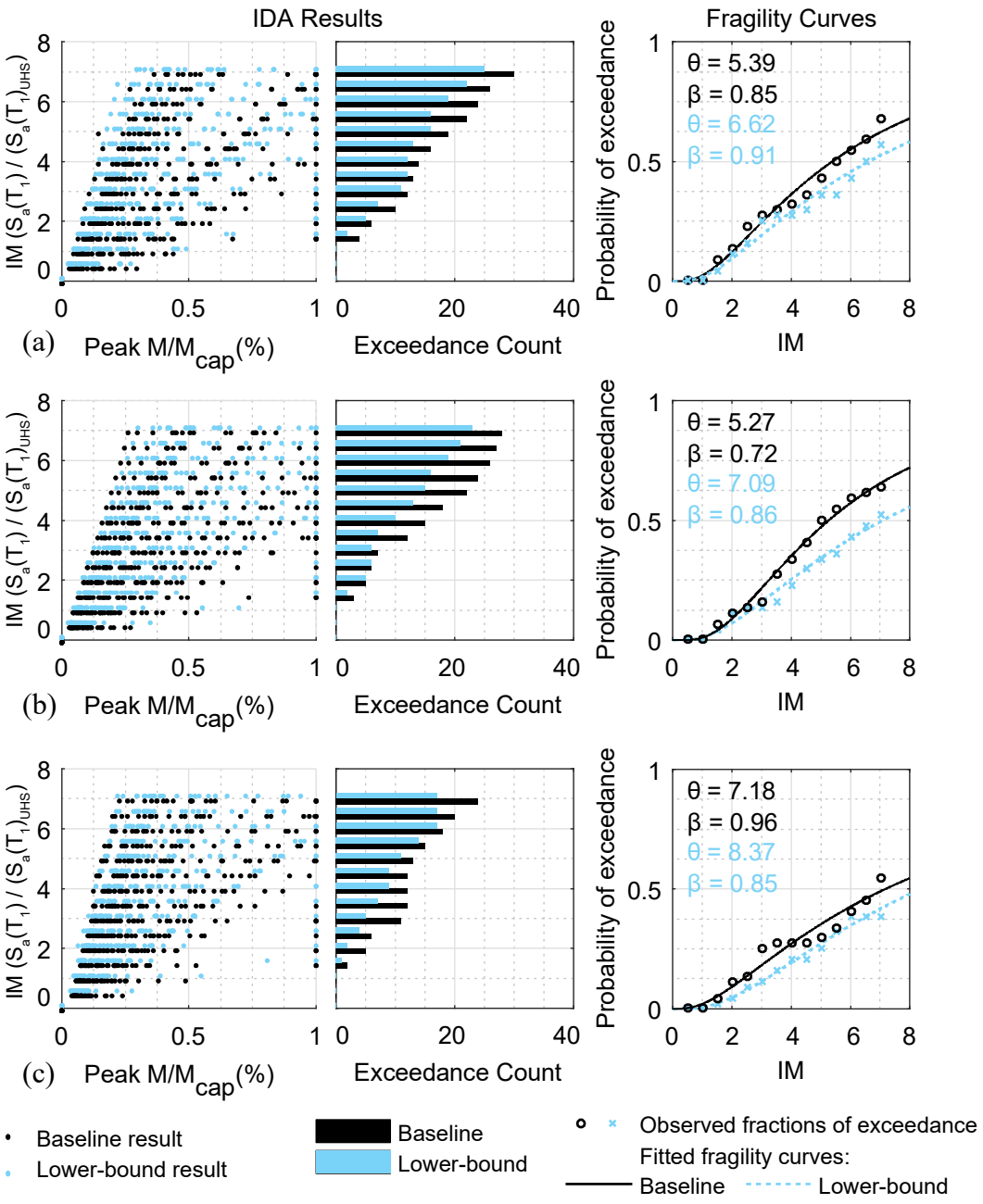

Figure 6.7: Peak bending moment demand-capacity and fragility curves for (a) three- (b) six-, and (c) nine-storey designs

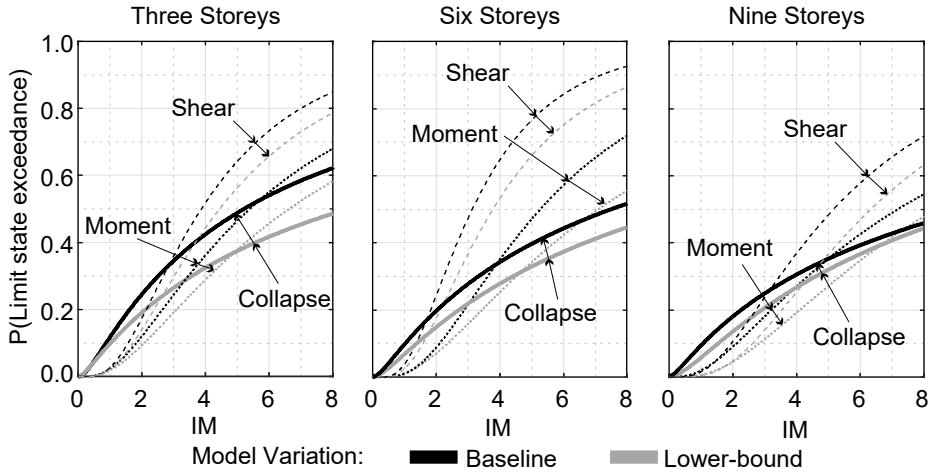

Figure 6.8: Comparison of limit state fragility curves estimated by MSA

6.3 Effects of the Model Limitations

The PT elements are modeled with the Steel02 material in OpenSees, as per Sarti (2015). Sarti selected Steel02 material parameters according to the modulus of elasticity, yield strength, curvature factor, and post-yield stiffness specified by a PT bar manufacturer. This material model was applied in the earlier investigation and verification of the baseline controlled rocking wall numerical model in Chapter 4, where the PT forces were not as large as in the IDA, and the PT was not yielding. In Section 4.2.2, a lower-bound model was proposed to capture some minor timber crushing under the PT anchorage from the available experimental data; the stress-strain relationships for the baseline and lower-bound PT models are shown in Figure 4.7. However, although the lower-bound model captured some minor timber crushing, the material parameters require further validation because the PT behaviour has not been verified at the large drifts observed in the IDA. Considering the effects on this study: the PT elements are removed from the numerical model if they reach 2% tensile strain to avoid overestimating the PT contribution at large drifts. However, the PT elements would likely still be capable of some contribution to preventing the controlled rocking at large drifts; therefore, this limitation has a conservative effect on the IDA results.

As per the collapse investigation in Section 6.2.3, there is also a limit on the Winkler spring response: the springs are removed after reaching twice the

compressive yield strain. This issue results in a lower-bound estimate of the controlled rocking wall collapse fragility estimate, since the sudden loss of base connection strength is unlikely to occur in practice: experimental observations by Ganey (2015) observed very little loss of CLT strength at roof drifts of 5%, and in most cases, up to 7.5%.

Finally, the controlled rocking wall's shear and bending moment failures are not reflected in the model's behaviour. However, as shown in Figure 6.8, the exceedance of shear force and bending moment capacities is a probable occurrence at larger intensities. Although the exceedance of shear and bending moment capacity is not expected to cause immediate collapse, the response of the model beyond this exceedance event is not reflected in the non-linear time-history analysis. This could affect the collapse IDA results, since the model's response is likely to be different after exceeding either of these limit states. This is discussed in Chapter 7 as an opportunity for future research.

7 Conclusions & Future Research

This chapter reviews the conclusions drawn from the previous chapters, and discusses opportunities for future research. Many of these opportunities were also highlighted in the previous chapters, but additional insight is provided here.

7.1 Summary

This thesis proposed and investigated controlled rocking heavy timber walls for application in low-to-moderate seismic hazard regions. Controlled rocking heavy timber walls were presented as a resilient structural alternative that is already in use in high seismic hazard regions; it was suggested that the system could be more suitable for low-to-moderate seismic hazard regions by adapting it to use local timber products, and by designing them without supplemental energy dissipation, to minimize design and construction costs and challenges. Furthermore, the proposed walls use cross-laminated timber (CLT) panels instead of the laminated-veneer lumber (LVL) products used in existing studies and commercial applications because the Canadian government has cited CLT as a significant economic and environmental opportunity for Canada and the United States.

First, existing analysis and design procedures were investigated, considering controlled rocking LVL and controlled rocking steel braced frame research. These procedures were critically evaluated and adapted for controlled rocking CLT walls. Furthermore, the results from Zhang (2015), regarding the behaviour of self-centering single-degree of freedom (SDOF) systems, were incorporated into the design and analysis of controlled rocking CLT walls; Zhang's research suggested that a wall could be designed without energy dissipation, and with a relatively large force reduction factor, whiles still controlling the peak displacement demand. Next, three higher mode estimation procedures were investigated and applied to the controlled rocking heavy timber system. Using the design, analysis, and higher mode estimation procedures, a six-storey prototype controlled rocking CLT structure was designed and analyzed for the moderate seismic hazard of Ottawa, Ontario, as an example.

A baseline numerical model of the controlled rocking wall was presented and validated using experimental data from Sarti (2015). A lower-bound variation of the numerical model was also calibrated, considering timber damage and other behavioural observations from Sarti's experimental program. After validating the baseline and lower-bound models, the Ottawa prototype was modelled and investigated using non-linear time-history analyses, also considering a lower-bound variation of the prototype. The analysis results include general system performance and an investigation of higher mode effects.

Finally, three additional designs, including three-, six-, and nine-storey buildings, were presented for the moderate seismic hazard of Montreal, Canada, and modeled numerically. The models were subjected to an incremental dynamic analysis (IDA) procedure to investigate the limit state fragility of the controlled rocking CLT wall designed without energy dissipation. The limit states considered include collapse of the gravity system, and both shear and bending moment capacity.

7.2 Conclusions

The design and analysis procedures, and the numerical model presented in this thesis rely on a controlled rocking wall base connection model called the Winkler Spring Analogy (WSA) presented by Newcombe (2011). The WSA model was selected because Newcombe (2015) found that it was the most capable of predicting crushing at the base of a controlled rocking heavy timber wall panel, and because CLT has lower strength and stiffness than the LVL products used in past controlled rocking heavy timber research. By applying the WSA in the prototype controlled rocking CLT design and analysis example, the quasi-static and dynamic response of a representative numerical model was found to closely match the predicted base connection performance and overall controlled rocking wall behaviour.

The design and analysis procedures also considered several unique features. For example, widely-spaced post-tensioning (PT) elements were specified in order to minimize the concentration of PT forces at the top of the timber panel; this resulted in a relatively significant concentrated moment at the top of the controlled rocking

wall, which was incorporated into the analysis procedure. Furthermore, because the design process is based on a force-based design methodology, controlled rocking behavioural research is cited in order to estimate the peak non-linear system displacement based on the amount of energy dissipation, the natural period of the system, and a relatively large force reduction factor. Adding this step in the design process allows the design forces, including the initial PT force and base connection moment, to be minimized while controlling the peak displacement response to within building code limits. By considering widely-spaced PT elements, and by estimating the displacement response without energy dissipation and with a relatively large force reduction factor, the cost and complexity of the controlled rocking heavy timber wall design and construction process is reduced.

The six storey prototype, designed for the moderate seismic hazard region of Ottawa, Canada, required twenty-four controlled rocking CLT walls, each 2.44 m long, allowing for a relatively open floor-plan. Supplemental energy dissipation elements were omitted, and a force reduction factor of 8.0 was used. The estimated peak roof displacement was 0.83% drift, and the three higher mode estimation procedures produced relatively consistent shear demand-capacity ratios between 32% and 35%, and bending moment demand-capacity ratios between 24% and 36%.

The OpenSees numerical model, compared with Sarti's (2015) experimental results, provided insight regarding the numerical modelling of a controlled rocking wall. Using the WSA, the numerical model closely reflected Sarti's experimental results without the calibration to experimental data that is required for the MBA. Furthermore, a lower-bound variation was able to bracket the experimental and baseline numerical model responses, using modifications that are explained by variations in timber material properties, and by observations in the experimental program described by Sarti (2015), such as lateral slip in the timber panel, and rocking toe damage due to repeated testing. This investigation verified the Winkler spring model for application in future controlled rocking CLT studies.

Baseline and lower-bound models of the prototype design were subjected to a suite of ground motions representing a 2% chance of exceedance in fifty years, and

the models' performance was compared to the design and analysis results. Considering the baseline model, the mean peak non-linear roof drift (0.65%) is 22% lower than estimated in the design procedure (0.83%). It was suggested that the result may be attributed to the design equations from Zhang (2015), which were calibrated for non-zero energy dissipation and for ground motions with more low-frequency content than is expected in Eastern North America; this is discussed further in Section 7.3, for future research needs. The lower-bound model showed a negligible difference in peak drifts.

The baseline and lower-bound models also exhibited significant higher mode effects, causing large peak force demands over the height of the wall. The peak demands were found to be significantly larger at the mid-height of the wall than at the base, contrasting with less substantial differences found by Sarti (2015) and Newcombe (Newcombe, 2011). The contrast is partially attributed to the relatively significant high-frequency content of Eastern Canadian ground motions, which strongly influence the higher mode effect. It is also partially attributed to the lower bending and shear stiffness properties of CLT, compared to LVL, which affects the dynamic behaviour of the controlled rocking wall. Nonetheless, the higher mode estimation procedures generally agree with the mean peak shear and bending moment demands over the height of the prototype wall: the largest difference between the mean NLTHA response and the higher mode estimation procedures in the peak shear and bending moment estimates is -7% and 10%, respectively. Also, the higher mode effects in the lower-bound variation are 10-20% lower than those in the baseline model.

The maximum mean peak storey acceleration was 0.85 g in the baseline model, and 0.83 g in the lower-bound model. This is relatively low, compared to recommendations for considering non-structural elements (Rahman & Sritharan, 2007).

IDA studies on a three-, six-, and nine-storey design demonstrated several limit state fragilities for the controlled rocking heavy timber wall. The resulting collapse fragility curves demonstrate between five and twelve percent probability of collapse

due to excessive interstorey drifts at the MCE-level intensity. Furthermore, the resulting bending moment and shear limit state fragility curves suggest an even lower probability of exceeding their respective capacities at the MCE-level. However, the probability of exceedance rapidly overtakes the probability of collapse beyond the MCE-level. This motivates future research regarding these failure modes in controlled rocking CLT panels, as discussed in Section 7.3.

7.3 Future Research

Estimating the Initial Period of the Structure

Sarti (2015) showed that initial period estimates in existing building code standards are insufficient for the controlled rocking heavy timber walls. The Rayleigh method was presented as the most appropriate means of checking an initial estimate; but according to the force-based design process in Chapter 3, an initial period estimate is still needed for an initial controlled rocking wall design, so a method (similar to the existing building code expressions) should be investigated.

Considering the natural period of an initial design, Sarti presented a modified Rayleigh method, suggesting that the controlled rocking heavy timber wall design should be based on the yield-secant stiffness. However, it has not been verified that the yield-secant stiffness is the most appropriate for design. Furthermore, Sarti's Rayleigh method modifier is specific to the Monolithic Beam Analogy (MBA), because it is a function of base connection stiffness factors in numerical modeling, such as the timber elastic modulus and the calibration parameters (see the final step of the design process, Chapter 3). Sarti's modifier increased the natural period by 40%, whereas the modifier presented for the Winkler Spring Analogy (WSA) only required an increase of 12%. Therefore, the modified Rayleigh method should be investigated further to improve the design process.

Estimating Post-Tension (PT) Losses and Understanding PT Behaviour in CLT

Long-term PT behaviour studies have been motivated by controlled rocking LVL research (Davies & Fragiacomo, 2011; Fragiacomo et al., 2011; Yeoh et al., 2012). The same long-term behaviour studies are required with CLT, because of the unique

material properties and dimensional composition of CLT, and the variety of timber species that can be used to produce CLT. Furthermore, the long-term stresses in controlled rocking walls presented in this thesis are significantly lower than in the New Zealand research and commercial applications (Devereux et al., 2011; Opus International Consultants, 2014; Palermo et al., 2012). Therefore, research is required to quantify the long-term PT losses in these designs for low-to-moderate seismicity.

Modeling the CLT Base Connection with Winkler Springs

Newcombe found that the wall length to neutral axis depth relationship was the most significant factor in the definition of the Winkler spring stiffness for the WSA describing the controlled rocking heavy timber base connection. However, the orthotropic properties of the timber panel (which are different in CLT and LVL) also had a small effect on the base connection stiffness (Newcombe, 2011). Furthermore, Newcombe's testing and definition of the effective Winkler spring length relied on finite element models for LVL; physical CLT panel testing was not conducted. Therefore, the Winkler spring's effective stiffness, and its application to CLT panels, should be evaluated. Both finite element models and physical testing should be considered, to understand how the WSA applies to the unique composition of CLT, and if any modification is required for a better fit to CLT performance.

The in-plane compression behaviour of CLT should also be studied, so that a base connection material model can better reflect the behaviour of CLT in compression. It is expected that this would improve both the accuracy and the numerical stability of the incremental dynamic analyses, and also allow for further evaluation of the controlled rocking heavy timber performance by capturing the state of damage in the base connection.

Scaling Effects on Experimental Controlled Rocking Wall Performance

In Chapter 4, two scaling effects were identified in the experimental model presented by Sarti (2015), which were not matched by the numerical model presented in the same chapter. First, Sarti spaces two PT elements within the centre 20% of the wall length, resulting in especially concentrated forces due to the reduced scale of the experimental specimen. These concentrated forces increase the potential for

local timber damage, which could be significant in future research testing since full-scale rocking walls with wider-spaced PT elements will not experience the same concentration of PT forces, and will therefore exhibit different timber crushing behaviour. This can be accounted for by testing a wider spaced PT configuration, to minimize the influence of crushing under the PT anchorage, or incorporating the crushing effect into future numerical modeling. Also, Sarti's PT was embedded in the foundation for a length equal to 25% of the wall height, whereas the numerical model considered the PT anchored at the wall base. This difference was identified as geometric incompatibility that could affect the numerical model comparison to the experimental data. This scaling effect should be considered in future modeling and testing research by either considering the PT embedment in design of a test specimen, or testing a full scale specimen.

Displacement Estimates According to Self-Centering SDOF Theory

Self-centering SDOF research by Zhang (2015) supports the design of controlled rocking heavy timber walls with relatively large force-reduction factors by characterizing the system response (i.e. peak displacement) as a function of various design parameters. This allows the designer to estimate the peak roof displacement given an initial controlled rocking heavy timber wall design. Zhang's regression equations for characterizing the system response were developed using a set of relatively low-frequency ground motions from California, as opposed to the Eastern Canadian ground motions used in this thesis, and Zhang's equations were conservative for self-centering systems without supplemental energy dissipation (i.e. β=0) and these are likely the reasons why the peak displacement was overestimated for the prototype studied in this thesis. Therefore, Zhang's regression equations should also be developed for high-frequency seismic hazards, and for non-dissipative systems, to improve the displacement estimation step of the design procedure.

Consideration of Controlled Rocking Heavy Timber Archetypes

Chapter 3 identified the potential for significant variations in the seismic weight of heavy timber structures, due to the relatively low weight of timber compared to other structural and non-structural components. This variation was identified

through a review of previous heavy timber structural research which considered significantly different seismic masses in their sample designs: using mass density as a measure, the lightest model was an open-concept controlled rocking heavy timber design with a density of 0.15 kN/m^3, whereas the heaviest design considered more internal CLT walls and a heavy floor, resulting in a density of 1.18 kN/m^3. Therefore, as per FEMA P695 (Applied Technology Council, 2009), it is especially important to consider high and low gravity design variations in order to draw general conclusions about controlled rocking heavy timber performance in future research.

Higher Mode Mitigation

Sarti (2015) and Ganey (2015), have suggested the development of higher mode mitigation techniques to address capacity design for higher mode effects observed in mid-rise controlled rocking heavy timber models. In particular, Sarti and Ganey cited Wiebe (2013), suggesting multiple rocking sections to limit the higher mode effects. However, the performance results of the controlled rocking walls in this study suggest that higher mode mitigation techniques may not be necessary because the shear and bending moment demands were relatively low in three different archetypes. Further incremental dynamic studies with different archetypes, according to FEMA P695 recommendations, could help to explore the need for higher mode mitigation techniques. Nonetheless, the research presented in this thesis supports the application of higher mode mitigation techniques, like multiple rocking sections, through the investigation of three capacity design methods to improve the estimation of higher mode force demands over the height of the controlled rocking wall. Therefore, future higher mode mitigation research can more effectively consider the performance of multiple rocking sections in controlled rocking heavy timber walls. Further research will also have to address the connectivity of multiple rocking sections, as the relatively soft timber connections may behave differently than the steel frames with multiple rocking joints that were investigated by Wiebe (2013).

Bending Moment and Shear: Capacity and Failure Modes

Section 3.4.4 demonstrated the bending moment and shear capacity calculation; however, this section also highlighted the uncertainty associated with these capacity

terms, especially for large scale specimens like the nine-layer CLT panel. Furthermore, the IDA investigation in Chapter 6 highlighted the potential for bending moment or shear failure to occur at relatively large ground motion intensities compared to the MCE-level, which could affect the collapse assessment of the controlled rocking system since the bending moment and shear failure modes are not captured by the model. Although the shear and bending moment failures are not expected to cause immediate collapse of the system, it is important to model the bending moment and shear capacity failures for a better understanding of the controlled rocking heavy timber fragility analysis. Future research should be conducted to capture the shear and bending moment failure modes with the numerical model.

System Damping Contributions

In the numerical model analyses presented in this thesis, only Rayleigh damping was used to damp the system response. However, the Rayleigh damping model and the assumption of 5% critical damping applied to the first and third modes has not been studied for controlled rocking CLT walls. This damping assumption should be studied further using experimental studies, considering the controlled rocking wall panel on its own, and also considering an entire controlled rocking structure, complete with non-structural elements. It may be necessary to change the damping model entirely, or to use a different level of critical damping, in future controlled rocking heavy timber wall studies. Furthermore, the base connection impact was identified as another possible source of damping: Marriott (2009) suggested disregarding impact damping when hysteretic (supplemental) energy dissipation was included in a controlled rocking system, because the latter was significantly larger, but supplemental energy dissipation is omitted in the proposed controlled rocking heavy timber wall for regions of low-to-moderate seismicity. The nature of impact damping in a controlled rocking wall with a soft base connection, as opposed to a stiff base connection (for example, as in precast concrete), should be evaluated further. Including this damping term could help to reduce the system response, as additional energy will be dissipated as the system rocks.

References

AIR Worldwide. (2013). *Study of Impact and the Insurance and Economic Cost of a Major Earthquake in British Columbia and Ontario/Quebec*.

Andreolli, M., Tomasi, R., & Polastri, A. (2012). Experimental investigation on in-plane behaviour of cross-laminated timber elements. In G. Rainer (Ed.), *CIB - W18* (pp. 1–11). Vaxjo, Sweden.

Applied Technology Council. (2009). *Quantification of Building Seismic Performance Factors. FEMA Report P695*. Washington, D.C.

Atkinson, G. M. (2009). Earthquake time histories compatible with the 2005 National building code of Canada uniform hazard spectrum. *Canadian Journal of Civil Engineering*, *36*(6), 991–1000. http://doi.org/10.1139/L09-044

Atkinson, G. M., Bouaanani, N., Daneshvar, P., Koboevic, S., Léger, P., & Tremblay, R. (2015). Selection and scaling of ground motion time histories for seismic analysis using NBCC 2015. In *Canadian Conference on Earthquake Engineering*. Victoria, B.C.

Baker, J. W. (2015). Efficient analytical fragility function fitting using dynamic structural analysis. *Earthquake Spectra*, *31*(1), 579–599. http://doi.org/10.1193/021113EQS025M

Bocchini, P., Frangopol, D. M., Ummenhofer, T., & Zinke, T. (2014). Resilience and Sustainability of Civil Infrastructure: Toward a Unified Approach. *Journal of Infrastructure Systems*, *20*(2), 04014004. http://doi.org/10.1061/(ASCE)IS.1943-555X.0000177

Bosher, L. (2008). Introduction: The Need for Built-in Resilience. In L. Bosher (Ed.), *Hazards and the Built Environment: Attaining Built-in Resilience* (p. 400). New York, N.Y.: Routledge.

Buchanan, A. H., Bull, D., Dhakal, R., Macrae, G., Palermo, A., & Pampanin, S. (2011). *Base Isolation and Damage-Resistant Technologies for Improved Seismic Performance of Buildings*. Christchurch, New Zealand.

Buchanan, A. H., Deam, B., Fragiacomo, M., Pampanin, S., & Palermo, A. (2008). Multi-Storey Prestressed Timber Buildings in New Zealand. *Structural*

Engineering International, *18*(2), 166–173. http://doi.org/10.2749/101686608784218635

Canterbury Earthquake Recovery Authority. (2012). Christchurch Central Recovery Plan.

Canterbury Earthquakes Royal Commission. (2012). *Royal Commission Report on Low-Damage Building Technologies, Volume 3*. Christchurch, New Zealand.

Ceccotti, A., Follesa, M., Lauriola, M. P., & Sandhaas, C. (2006). Sofie Project–Test Results on the Lateral Resistance of Cross-Laminated Wooden Panels. In *Proceedings of the First European Conference on Earthquake Engineering and Seismicity* (p. 10). Geneva, Switzerland. Retrieved from http://www.timberengineering.it/Pubblicazioni/img/Articoli_scientifici/2006_ECEES_Test results.pdf

Charney, F. A. (2008). Unintended Consequences of Modeling Damping in Structures. *Journal of Structural Engineering*, *134*(4), 581–592. http://doi.org/10.1061/(ASCE)0733-9445(2008)134:4(581)

Chopra, A. K. (2007). *Dynamics of Structures: Theory and Applications to Earthquake Engineering* (Third Edit). Pearson.

Chopra, A. K., & Goel, R. K. (1997). *Vibration properties of buildings determined from recorded earthquake motions. Earthquake Engineering Research Center, College of Engineering - University of California at Berkeley* (Vol. UCB/EERC-9). Berkeley, California.

Chopra, A. K., & McKenna, F. (2015). Modeling viscous damping in nonlinear response history analysis of buildings for earthquake excitation. *Earthquake Engineering & Structural Dynamics*, *137*(2), 193–211. http://doi.org/10.1002/eqe.2622

Christopoulos, C., Filiatrault, A., Uang, C.-M., & Folz, B. (2002). Posttensioned Energy Dissipating Connections for Moment-Resisting Steel Frames. *Journal of Structural Engineering*, *128*(9), 1111–1120. http://doi.org/10.1061/(ASCE)0733-9445(2002)128:9(1111)

Davies, M., & Fragiacomo, M. (2011). Long-Term Behavior of Prestressed LVL Members. I: Experimental Tests. *Journal of Structural Engineering*, *137*(12),

1553–1561. http://doi.org/10.1061/(ASCE)ST.1943-541X.0000405

Dehghani, M., & Tremblay, R. (2016). Robust Period-Independent Ground Motion Selection and Scaling for Effective Seismic Design and Assessment. *Journal of Earthquake Engineering*, *20*(2), 185–218. http://doi.org/10.1080/13632469.2015.1051635

Department of Economic and Social Affairs: Population Division. (2014). *World Urbanization Prospects: The 2014 Revision*. New York, N.Y. Retrieved from http://esa.un.org/unpd/wup/Highlights/WUP2014-Highlights.pdf

Devereux, C. P., Holden, T. J., Buchanan, A. H., & Pampanin, S. (2011). NMIT Arts & Media Building - Damage Mitigation Using Post-tensioned Timber Walls. In *Pacific Conference on Earthquake Engineering* (pp. 1–8). Auckland, New Zealand.

DSI. (2015). DYWIDAG Post-Tensioning System using Bars. DYWIDAG Systems International. Retrieved from https://www.dsicanada.ca/products/post-tensioning/bar-post-tensioning-system/metric-steel-properties.html

Dunbar, A., Pampanin, S., & Buchanan, A. H. (2014). Seismic Performance of Core-Walls for Multi-Storey Timber Buildings. In *New Zealand Society of Earthquake Engineering Conference*.

Dunbar, A., Pampanin, S., Palermo, A., & Buchanan, A. H. (2013). Seismic Design of Core-walls for Multi-Storey Timber Buildings. In *New Zealand Society of Earthquake Engineering Conference*.

Filippou, F. C., Popov, E. P., & Bertero, V. V. (1983). *Effects of Bond Deterioration on Hysteretic Behavior of Reinforced Concrete Joints* (Report No. EERC-83/19). Berkeley, California.

Fischer III, H. W., Scharnberger, C. K., & Geiger, C. J. (1996). Reducing seismic vulnerability in low to moderate risk areas. *Disaster Prevention and Management*, *5*(4), 5. http://doi.org/10.1108/09653569610127398

Flaig, M. (2014). Design of CLT Beams with Rectangular Holes or Notches. In *International Network on Timber Engineering Research*. Bath, UK.

Flaig, M., & Blass, H. J. (2013). Shear Strength and Shear Stiffness of CLT-Beams Loaded In Plane. In *CIB-W18/46-12-3*. Vancouver, B.C.

Fragiacomo, M., & Davies, M. (2011). Long-Term Behavior of Prestressed LVL Members. II: Analytical Approach. *Journal of Structural Engineering*, *137*(12), 1562–1572. http://doi.org/10.1061/(ASCE)ST.1943-541X.0000410

Gagnon, S., Mohammad, M., Toro, W. M., & Popovski, M. (2014). Evaluation of In-Plane Shear Strength of CLT. In *World Conference on Timber Engineering* (pp. 1–7). Quebec City, Quebec.

Gagnon, S., & Pirvu, C. (2011). *CLT Handbook*. (S. Gagnon & C. Pirvu, Eds.) (Canadian E). Quebec City, Quebec: FPInnovations.

Ganey, R. S. (2015). *Seismic Design and Testing of Rocking Cross Laminated Timber Walls* (Master of Science). University of Washington.

Gavric, I., Fragiacomo, M., Popovski, M., & Ceccotti, A. (2013). Behaviour of Cross-Laminated Timber Panels under Cyclic Loads. In *Materials and Joints in Timber Structures* (pp. 689–702). Dordrecht: Springer Netherlands. http://doi.org/10.1007/978-94-007-7811-5_62

Giardini, D., Grunthal, G., Shedlock, K., & Zhang, P. (1999). Global Seismic Hazard Map. Retrieved from http://www.seismo.ethz.ch/static/GSHAP/

Green, M. C. (2011). CLT at Murray Grove – the world's tallest modern timber residential building. Wood Solutions. Retrieved from http://www.woodsolutions.com.au/Blog/Dream-big-and-innovate

Guéguen, P., Michel, C., & LeCorre, L. (2007). A simplified approach for vulnerability assessment in moderate-to-low seismic hazard regions: application to Grenoble (France). *Bulletin of Earthquake Engineering*, *5*(3), 467–490. http://doi.org/10.1007/s10518-007-9036-3

Hare, J., Oliver, S., & Galloway, B. (2012). Performance Objectives for Low Damage Seismic Design of Buildings. In *New Zealand Society for Earthquake Engineering Conference*. Christchurch, New Zealand.

Horvat, D. (2013). *Stability Behavior of Cross Laminated Timber (CLT) Columns Under Compressive Axial Load* (Masters of Science). University of British Columbia.

Iqbal, A., Pampanin, S., Palermo, A., & Buchanan, A. H. (2015). Performance and Design of LVL Walls Coupled with UFP Dissipaters. *Journal of Earthquake*

Engineering, *19*(3), 383–409. http://doi.org/10.1080/13632469.2014.987406

Iqbal, A., Smith, T., Pampanin, S., Fragiacomo, M., Palermo, A., & Buchanan, A. H. (2015). Experimental Performance and Structural Analysis of Plywood-Coupled LVL Walls. *Journal of Structural Engineering*, 04015123. http://doi.org/10.1061/(ASCE)ST.1943-541X.0001383

Jeske, J., & Esposito, D. (2015). *2015 Reference Guide: Mid-Rise Wood Construction in the Ontario Building Code*. North Bay, Ontario.

KLH UK. (2015). Technical. Retrieved September 25, 2015, from http://www.klhuk.com/product-/technical.aspx

Klusell, A.-S. (2008). *A competitive analysis of the timber and steel frame building industry in Europe*. Stockholm, Sweden. Retrieved from http://www.s-p-b.pl/opracowania/TimberSteelFrameBuilding_Sweden.pdf

Knee, T. (2015). FPInnovations signs licensing agreement with NZ-based firms. Montreal, Canada: FPInnovations. Retrieved from http://www.prestressedtimberltd.co.nz/news/news-archive-2015/

Krawinkler, H., & Miranda, E. (2004). Performance-Based Earthquake Engineering. In Y. Bozorgnia & V. V. Bertero (Eds.), *Earthquake Engineering: From Engineering Seismology to Performance-Based Engineering* (pp. 560–636). Boca Raton, Florida: CRC Press.

Kuang, J. S. (1998). Why Worry About Earthquake in Regions of Moderate Seismicity: A Case-Study of Hong Kong. *Journal of the Earthquake Engineering Society of Korea*, *2*(3), 111–119.

Lantada, N., Pujades, L. G., & Barbat, A. H. (2009). Vulnerability index and capacity spectrum based methods for urban seismic risk evaluation. A comparison. *Natural Hazards*, *51*(3), 501–524. http://doi.org/10.1007/s11069-007-9212-4

Lewington, J. (2014, December 1). Six-storey wood buildings "a game-changer." *The Globe and Mail*. Cambridge, Ontario. Retrieved from http://tgam.ca/EGfd

Marriott, D. (2009, February). *The Development of High-Performance Post-Tensioned Rocking Systems for the Seismic Design of Structures* (Doctor of Philosophy). University of Canterbury.

Mazzoni, S., McKenna, F., Scott, M. H., & Fenves, G. L. (2006). *OpenSees Command Language Manual*. Berkeley, California: Pacific Earthquake Engineering Research (PEER) Center.

Moroder, D., Sarti, F., Palermo, A., & Pampanin, S. (2014). Experimental investigation of wall-to-floor connections in post-tensioned timber buildings. *NZSEE Conference*.

Morris, H., Wang, M., & Zhu, X. (2012). Deformations and Loads in an LVL Building with 3-Storey Post-Tensioned Shear Walls. In *World Conference on Timber Engineering*. Auckland, New Zealand.

Moses, D., & Gagnon, S. (2010). A New Generation of Solid Wood Panels. *Wood Design & Building*, 40–44.

Natural Resources Canada. (2013). Earthquake Zones in Eastern Canada. Retrieved from http://www.earthquakescanada.nrcan.gc.ca/zones/eastcan-en.php

Natural Resources Canada. (2015). Spotlight: Pushing the heights of building with wood. Retrieved October 15, 2015, from http://www.nrcan.gc.ca/forests/industry/products-applications/16834

Nelson Pine. (2015). Kaikoura District Council building – a world-first amalgam of CLT and LVL. Kaikoura, New Zealand: Build Magazine. Retrieved from http://www.buildmagazine.org.nz/articles/show/timber-takes-on-new-forms/

Newcombe, M. P. (2007). *Seismic design of multistorey post-tensioned timber buildings* (Masters of Earthquake Engineering). *Istituto Universitario di Studi Superiori di Pavia*. Istituto Universitario di Studi Superiori di Pavia.

Newcombe, M. P. (2011). *Seismic Design of Post-Tensioned Timber Frame and Wall Buildings* (Doctor of Philosophy). University of Canterbury.

Newcombe, M. P. (2015). The Connection Response of Rocking Timber Walls. *SESOC Journal*, *28*(1), 46–53.

Newcombe, M. P., Marriott, D., Kam, W., Pampanin, S., & Buchanan, A. H. (2011). Design of UFP-Coupled Post-Tensioned Timber Shear Walls. In *Ninth Pacific Conference on Earthquake Engineering*. Auckland, New Zealand. Retrieved from http://www.ir.canterbury.ac.nz/handle/10092/5361

Newcombe, M. P., Pampanin, S., Buchanan, A. H., & Palermo, A. (2008). Section Analysis and Cyclic Behavior of Post-Tensioned Jointed Ductile Connections for Multi-Story Timber Buildings. *Journal of Earthquake Engineering*, *12*, 83–110. http://doi.org/10.1080/13632460801925632

Nordic Structures. (2015). Nordic X-LAM Cross-Laminated Timber (CLT). Retrieved September 25, 2015, from http://nordic.ca/en/products/nordic-x-lam-cross-laminated-timber-clt

NRCC. (2010). *National Building Code of Canada - Chapter 4*. Canadian Commission on Building and Fire Codes.

Opus International Consultants. (2014). Trimble Navigation. Retrieved December 7, 2015, from http://www.opus.co.nz/projects/trimble-navigation/

Osborne, L., & Dagenais, C. (2015). *Full-scale Mass Timber Shaft Demonstration Fire – Final Report* (Project No. 301009899). *FPInnovations*.

Palermo, A., Pampanin, S., Buchanan, A. H., & Newcombe, M. P. (2005). Seismic design of multi-storey buildings using laminated veneer lumber (LVL). In *New Zealand Society of Earthquake Engineering Conference*. Wairakei, New Zealand.

Palermo, A., Sarti, F., Baird, A., & Bonardi, D. (2012). From Theory to Practice: Design, Analysis and Construction of Dissipative Timber Rocking Post-Tensioning Wall System for Carterton Events Centre, New Zealand. In *World Conference on Timber Engineering*. Lisbon, Portugal.

Pampanin, S. (2015). Towards the "Ultimate Earthquake-Proof" Building: Development of an Integrated Low-Damage System. In A. Ansal (Ed.), *Perspectives on European Earthquake Engineering and Seismology* (Volume 2, Vol. 39). Christchurch, New Zealand: Springer International Publishing. http://doi.org/10.1007/978-3-319-16964-4

Pei, S., Berman, J., Dolan, D., Lindt, J. Van De, Ricles, J., Sause, R., … Rammer, D. (2014). Progress on the development of seismic resilient tall buildings in the Pacific Northwest. In *World Conference on Timber Engineering*. Quebec City, Quebec: World Conference on Timber Engineering.

Pei, S., van de Lindt, J. W., & Popovski, M. (2012). Approximate R-Factor for Cross Laminated Timber Walls in Multi-Story Buildings. *Journal of Architectural*

Engineering, (December), 245–255. http://doi.org/10.1061/(ASCE)AE.1943-5568.0000117.

Polastri, A., Pozza, L., Loss, C., & Smith, I. (2015). Structural characterization of multi-storey CLT buildings braced with cores and additional shear walls. In *International Network on Timber Engineering Research* (pp. 1–14). Sibenik, Croatia.

Priestley, M. J. N., Sritharan, S., Conley, J. R., & Pampanin, S. (1999). Preliminary Test Results from the PRESSS 5-Story Precast Concrete Building. *PCI Journal*, *44*(6), 42–67.

Rahman, M. A. (2008). *Performance-based seismic analysis and design improvements of two precast concrete structural systems* (Doctor of Philosophy). Iowa State University.

Rahman, M. A., & Sritharan, S. (2007). Performance-Based Seismic Evaluation of Two Five-Story Precast Concrete Hybrid Frame Buildings. *Journal of Structural Engineering*, *133*(11), 1489–1500. http://doi.org/10.1061/(ASCE)0733-9445(2007)133:11(1489)

Rahman, M. A., & Sritharan, S. (2015). Seismic response of precast, posttensioned concrete jointed wall systems designed for low- to midrise buildings using the direct displacement-based approach. *PCI Journal*, (March-April), 38–56.

reThink Wood. (2014). Tall Wood Takes a Stand. Retrieved from http://www.rethinkwood.com/sites/default/files/Tall-Wood-CEU-Nov-2014.pdf

Robertson, A. B. (2011). *A Comparative Life Cycle Assessment of Mid-Rise Office Building Construction Alternatives: Laminated Timber Or Reinforced Concrete* (Masters of Applied Science). University of British Columbia.

Sarti, F. (2015, November). *Seismic Design of Low-Damage Post-Tensioned Timber Wall Systems* (Doctor of Philosophy). University of Canterbury.

Sarti, F., Palermo, A., & Pampanin, S. (2012a). Design Charts and Simplified Procedures for Post-Tensioned Seismic Resistant Timber Walls. In *World Conference On Timber Engineering* (pp. 112–121). Auckland, New Zealand.

Sarti, F., Palermo, A., & Pampanin, S. (2012b). Simplified Design Procedures for

Post-Tensioned Seismic Resistant Timber Walls. In *World Conference on Earthquake Engineering*. Lisbon, Portugal.

Sarti, F., Palermo, A., & Pampanin, S. (2015a). Comparison of Force-Based and Displacement-Based Seismic Design of Dissipative Post-Tensioned Rocking Timber Wall Systems. In *New Zealand Society for Earthquake Engineering Conference*.

Sarti, F., Palermo, A., & Pampanin, S. (2015b). Development and Testing of an Alternative Dissipative Posttensioned Rocking Timber Wall with Boundary Columns. *Journal of Structural Engineering*, E4015011. http://doi.org/10.1061/(ASCE)ST.1943-541X.0001390

Sarti, F., Palermo, A., & Pampanin, S. (2015c). Quasi-Static Cyclic Testing of Two-Thirds Scale Unbonded Posttensioned Rocking Dissipative Timber Walls. *Journal of Structural Engineering*, (2008), E4015005. http://doi.org/10.1061/(ASCE)ST.1943-541X.0001291

Schmidt, R. J., & Griffin, C. T. (2013). Barriers to the design and use of cross-laminated timber structures in high-rise multi-family housing in the United States. In P. J. S. Cruz (Ed.), *Structures and Architecture* (pp. 2225–2231). CRC Press.

Smith, T. J. (2014). *Post-tensioned Timber Frames with Supplemental Damping Devices* (Doctor of Philosophy). University of Canterbury.

Smith, T. J., & Buchanan, A. H. (2008). *Feasibility of Multi Storey Post-Tensioned Timber Buildings: Detailing, Cost and Construction* (Master of Engineering). University of Canterbury.

Smith, T., Ludwig, F., Pampanin, S., Fragiacomo, M., Buchanan, A. H., Deam, B., & Palermo, A. (2007). Seismic Response of Hybrid-LVL Coupled Walls Under Quasi-Static and Pseudo-Dynamic Testing. In *New Zealand Society for Earthquake Engineering Conference* (pp. 1–8). Retrieved from http://www.nzsee.org.nz/db/2007/Paper60.pdf

Steele, T. C., & Wiebe, L. D. A. (2016). Dynamic and equivalent static procedures for capacity design of controlled rocking steel braced frames. *Earthquake Engineering & Structural Dynamics*, *in press*. http://doi.org/10.1002/eqe.2765

Structural Timber Association. (2014). *Engineered wood products and an introduction to timber structural systems*. Alloa, UK.

The World Bank. (2014). *Understanding Risk in an Evolving World: Emerging Best Practices in Natural Disaster Risk Assessment. International Bank for Reconstruction and Development*. Washington, U.S.A. Retrieved from http://www.bmj.com/cgi/doi/10.1136/bmj.329.7474.1086

Wiebe, L. (2009). *Mitigation of higher mode effects in self-centering walls by using multiple rocking sections. ROSE Report 2009/01*. Pavia, Italy.

Wiebe, L. (2013). *Design of Controlled Rocking Steel Frames to Limit Higher Mode Effects* (Doctor of Philosophy). University of Toronto.

Wiebe, L., & Christopoulos, C. (2015a). A cantilever beam analogy for quantifying higher mode effects in multistorey buildings. *Earthquake Engineering & Structural Dynamics*, *44*(11), 1697–1716. http://doi.org/10.1002/eqe.2549

Wiebe, L., & Christopoulos, C. (2015b). Performance-Based Seismic Design of Controlled Rocking Steel Braced Frames. II: Design of Capacity-Protected Elements. *Journal of Structural Engineering*, *141*(9), 04014227. http://doi.org/10.1061/(ASCE)ST.1943-541X.0001201

Yeoh, D., Carradine, D., Palermo, A., Shrestha, R., & Morris, H. (2012). *Long-Term Performance of Post-Tensioned LVL Frames and Walls*. Canterbury, NZ. Retrieved from http://hdl.handle.net/10092/10312

Zabalza Bribián, I., Valero Capilla, A., & Aranda Usón, A. (2011). Life cycle assessment of building materials: Comparative analysis of energy and environmental impacts and evaluation of the eco-efficiency improvement potential. *Building and Environment*, *46*(5), 1133–1140. http://doi.org/10.1016/j.buildenv.2010.12.002

Zhang, C. (2015). *Seismic Displacement Demands On Self-Centering Single-Degree-of-Freedom Systems* (Master of Applied Science). McMaster University. Retrieved from http://hdl.handle.net/11375/18193